



UNIVERSITY OF NAIROBI

**DEVELOPMENT OF STABLE AND EFFICIENT TIN
PEROVSKITE SOLAR CELLS USING ANILINIUM
HYPOPHOSPHITE ADDITIVE, AND PERYLENE-DIIMIDE AS A
COPPER INTERFACIAL LAYER**

BY

JORIM OKOTH OBILA

I80/53817/2018

A Thesis Submitted in Fulfilment of the Requirements for the Award of the Degree of Doctor of
Philosophy (PhD) in Physics of University of Nairobi


July 2024

DECLARATION

I declare that this thesis is my original work and has not been submitted elsewhere for examination, award of degree or publication. Where other people's work has been used, this has properly been acknowledged and referenced in accordance with the University of Nairobi requirements

Jorim Okoth Obila

Department of Physics, Faculty of Science and Technology, University of Nairobi, Nairobi

Signed: 

Date: July 4, 2024

The thesis is submitted for examination with our approval as research supervisors

1. Dr. Elijah O. Ayieta

Department of Physics, Faculty of Science and Technology, University of Nairobi,

Signed 

Date 16/7/2024

2. Prof. Robinson J. Musembi


Department of Physics, Faculty of Science and Technology, University of Nairobi

Signed 

Date: 18/07/2024

1. Dr. Chang Eun Song

Advanced Energy Materials Research Center, Korea Research Institute of Chemical
Technology (KRICT)

Signed 

Date 15/07/2024

DEDICATION

To my lovely wife Mealer Achieng', and son Aldrich Noon.

ACKNOWLEDGEMENT

I am very grateful to my supervisors Dr. Elijah O. Ayieta and Prof. Robinson J. Musembi of the University of Nairobi (UoN) for their invaluable comments and advice on my thesis and patience during my PhD program. I also appreciate Dr. Alex A. Ogacho and Prof. Bernard Aduda for their advice and support during the proposal writing and some manuscript writing.

I extend my gratitude to the International Science Program for supporting part of my PhD program. Through ISP support, I was able to conduct part of my research work at Linköping University, Sweden. I also express my gratitude to Prof. Feng Gao of the Department of Physics, Chemistry, and Biology (IFM), Linköping University, for hosting me in his laboratory to carry out my research. The team was a great team with researchers of immense knowledge in perovskite materials and perovskite devices. I would like to appreciate Dr. Feng Wang and Dr. Hongwei Lei for their presence during my laboratory training and as my first-hand advisors at Linköping University.

I also want to thank the Regional Scholarship and Innovation Fund (RSIF) for supporting the bulk part of my PhD program. Through RSIF, I managed to conduct my experimental work at the Korea Research Institute of Chemical Technology (KRICT), South Korea. I thank my host and supervisor at KRICT, Dr. Chang Eun Song for the opportunity to learn the experimental techniques in tin perovskite solar cells. I extend my gratitude to my senior Dr. Nasir Khan for helping me adapt to the KRICT laboratory. In addition, I want to appreciate my colleagues at KRICT and UoN laboratory; Mwende Mbilo, Haris Muhammed, Jahankan Muhammed, Brian Owino Owuor, Jacinter Okwako, and Ryu Du Hyeon for the fruitful discussions we had during this program.

Lastly and importantly, I want to appreciate my family, Mealer Achieng' and Aldrich Noon for always being around. Above all, God controlled the whole journey.

Abstract

Tin perovskite solar cells (Sn-PSCs) have attracted a tremendous attention due to the robust optoelectronic properties of Sn-perovskite materials. The band gap of Sn-perovskite ($\sim 1.3-1.5$ eV), is within the optimal band gap for fabrication of high performing single junction solar cells. However, the power conversion efficiency (PCE) and stability of Sn-PSCs are still low despite the good Sn-perovskite optoelectronic properties. The primary challenge is the ease of oxidation of Sn^{2+} ions in the Sn-perovskite absorber material, and uncontrollable crystallization during Sn-perovskite film formation. In the first part of this study, tin fluoride (SnF_2) and anilinium hypophosphite (AHP) were used to inhibit the oxidation of Sn^{2+} and to maintain the stability of Sn-PSCs. The crystallization was controlled by using solvent engineering technique by mixing N, N-dimethylformamide (DMF), and dimethyl sulfoxide (DMSO), and using chlorobenzene (CB) as an antisolvent. Combining SnF_2 and AHP resulted in stable films with superior optoelectronic properties. The primary reason was the ability of AHP to interact with SnF_2 to produce a complex double salt ($\text{Sn}(\text{H}_2\text{PO}_2)_2 \cdot \text{SnF}_2$) which passivated the grain boundaries and surface of the absorber films. The passivated films were prevented from direct contact with oxygen and moisture, which are the main degrading agents, thereby making the films more stable. SnF_2 and AHP mixture was used to fabricate two Sn-PSCs with absorber layers of $\text{FA}_{0.50}\text{MA}_{0.45}\text{PEA}_{0.05}\text{SnI}_{3.00}$ and FASnI_3 . The PCE of Sn-PSCs from $\text{FA}_{0.50}\text{MA}_{0.45}\text{PEA}_{0.05}\text{SnI}_{3.00}$ absorber layer was up to 6.87% with a stability of 97% after 720 hours of storage in a nitrogen environment. The efficiency of Sn-PSCs from FASnI_3 absorber material rose to 5.48% from 4.04% of the control device. In the second part of this study, perylene-diimide (PDINN) was utilized as a cathode interfacial layer to enhance the performance of Sn-PSCs. Copper (Cu) was used instead of the commonly used silver (Ag) because of its ability to resist corrosion from halide materials originating from the perovskite due to iodine ion migration and diffusion. PDINN was used as a cathode interfacial layer instead of the usual bathocuproine (BCP) because of its better electrical and physical properties. The Sn-PSCs based on PDINN achieved an efficiency of up to 10.99% with an improved stability. The PDINN-based Sn-PSC maintained up to 80% of its PCE even after exposure to the atmospheric air of relative humidity $\sim 35 - 45\%$ and temperature $\sim 19 - 25^\circ\text{C}$. The stability and magnified PCE of PDINN based Sn-PSCS was due to its hydrophobic nature making it difficult for moisture penetration, and its ability to efficiently-transport photogenerated charges at the electron transport layer (ETL)/cathode interface.

LIST OF PUBLICATIONS

1. Obila, J. O., Ryu, D. H., Oh, S., Kim, J. H., Musembi, R. J., Lee, S., Kang, B. J., Jeon, N. J., Ayieta, E. O., Im, S. H. & Song, C. E. (2024). Tin-based Perovskite Solar Cells Containing a Perylene Diimide Cathode Interlayer with a Copper Top Electrode. *ACS Energy Letters*, **9**(3), 1090-1096.
2. Obila, J. O., Lei, H., Ayieta, E. O., Ogacho, A. A., Aduda, B. O., & Wang, F. (2021). Improving the efficiency and stability of tin-based perovskite solar cells using anilinium hypophosphite additive. *New Journal of Chemistry*, **45**(18), 8092–8100.
3. Obila, J.O, Lei, H., Omollo Ayieta, E., Awuor Ogacho, A., Aduda, B. O., & Wang. (2021). Optoelectronic Property Refinement of FASnI₃ films for Photovoltaic Application. *Materials Letters*, **300**, 130099.

TABLE OF CONTENTS

DECLARATION	ii
DEDICATION	iii
ACKNOWLEDGEMENT	iv
Abstract	v
LIST OF PUBLICATIONS	v
LIST OF TABLES	x
LIST OF FIGURES.....	xi
List of Symbols and Formulae	xiv
List of abbreviations.....	xvii
CHAPTER ONE	1
INTRODUCTION.....	1
1.1 Background.....	1
1.2 Problem Statement.....	5
1.3 Objectives of the Study.....	6
1.3.1 General Objective	7
1.3.2 Specific Objectives	7
CHAPTER TWO.....	10
LITERATURE REVIEW	10
2.1 Perovskite Solar Cell Technology	10
2.2 Lead Perovskite Solar Cells (Pb-PSCs).....	12
2.2.1 Challenges and Possible Solutions for Lead Halide PSCs.....	13
2.3 Tin-Perovskite Solar Cells (Sn-PSCs).....	15
2.3.1 Degradation mechanisms of tin-perovskites in the ambient environment.....	15
2.3.2 Electronic impact of the instability of tin-perovskite	16
2.4 Improving the Photovoltaic Properties of Sn-PSCs	17
2.4.1 Architectural Engineering of Sn-PSCs	18
2.4.2 Film Morphology	19
2.4.3 Use of additives and co-additives	21
2.4.4 Mixing of organic cations	22
2.4.5 Dimensionality Adjustment in Sn-Perovskite Absorber Material	23
CHAPTER THREE.....	27
THEORETICAL BACKGROUND	27

3.1 Ostwald Ripening	27
3.2 Urbach Energy (Absorption Band Tail) of Perovskite Absorber Material.....	27
3.3 Power Conversion Efficiency (η) of a Photovoltaic Cell.....	29
3.4 Open-Circuit Voltage (V_{oc}) of Sn-PSC	30
3.4.1 Open-Circuit Voltage (V_{oc}) Loss and Approaches used in Improving the V_{oc} in Sn-PSCs.....	32
3.5 Photoluminescence (PL) and Time-Resolved Photoluminescence (TRPL) Spectroscopy ..	33
3.6 Charge Recombination (monomolecular and bimolecular) in PSCs.....	35
3.7 Charge Trap Density Concentration in Sn-Perovskite Layers.....	37
3.8 Mott-Schottky (M-S) Analysis	39
3.9 Principles of Fourier Transform Infrared Spectrometer (FTIR) Spectroscopy	41
3.10 Use of PDINN as a Buffer Layer and Cu as an electrode in Sn-PSCs	42
CHAPTER FOUR.....	44
MATERIALS AND METHODS	44
4.1 Fabrication and Characterization of FA _{0.50} MA _{0.45} PEA _{0.05} SnI _{3.00} and FASnI ₃ Solar Cells...44	
4.1.1 Materials	44
4.1.2 Substrate Cleaning	44
4.1.3 Solution Preparation.....	46
4.1.4 Sn-PSCs Fabrication	47
4.1.5 Films and Devices Characterization	48
4.2 Fabrication and Characterization of FA _{0.70} EA _{0.15} PEA _{0.15} SnI _{2.70} Br _{0.30} Solar Cells	49
4.2.1 Materials	49
4.2.2 Synthesis of tin iodide (SnI ₂)	49
4.2.3 Recrystallization of FAI, EAI, FABr and PEAI	50
4.2.4 Solution Preparations	50
4.2.5 Device Fabrication	51
4.2.6 Characterization of Films and Devices	52
CHAPTER FIVE.....	53
RESULTS AND DISCUSSION	53
5.1 FA _{0.50} MA _{0.45} PEA _{0.05} SnI _{3.00} films and solar cells	53
5.1.1 Morphology of the Perovskite Layer	53
5.1.2 Fourier Transform Infrared Spectroscopy Measurement and Reaction Mechanism	55
5.1.3 X-Ray Diffraction Measurement Results.....	57

5.1.4 Absorption Spectra of FA _{0.50} MA _{0.45} PEA _{0.05} SnI _{3.00}	60
5.1.5 Photoluminescence and Time-resolved photoluminescence measurement	61
5.1.6 Photovoltaic Properties of the FA _{0.50} MA _{0.45} PEA _{0.05} SnI _{3.00} Solar cells	62
5.1.7 External Quantum Efficiency of the Devices	68
5.2 FASnI ₃ films and solar cells	70
5.2.1 Film Morphology	70
5.2.2 The Perovskite Film Structural Measurement	73
5.2.3 Absorption Spectra of FASnI ₃	75
5.2.4 Photoluminescence and Time-resolved photoluminescence measurement	76
5.2.5 Photovoltaic Properties of the FASnI ₃ Solar Cells.....	77
5.3 FA _{0.70} EA _{0.15} PEA _{0.15} SnI _{2.70} Br _{0.30} Solar Cells.....	81
5.3.1 Photovoltaic Performance	81
5.3.2 Potassium Thiocyanate (KSCN) and PDINN Optimization	86
5.3.3 Structural Defects within the Perovskite Absorber Layer	89
5.3.4 Charge recombination within the Sn-perovskite solar cells	91
5.3.5 The photogenerated charge transport in the BCP and PDINN based Sn-PSCs	96
5.3.6 Investigation of moisture and oxygen stability of Sn-perovskite solar cells.	97
CHAPTER SIX	100
CONCLUSIONS AND RECOMMENDATIONS.....	100
6.1 Conclusions	100
6.2 Recommendations for Further Works	100
References	102

LIST OF TABLES

Table 3.1. Summary of TRPL data interpretation.....	35
Table 5.1. Summary of the photovoltaic characteristics of the devices fabricated using FA _{0.50} MA _{0.45} PEA _{0.05} SnI _{3.00} perovskite absorber layer	63
Table 5.2. A summary of the photovoltaic properties of the developed devices, both modified and reference devices.	78
Table 5.3 Summary of the PCE parameters of the solar cells, for both individual champion cells and the statistical average.	84
Table 5.4 Optimization of KSCN concentration in DMF	87
Table 5.5. Optimization of PDINN concentration	89
Table 5.6. Electrical impedance spectra parameters obtained after the Nyquist plot fitting.	92

LIST OF FIGURES

Figure 1.1. Architectural designs for PSCs (a) mesoscopic (b) planar	5
Figure 1.2. Charge transfer processes in a PSC.	5
Figure 2.1. A typical perovskite structure	11
Figure 2.2. Decomposition mechanism of lead-based perovskite films.	14
Figure 2.3. Predicted degradation routes of tin-perovskite in the ambient environment.	16
Figure 2.4. A summary of the oxidation process in Sn-perovskites	17
Figure 2.5. An illustration concerted efforts researchers are putting on designing stable and high performing Sn-PSC structure	19
Figure 2.6. An illustration of how to use the antisolvent.	20
Figure 2.7. 2D-quasi-2D-3D perovskite resulting from depositing a bulky ammonium cation on the 3D perovskite absorber.	24
Figure 3.1. Equivalent circuit model for a solar cell.....	30
Figure 3.2. Basic principles of PL spectroscopy.....	34
Figure 3.3. Electron-only device.....	39
Figure 3.4. An example of an M-S plot	40
Figure 3.5: Block diagram of working principal of FTIR spectroscopy.....	41
Figure 4.1. The block diagram of the UV-ozone cleaner machine	45
Figure 4.2. The mechanism of UV-ozone cleaning	45
Figure 4.3. The two-step deposition procedure of the perovskite solution	47
Figure 5.1. Scanning electron microscope images of FA _{0.50} MA _{0.45} PEA _{0.05} SnI _{3.00} films having 0 (%) (a) and (b), 5% (c) and (d), and 10% (e) and (f) AHP under different magnifications.	54
Figure 5.2. The FTIR spectra of (a) AHP, and a mixture of AHP and SnF ₂ (b) tin-perovskite film with and without AHP as a co-additive, and (c) the extract of the region between 1086 and 1250 cm ⁻¹ of (b) for easy visibility.	56
Figure 5.3. The XRD peaks of FA _{0.50} MA _{0.45} PEA _{0.05} SnI _{3.00} upon exposure to air at varried time intervals .	58
Figure 5.4. The FWHM of the perovskite layer with and without AHP at zero hours exposure to normal atmospheric conditions.	59
Figure 5.5. The rate of peak intensity decay time for films with and without AHP.	60
Figure 5.6. Absorption spectra of Sn-perovskite films containing and without 5% AHP; the inset shows the band gaps of the films with and without AHP.....	61
Figure 5.7. (a) PL spectra of FA _{0.50} MA _{0.5} PEA _{0.45} SnI _{3.00} with and without AHP additive, (b) TRPL spectra of FA _{0.50} MA _{0.45} PEA _{0.05} SnI _{3.00} having and without AHP.	62
Figure 5.8. The J-V curves of the best solar cells fabricated from control films and films containing AHP.	64
Figure 5.9. Steady-state PCE of devices fabricated with absorber film with and without 5% AHP	66
Figure 5.10. The histogram shows the performance of some of the fabricated devices.	67
Figure 5.11. (a) Stability of the Sn-PSCs with and without 5% AHP under light soaking (b) J-V curves of freshly fabricated devices and devices stored after 30 days.	68

Figure 5.12. (a) EQE and the integrated photocurrent of Sn-PSCs with and without AHP. (b) EQE and the integrated photocurrent of the devices with and without AHP after exposure to air for 20 minutes	69
Figure 5.13. SEM images of the FASnI ₃ films containing (a) 0% (b) 5% and (c) 10%, of AHP.....	71
Figure 5.14. Histograms of grain sizes of the FASnI ₃ films with varied amounts of AHP.	72
Figure 5.15. SEM-EDS elemental mapping of (a) F and (b) P distribution on film containing both AHP and SnF ₂	72
Figure 5.16. The XRD patterns of FASnI ₃ films fabricated with varied amounts of AHP.....	73
Figure 5.17 Magnification of peak (100) of Figure 5.16 for FWHM approximation for films with and without AHP.	75
Figure 5.18. (a) Absorption spectra of films with varied amounts of AHP, (b) Absorption spectra of films with and without 5% AHP.....	75
Figure 5.19 (a) PL spectra of FASnI ₃ with varied amounts of AHP, (b) TRPL spectra of FASnI ₃ with and without 5% AHP.....	76
Figure 5.20. The $J - V$ curves of the best solar cells fabricated from control films and films containing both AHP and SnF ₂ additives.	78
Figure 5.21. The histogram shows the performance of some of the fabricated devices.	79
Figure 5.22. (a) Steady-state PCE of the reference and modified device (b) Stability test of the reference and modified device.	80
Figure 5.23. EQE and the integrated photocurrent of the cells of the reference and modified devices.....	80
Figure 5.25. The possible flow of electrons and holes in a PCBM+P3HT system.....	81
Figure 5.26. Current density-voltage ($J - V$) curves of (a) freshly prepared solar cells, (b) BCP and PDINN after 5 days, and the fresh device without buffer layer.	82
Figure 5.27. (a) Steady PCE output of the three devices. (b) The statistical representation of 20 devices of each condition.	83
Figure 5.28. (a) The EQE curves of the three champion devices. (b) Stability measurement of the champion devices.	84
Figure 5.29. The storage evolution of the $J - V$ curves of (a) control device without buffer layer (b) BCP-based device and (c) PDINN-based device.	86
Figure 5.30. (a) The variation of the photovoltaic properties of the devices with KSCN concentration. (b) The optical absorption spectra of perovskite films deposited on plain glass and on glass coated with KSCN.	87
Figure 5.31. The variation of the photovoltaic properties of the devices with PDINN concentration.	89
Figure 5.32. The Urbach energy of the perovskite film is based on the UV-Vis absorbance data.....	90
Figure 5.33. (a) The Nyquist plot from the EIS measurement for control, BCP, and PDINN devices. (b) Mott-Schottky plots of the devices measured at 100 kHz in the dark.....	92
Figure 5.34. (a) The linear relationship of V_{oc} against logarithmic light intensity. (b) Double logarithmic of J_{sc} against light intensity.	94
Figure 5.35. (a) Dark current graphs of the devices measured under dark condition (b) SCLC plots of hole-only devices with ITO/PEDOT:PSS/with or without KSCN/perovskite/MoO ₃ /Cu.....	95
Figure 5.36. (a) Transient photovoltage curves (b) Transient photocurrent curves of Sn-perovskite solar cells based on BCP and PDINN cathode interfacial layer.	97

Figure 5.37. Photo-stability of Sn-PSCs with PDINN and BCP interlayer taken at intervals of 2 hours after exposure to ambient air for 14 hours. (The relative humidity was ~38.8 – 44.3%, and temperature ~18.3 – 20°C). 98

Figure 5.38. Water contact angle of (a) PCBM, (b) PCBM/BCP and (c) PCBM/PDINN. 99

List of Symbols and Formulae

t	Goldschmidt's tolerance factor
D_n	Diffusion coefficient of electrons
D_p	Diffusion coefficient of holes
E_U	Urbach Energy
E_g	Band gap energy
J_0	Dark current
J_{ph}	Photogenerated current
L_n	Diffusion length of the minority carriers in n-type region
L_p	Diffusion length of the minority carriers in p-type region
N_A	Density of acceptors
N_D	Density of donors
P_{in}	Power input
R_{sh}	Shunt resistance
V_{loss}	Open-circuit voltage loss
V_{OC}	Open-circuit voltage
k_B	Boltzmann constant
n_i	Carrier density
ϵ_0	Permittivity of free space
τ_{quench}	Quench carrier lifetime
μL	microliters
Ag	Silver
Al_2O_3	Aluminium oxide
Au	Gold
BA^+	Butylamine
Bi	Bismuth
Br^-	Bromide
$^\circ\text{C}$	Degrees Celsius
$\text{C}_6\text{H}_5\text{NH}_3\text{H}_2\text{PO}_2$	Anilinium hypophosphite
CaTiO_3	Calcium titanate

Cl^-	Chloride
CO_2	Carbon (iv) oxide
Cs^+	Cesium
Cu	Copper
EDAI_2	Ethylenediammonium diiodide
FA^+	Formamidinium ion
Ge	Germanium
Ge^{2+}	Germanium (ii) ions
H_2O	Water
H_3PO_2	Triethylphosphine
MA^+	Methylammonium
η	Power Conversion Efficiency
$\text{NH}_4\text{H}_2\text{PO}_2$	Ammonium hypophosphite
NH_4SCN	Ammonium thiocyanate
Pb	Lead
PEA^+	Phenyl ethylammonium
s	Second
Sn	Tin
Sn^{2+}	Tin (ii) ions
Sn^{4+}	Tin (iv) ions
SnF_2	Tin fluoride
SnI_2	Tin iodide
SnO_2	Tin oxide
TiO_2	Titanium oxide
A	Area
B	Amplitude
C	Space-charge capacitance
L	Thickness
T	Absolute temperature
n	Ideality factor
q	Elementary charge

α	Absorption coefficient
ε	Relative dielectric constant of the absorber
μ	Charge mobility
τ	Carrier lifetime

List of abbreviations

J_{sc}	Current density
N_D	Defects concentration
V_{OC}	Open-circuit voltage
V_{TFL}	Trap filling limited voltage
V_{bi}	Built-in potential
2D	Two dimension
3D	Three dimension
AC	Alternating current
AHP	Anilinium hypophosphite
Asp	Asparagine
BCP	2,9-dimethyl-4,7-diphenyl-1,10-phenanthroline
BCP	Bathocuproine
CB	Chlorobenzene
CB	Conduction band
CdTE	Cadmium telluride
CIGS	Copper indium gallium selenide
c-TiO ₂	Compact titanium oxide
DE	Diethyl ether
DMA	N, N-dimethylacetamide
DMF	N, N-dimethylformamide
DMSO	Dimethyl sulfoxide
DSSCs	Dye-sensitized solar cells
EAI	Ethylammonium iodide
EDTA	Tetraacetic acid
EIS	Electrochemical impedance spectroscopy
ETL	Electron transporting layer
ETM	Electron transporting medium
eV	Electron volt

FABr	Formamidinium bromide
FAI	Formamidinium iodide
FTIR	Fourier-transform infrared
GBL	γ -butyrolactone
HOMO	Highest occupied molecular orbital
HTL	Hole-transporting layer
HTM	Hole transporting medium
ICBA	Indene-C60 bisadduct
IPA	Isopropyl alcohol
ITO	Indium-tin-oxide
KSCN	Potassium thiocyanate
LiTFSI	Bistrifluoromethanesulfonimide
LUMO	Lowest unoccupied molecular orbital
MA	Methyl acetate
MAI	Methylammonium iodide
mp-TiO ₂	mesoporous titanium oxide
M-S	Mott-Schottky
P3HT	Poly(3-hexylthiophene-2,5-diyl)
Pb-PSCs	Lead perovskite solar cells
PC ₆₀ BM	[6,6]-phenyl-C60-butyric acid methyl ester
PCBM	[6,6]-phenyl-C61-butyric acid methyl ester
PCE	Power conversion efficiency
PDINN	Perylene-diimide
PEAI	Phenethylammonium iodide
PEDOT:PSS	Poly(3,4-ethylenedioxythiophene):polystyrene sulfonate
PL	Photoluminescence
PMMA	Poly(methyl methacrylate)
PSCs	Perovskite solar cells
PTFE	Polytetrafluoroethylene
PZ	Pyrazine

R-P	Ruddlesden – Popper
SCLC	Space charge limited current
SEM	Scanning electron microscope
SnCl ₂	Tin chloride
Sn-PSCs	Tin perovskite solar cells
TL	Toluene
TRPL	Time-resolved photoluminescence
TWh	Terawatt-hours
VB	Valence band
XRD	X-ray diffractometer
α -Si	Amorphous silicon
$J - V$	Current density voltage

CHAPTER ONE

INTRODUCTION

1.1 Background

Globally, energy demand is on the rise to match the ever-increasing human population. The energy demand is almost directly proportional to the population around the globe. For example, it is estimated that as of 2022, 5 billion people lived in areas with the need for space cooling. This number is predicted to rise to 7 billion by 2050, and electricity demand for this is expected to go as high as 5200 terawatt-hours (TWh), as the number of air conditioners will increase by 90 % (World Energy Outlook, 2022). In addition, the economic outlook of the world dictates the need for energy; both the developed and developing worlds need energy to stimulate their economic growth. Therefore, the world must have sustainable energy sources to maintain the economic development progress, and to sustain the ever-growing population.

Currently, the world depends on limited mineable fossil fuel sources of energy such as oil, coal, and natural gas. In 2020 alone, fossil fuels contributed up to 82% of the primary energy consumed (“bp Statistical Review of World Energy”, 2022). All these fossil fuel sources have their disadvantages and cannot be relied upon for future energy sustainability. Natural gas faces challenges of fluctuating prices with its prices hitting a record high in recent years; coupled with increased energy security alarms (“bp Statistical Review of World Energy”, 2022). The demand for natural gas is predicted to decline by 0.4 % between 2020 and 2030 because of the challenges facing natural gas (World Energy Outlook, 2022). Many have viewed coal as an alternative to expensive gas but coal is dangerous to the environment due to its excess carbon (iv) oxide emission to the environment. In 2021, carbon emissions from fossil fuels rose by 5.9% to 33.9 gigatonne CO₂ (GtCO₂) (“bp Statistical Review of World Energy”, 2022). However, according to the Announced Pledges Scenario (APS), the world is expected to shift its dependence on fossil fuels to reduce emissions for a better world with minimal unexpected climate change (International Energy Agency, 2021). The energy demand around the globe is projected to skyrocket in the future, but depending exclusively on fossil fuel energy sources can only result in degrading the environment, and human and animal health. Therefore, there is a need for the exploitation of clean energy sources.

Access to clean energy sources such as electricity is a challenge to a large percentage of people in developing economies, especially in rural areas. The developing world experiences a high cost of electric power due to unpredictable inflations (Deutsche Bank, 2014). The high price together with inflation has made access to electricity difficult, as most people cannot be connected to the national electrical power grid systems. It was predicted that the population without electricity would surge in 2022 for the first time in decades, probably because of population increase (World Energy Outlook, 2022). The developing world, which has most rural zones, must look into alternative ways of curbing the energy menace.

The demand for alternative clean, sustainable, and renewable energy has increased greatly around the globe, especially in developing economies. Some of the renewable energy sources include biomass, solar, tidal, wind, and geothermal energy. Solar energy among the renewable energy sources is the most clean, abundant, and reliable in most geographical locations (Tumen-Ulzii *et al.*, 2021). Therefore, it is of urgent need to find efficient and effective means of converting solar energy to electricity for both domestic and industrial use. Photovoltaic devices have been fabricated over the years to harvest solar energy; the main effort being concerted towards harvesting solar energy efficiently and at low cost and using a minimal amount of materials.

Silicon (Si) photovoltaics is the first-generation solar technology, which has gained the most trust and fame globally. The solar-to-electricity power conversion efficiency (PCE) of Si solar cells stands at 26.6 % (Yoshikawa *et al.*, 2017). Silicon solar technology however is faced with several fundamental limitations; firstly, the raw materials are abundantly available but not in their pure form needed for photovoltaic device fabrication. Silicon exists as sand around beaches in the form of silicon (iv) oxide, but it takes a lot of energy to convert silicon oxide to pure silicon, silicon oxide is melted at around 1500 – 2000 °C. The amount of energy needed for such high temperatures is tremendously expensive and in addition during such processes, fossil fuels are used which increases greenhouse gas emissions to the environment (Imamzai *et al.*, 2012).

Secondly, silicon is rigid and thus silicon solar modules are only limited to rooftops and other regions where they can be placed in flat positions; this limits their use, especially to small spaced areas, which requires the modules to bend (Efaz1 *et al.*, 2021). Thirdly, the wafers used in making the solar cells are big which means a lot of material has to be used to make the modules; the sunlight absorption coefficient of silicon is moderate, and thus thicker wafers are required for maximum

sunlight absorption (Efazl *et al.*, 2021; Imamzai *et al.*, 2012). To contain the carbon emissions and high increase in the electricity demand, it is estimated that photovoltaic electricity should contribute to at least 20% of the entire primary energy demand (Deutsche Bank, 2014). Therefore, researchers must come up with alternative solar technologies to counter the silicon solar cell technology challenges and propel the use of photovoltaics forward.

Thin film solar technology is a promising replacement/supplement to silicon solar technology. Thin film solar cells, have good photoactive materials with better light absorption capabilities, implying that only a small quantity of materials is required in fabricating the photovoltaic devices. The reduced material means reduced cost of production. Thin films are not as fragile as silicon making them easy to handle (Efazl *et al.*, 2021). In addition, thin film photovoltaic devices can be fabricated in all kinds of shapes due to their flexibility; this broadens the applications of photovoltaic technology to areas where silicon devices cannot penetrate.

Some of the notable commercialized thin film solar technology include; cadmium telluride (CdTE), amorphous silicon (α -Si), and copper indium gallium selenide (CIGS). The efficiencies of these technologies stand at 23.4% (W. Liu *et al.*, 2022), 22.1%, and 14.0% for CIGS, CdTE, and α -Si, respectively (“NREL Best Research-Cell Efficiency Chart”, 2022; Seroka *et al.*, 2022). α -Si requires little material to fabricate as compared to Si-solar cells, however, it is expensive to create thin silicon wafers, moreover, the amorphous nature of α -Si does not favour charge transport in photovoltaic devices (Seroka *et al.*, 2022). CdTE commercialization is limited by the incorporation of toxic cadmium; it is a danger to the environment and humanity (T. D. Lee & Ebong, 2017). CIGS efficiency is good but cannot compete effectively with other solar technology because of the complexity of its structure, and indium is not readily available making its commercialization limited (T. D. Lee & Ebong, 2017).

The challenges facing the commercialized thin film solar technology make it a priority for an alternative to be sort. Perovskite solar cells (PSCs) are an appealing alternative to many researchers and are considered an alternative to thin film solar technology. Perovskites refer to materials with crystal structures comparable to that of calcium titanate (CaTiO_3) structure. From the CaTiO_3 formula, scientists have concluded that the perovskite structure basic formula is ABX_3 , where A is Ca, B is the Ti, and X_3 is the O_3 . But for device applications, the ABX_3 refers to different components; where A can be an inorganic or organic ammonium cation like cesium (Cs^+),

methylammonium (MA^+), and formamidinium (FA^+) cations or a mixture of the cations; B can be lead (Pb^{2+}) or tin (Sn^{2+}) cations or a mixture of the cations; and X is a halide anion like bromide (Br^-), chloride (Cl^-) and iodide (I^-) or a mixture of the halide anions.

Gustav Rose, a German scientist, found the CaTiO_3 mineral in 1839 in the Ural Mountains and named it "perovskite" in honour of Lev von Perovski, a Russian mineralogist. The research on perovskites started as early as 1978 when Weber's research group replaced calcium with cesium (Weber, 1978). The work on perovskite was later revived in 2009 extensively and intensively for applications in photovoltaic devices. The commonly used perovskites are currently referred to as hybrid organic-inorganic perovskites, but in this study, the name perovskites will mostly be used.

Perovskites have strong optoelectronic characteristics such as: (i) high light absorption capability in the range of $\sim 10^4 \text{ cm}^{-1}$ (M. Wang *et al.*, 2021); tunable bandgaps ranging between $\sim 1.35 - 1.9$ eV, which is approximately the ideal band gap for absorber materials in single junction solar cells, and also permits for wide range light absorption (Faridi *et al.*, 2022). (ii) Low exciton binding energy of between 37 and 45 meV, making the electron-hole pair separation easy and efficient (C. Wang *et al.*, 2019). (iii) Long carrier diffusion lengths of up to $\sim 1 \mu\text{m}$, helps in enhancing charge transport and collection resulting in better device performances (Z. Wang *et al.*, 2020). (iv) High carrier mobility ranging between $1 - 25 \text{ cm}^2\text{V}^{-1}\text{s}^{-1}$ and carrier lifetime ranging from nanoseconds to $175 \mu\text{s}$ (Tailor *et al.*, 2021). These excellent properties make perovskites desirable for application as absorber materials in solar cells known as perovskite solar cells (PSCs).

PSC is a photovoltaic device having a perovskite compound as a light absorber layer. Mesoscopic and planar architectural designs are the two most popular architectural designs in PSCs constructions (Vivo *et al.*, 2017). In a mesostructured design, the perovskite thin film is deposited on mesoporous- TiO_2 , acting as an electron-transporting layer (ETL) film followed by a hole-transporting layer (HTL) (spiro-MeOTAD) and finally, a back contact, which can be gold (Au), Silver (Ag) or any other appropriate metal, as shown in Figure 1.1(a). The structure can be summarized as block- TiO_2 /Mesoporous- TiO_2 (ETL)/Perovskite/Spiro-MeOTAD (HTL)/Gold. In planar structural design, perovskite film is deposited directly on the compact TiO_2 (c- TiO_2), where c- TiO_2 acts as the ELT. This kind of perovskite solar cell structure where the active layer is deposited on ETL is known as the n-i-p configuration.

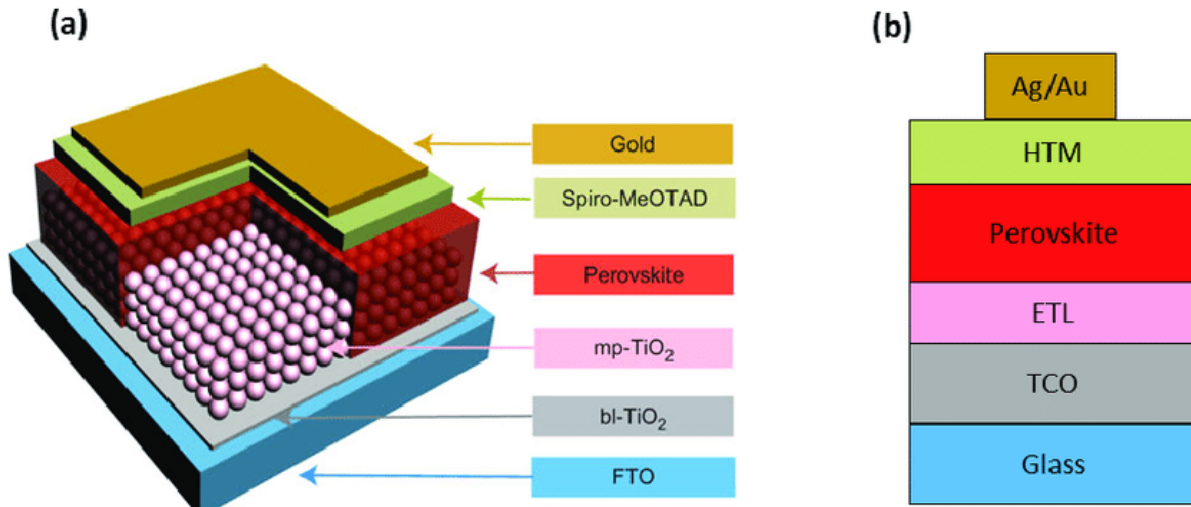


Figure 1.1. Architectural designs for PSCs (a) mesoscopic (b) planar (Vivo et al., 2017)

The basic operation of PSCs includes photon absorption, excitons creation, excitons diffusion and separation, charge transmission, and charge collection. The operation is summarized as shown in Figure 1.2. Photogeneration takes place once a photon with sufficient energy is absorbed.

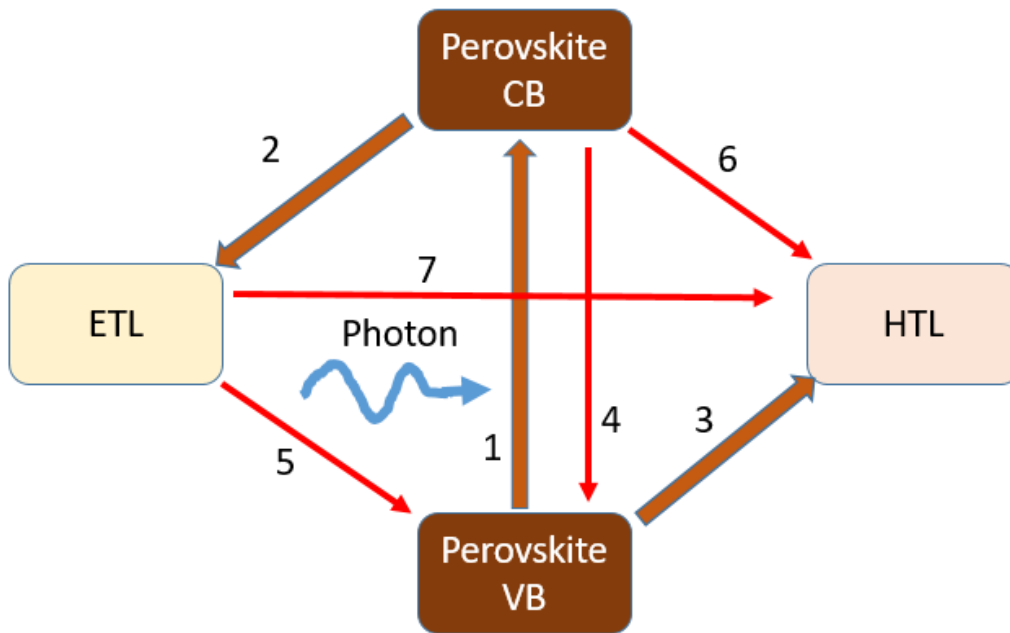


Figure 1.2. Charge transfer processes in a PSC.

Upon photon absorption by the perovskite layer, photoexcitation (1) takes place, where excitons are created. The excitons separate and the electrons are pumped into the ETL (2), and the holes

into the HTL (3). The charges can then be collected at the contacts to generate electricity. During PSC operations some unwanted processes can take place: recombination of the generated electron-hole pair (4), back charge transfer at the interface of HTL and ETL with perovskite film (5 and 6, respectively), and between ETL and HTL (7) (this occur if perovskite film is not entirely covering the ETL surface, leading to direct contact between HTL and ETL). For a high-performing PSC, processes 4-7 should work on a reduced timescale than the charge generation and extraction (processes 1-3).

Researchers' work to control the device structure, interfacial layer engineering, and fabrication methods, has made the PCE of PSCs jump from 3.8% (Kojima *et al.*, 2009) recorded in 2009 to 26.1% in 2022 (D. Li *et al.*, 2023; Li *et al.*, 2023; National Renewable Energy Laboratory, 2022; Park *et al.*, 2023). Lead-based perovskite absorber materials have been exploited to develop lead-perovskite solar cells (Pb-PSCs), these kinds of PCE are known as lead-PSCs, and they are the best-performing PSCs. The quick upsurge in the PCE of PSCs is possible because of their outstanding optoelectronic characteristics of Pb-perovskites. However, lead is toxic, and thus a replacement should be sought to protect the environment and people fabricating the devices. Some of the possible alternatives for Pb include tin (Sn), germanium (Ge), bismuth (Bi), and copper (Cu) (Ke *et al.*, 2019). Sn, however, stands a better chance of replacing Pb, since its electronic properties are comparable to that of Pb (Kayesh *et al.*, 2018). Sn-perovskites have band gaps varying between $\sim 1.3 - 1.4$ eV, which is ideal for a single junction solar cell; this can help in achieving the theoretically predicted Shockley-Queisser Limit of 33 % PCE (Zhao *et al.*, 2017; Guo *et al.*, 2022).

The current highest PCE of Sn-PSCs stands at 14.8 % (B. Yu *et al.*, 2021). This PCE is low as compared to Pb-PSCs PCE of 26.1%. Moreover, the long-term stability of Sn-PSCs is still poor as compared to the Pb-PSCs. The low stability and PCE are a result of the ease of oxidation and uncontrollable crystallization of Sn-perovskite layers (Ke *et al.*, 2019). The stability and PCE issues are a big drawback to the commercialization of PSCs technology. Therefore, there is a need for more research on Sn-PSCs to identify ways of improving their PCE and stability to advance the chances of commercialization of PSCs technology.

1.2 Problem Statement

Researchers for a long time have relied on the superb optoelectronic properties of Pb-perovskite absorber materials, which include long charge-carrier diffusion lengths, strong-light absorption

coefficient, and long charge-carrier lifetimes, to come up with some of the best-performing PSCs. The lowest bandgap of lead-halide perovskite absorber material is ~ 1.5 eV, this is out of the range of the ~ 1.3 - 1.4 eV needed for maximum theoretical efficiencies of single-junction solar cells. In addition, lead is toxic in its soluble form, hence posing danger both at the time of production and disposal of lead-based photovoltaic devices. These two issues have forced researchers to seek alternative metal halide semiconductors.

Tin halide is considered a promising substitute to replace lead halide in PSCs due to its unique optoelectronic characteristics. Tin halide is drawing much attention because its bandgap can be altered between $1.3 - 1.4$ eV, which is within the range of values desired for optimum single-junction solar cell operation. Tin halide perovskites however are unstable in the ambient environment; the Sn^{2+} ion in Sn-perovskites is readily oxidized in the ambient conditions to their Sn^{4+} thermodynamic stable state. Tin oxidation in the perovskite films introduces charge-carrier recombination pathways, which lowers the PCEs of the devices. The reduced durability of tin-perovskites films is aided by the poor quality of the absorber films; the rate of crystallization of absorber material is rapid leading to films with poor morphology, and high density of pinholes, which act as entry pathways for the degrading agents such as oxygen and moisture, to penetrate the film. Therefore, it is necessary to deposit homogeneous and dense Sn-perovskite films to avoid faster degradation of Sn-PSCs. In addition, it is desirable to seek alternative charge transport materials to alleviate charge recombination in the devices and thus improve devices' PCEs and stability.

The rate of crystallization in this work was controlled using complete solvent engineering involving a mixture of perovskite solvents and antisolvents. The oxidation of Sn-perovskite was controlled by the use of additives and co-additive technique; the additives also improved the stability of Sn-PSCs. The charge accumulation at the interface between the electron transport layer (ETL) and the cathode was controlled by using different cathode interfacial layers.

1.3 Objectives of the Study

1.3.1 General Objective

The primary aim of this research is to fabricate stable tin perovskite solar cells (Sn-PSCs) with enhanced photovoltaic conversion efficiencies (PCEs).

1.3.2 Specific Objectives

The main objective is subdivided into the following specific objectives

- i. To optimize, deposit, and characterize tin-perovskite films.
- ii. To fabricate and characterize tin-perovskite-based solar cells.
- iii. To study the influence of different buffer layers on the photovoltaic properties of Sn-PSCs.
- iv. To monitor the stability of the fabricated solar cells.

1.4 Justification and Significance of the Study

The expected improved efficiency and stability of Sn-PSCs can propel forward the idea of commercialization of perovskite solar technology. Sn-perovskite film formation is marred with uncontrollable crystallization, which leads to poor film morphology, which has a high density of pinholes and defects. The use of solvent engineering is important in alleviating crystallization challenges, for example, DMSO used in the mixed solvent technique has a high coordination effect and thus, can coordinate with the organic ammonium cation and SnI_2 to reduce their rate of reaction and hence slow down the crystallization to lead to films with large grains and reduced defects (X. Jiang *et al.*, 2021). Anti-solvent dripping, which is part of solvent engineering, is essential in increasing nucleation sites during film formation, the increased nucleation sites help in the growth of films with good surface coverage on the substrates (Hoefler *et al.*, 2017; Y. Li *et al.*, 2022). Improved film coverage and lack of defects are essential in the fabrication of high-performing devices.

The stability issue is disadvantageous to the long-term performance of PSCs. SnF_2 has often been used as an antioxidant in tin perovskites, however, its use always results in the formation of other unwanted phases (J. Cao *et al.*, 2019; D. Wu *et al.*, 2020). The unwanted phases act as charge trap centers leading to high charge recombination in the devices. To improve device performance, the aggregates have to be eliminated. In this work a phosphite compound is used to eliminate the unwanted phases created by excess SnF_2 , the compound can interact with SnF_2 to create a double-complex salt which is dispersed on the surface of the perovskite film. The distributed double salt acts as a passivator on the film surface and leads to the formation of what is known as self-encapsulation. The self-encapsulation of the devices is important in improving the device stability. In addition, BCP has always been used as a cathode interfacial layer in the p-i-n structure of Sn-

PSCs. BCP is thickness sensitive, the thickness is not easily controlled in solution-processed PSCs layers; the lack of thickness control leads to charge accumulation at the cathode interface, which leads to hysteresis in the device and thus lowered PCE. Therefore, there is a need to seek alternative interfacial layers for better Sn-PSCs PCEs.

CHAPTER TWO

LITERATURE REVIEW

2.1 Perovskite Solar Cell Technology

Hybrid perovskites have drawn remarkable attention from optoelectronic researchers in the past decade due to their robust electrical and optical properties (E. H. Jung *et al.*, 2019; Lanzetta *et al.*, 2020). The concerted attention has seen a rapid rise in the PCE of the PSCs from 3.8% (Kojima *et al.*, 2009), to a record certified PCE of 26.1% (“NREL Best Research-Cell Efficiency Chart”, 2022; D. Li *et al.*, 2023; Lanzetta *et al.*, 2020; Y. Liu *et al.*, 2020). The two major subdivisions of PSCs are lead-PSCs and lead-free-perovskite solar cells. Lead-free-PSCs are a result of the replacement of lead with other materials deemed to be less or nontoxic as compared to Pb (Igbari *et al.*, 2019).

The optimal perovskite equilibrium structure is essential in considering an element or elements as potential lead replacements. ABX_3 formula is generally used to denote perovskites; where A is a monovalent organic or inorganic cation (FA^+ , MA^+ , or Cs^+), B is a divalent metal cation ion, commonly Pb^{2+} is used, but potential replacements are Sn^{2+} or Ge^{2+} , X is a monovalent halide anion. Perovskites have a cubic crystal structure, which is the optimal structure, with the B 6-fold and A 12-fold coordinated by X anions in BX_6 octahedra and AX_{12} cubo-octahedra, correspondingly. A classic perovskite structure is displayed in Figure 2.1. Goldschmidt and Octahedra’s tolerance factors, the relation shown in equations 2.1 and 2.2, respectively, are used to determine the equilibrium perovskite structure (Igbari *et al.*, 2019; Ke *et al.*, 2019; Nasti & Abate, 2020). The range of t for perovskites is $0.81 < t < 1.11$ and the range of μ is $0.44 < \mu < 0.90$ (Igbari *et al.*, 2019).

$$t = \frac{r_A + r_X}{\sqrt{2}(r_B + r_X)} \quad 2.1$$

Where it is assumed that the ions of A, B, and X are rigid spheres with ionic radii r_A , r_B and r_X , respectively. The values of ionic radii of Sn^{2+} , Pb^{2+} , FA^+ , MA^+ , Cs^+ , I $^-$, Br $^-$ and Cl $^-$ are 115 pm, 119 pm, 253 pm, 216 pm, 167 pm, 220 pm, 196 pm, and 184 pm, respectively (Nasti & Abate, 2020).

$$\mu = \frac{r_B}{r_X}$$

2.2

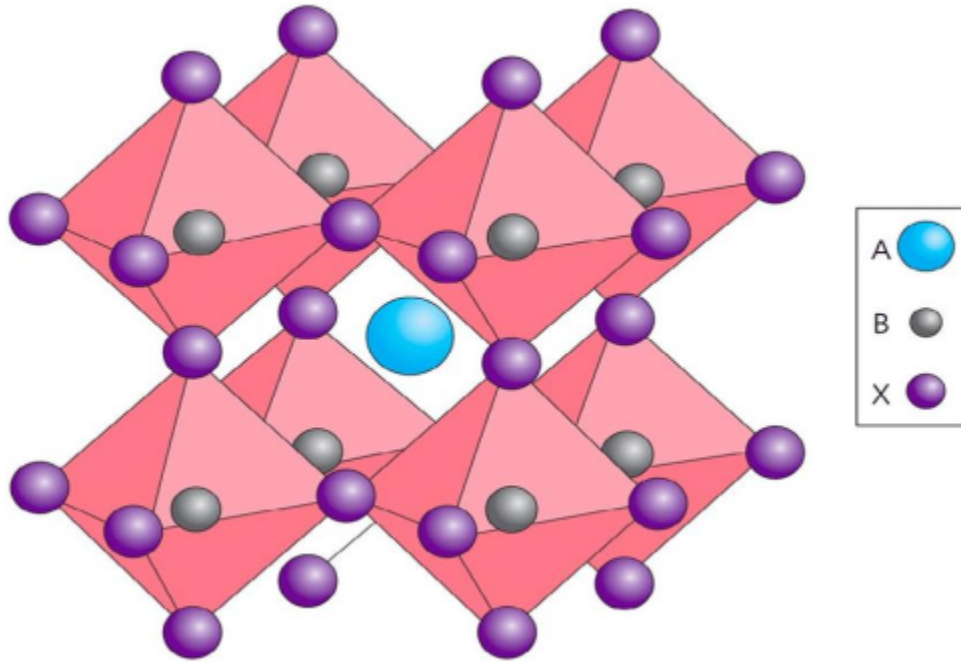


Figure 2.1. A typical perovskite structure (Sani *et al.*, 2018)

Lead replacement is further subdivided into two categories; heterovalent elements like Sb and Bi, and homovalent elements (homovalent elements have same valency as Pb element in this study) such as Ge and Sn (Z. Xiao *et al.*, 2019). The heterovalent lead replacement leads to mixed cation compounds such as $A_2B(I)B(III)X_6$, where A is an organic cation, B(I) is a monovalent cation and B(III) is a trivalent cation, X is a halide (Br, Cl), example $Cs_2AgBiCl_6$ (Nasti & Abate, 2020). $A_2B(I)B(III)X_6$ is also known as double perovskite absorber layer (Igbari *et al.*, 2019). The heterovalent replacements leads to poor optoelectronic behaviours of the perovskite since they reduce the dimensionality of the perovskites, hence demanding extra effort to make them fit for photovoltaic applications (Z. Xiao *et al.*, 2019). Homovalent replacement of lead include tin (Sn) and germanium (Ge), but they lead to reduced perovskite stability, but better electronic properties (Ke *et al.*, 2019). In this study, interest will be turned to the Sn as a potential Pb replacement, and since the research is developing from lead-PSCs, a short review of what has been achieved in Pb-PSCs is looked into.

2.2 Lead Perovskite Solar Cells (Pb-PSCs)

Kojima *et al.* (2006) first reported photovoltaic results for perovskites solar cells with a PCE of 2.2% from methylammonium lead bromide ($\text{CH}_3\text{NH}_3\text{PbBr}_3$) solar cells (Kojima *et al.*, 2006). Using iodine in place of bromine in the earliest perovskite solar cells, the PCE was improved to 3.8% (Kojima *et al.*, 2009). In both works, the group fabricated perovskite DSSCs with an organic electrolyte as a hole transporting medium and titanium oxide as the electron transporting medium (ETM), the devices were very unstable because of the dissolution of the perovskite absorber material in the electrolyte (Kojima *et al.*, 2009). However, it was noted that methylammonium lead iodide ($\text{CH}_3\text{NH}_3\text{PbI}_3$) had superior light harvesting properties as compared to the initially reported $\text{CH}_3\text{NH}_3\text{PbBr}_3$.

Im *et al.* (2011) were able to achieve 6.5% PCE after varying the TiO_2 thickness and using perovskite nanoparticles; they dissolved the nanoparticles in hole transporting medium (HTM) electrolyte, but it resulted in rapid degradation. In the year 2011, the organic electrolyte was substituted with a solid-state-HTM to solve the degradation problem, for example, Park's group (2012), replaced the electrolyte with solid-state spiro-MeOTAD which is a solid-state HTM and achieved an efficiency of 9% and improved stability (H. S. Kim *et al.*, 2012). The discoveries of solid-state HTM and better light harvesting perovskite ($\text{CH}_3\text{NH}_3\text{PbI}_3$) paved the way for advancement in research on Pb-PSCs.

More attempts to improve the stability and carrier transport of perovskites have been reported: e.g. mixing halides in perovskite films (I, Cl and Br), coating mp- TiO_2 surfaces with extremely thin perovskite films and substituting mp- TiO_2 with aluminium oxide (Al_2O_3), where Snaith's group achieved a PCE of 10.9% (M. M. Lee *et al.*, 2012). Since 2012, a lot of modifications on the perovskite layers, the ETL and HTL, and the devices' structure have been employed to improve the Pb-PSCs PCEs and stability. Burschka *et al.* (2013) fabricated planar PSCs by sequentially depositing PbI_2 followed by $\text{CH}_3\text{NH}_3\text{I}$, where they managed to control the perovskite morphology and got a PCE of 15% (Burschka *et al.*, 2013). In 2014, Im and the group used sequential deposition with different concentrations to control the perovskite cuboids and got an efficiency of 17.01%, due to improved light absorption as a result of controlling the cuboid sizes (Im *et al.*, 2014).

In 2015, the PCE of PSCs increased to 19.3% when Giordano *et al.* (2016) employed lithium to dope TiO_2 to improve the electronic properties of TiO_2 (Giordano *et al.*, 2016). For the first time

in 2015, MA⁺ in MAPbI₃ was substituted by FA⁺ and the efficiency of the device rose to 20.1% (Tumen-Ulzii *et al.*, 2021). In 2016, a poly(methyl methacrylate) (PMMA) template was used to regulate the crystallization and nucleation of (FAI)_{0.81}(PbI₂)_{0.85}(MAPbBr₃)_{0.15} to form high-quality perovskites and the efficiency achieved was 21.6%; this work showed how important the property of perovskite films is to PSCs performances (Bi *et al.*, 2016). In 2018, planar devices were fabricated with tin oxide (SnO₂) as the ETL, the ETL was modified by Ethylene diamine tetraacetic acid (EDTA) to improve its optoelectronic properties and an efficiency of up to 21.6% was reached, the devices were also stable and lost only 8% of their PCE after 2880 h (D. Yang *et al.*, 2018).

Q. Jiang *et al.* (2019) introduced perovskite surface passivation by using phenethylammonium iodide (PEAI) on the surface of a perovskite absorber containing a combination of MA⁺ and FA⁺ cations. The group realized that the PEA layer formed on the perovskite's surface, passivated the surface imperfections on the perovskite films, and thus suppressed trap-assisted recombination, which is always unfavorable to the performances of PSCs. The group achieved a PCE of 23.32% with a high V_{oc} of 1.18 V, which is nearby to the Shockley-Queisser limit of 1.25 V (Q. Jiang *et al.*, 2019). The PCE of Pb-PSCs continued to increase with the highest reported PCE being 26.1% (D. Li *et al.*, 2023), and the certified PCE standing at 26.1% as at 2023 (“NREL Best Research-Cell Efficiency Chart”, 2022). It is vital to take into account that perovskite film quality, ETL and HTL modification are beneficial in improving PSCs efficiencies and stability.

2.2.1 Challenges and Possible Solutions for Lead Halide PSCs

The PCE of lead-based PSCs is approaching the theoretically projected thermodynamic maximum efficiency of ~31% (Saliba *et al.*, 2018; Guo *et al.*, 2022). The high efficiency shows that lead-based PSCs can now be commercialized and compete favourably with other solar technologies like silicon-based technology. But the main challenge of lead-based PSCs is the highly toxic lead component (Min *et al.*, 2022); lead-based perovskites readily decompose when exposed to water to result in toxic solutions (Igbari *et al.*, 2019). The decomposition process of lead-based perovskite films, when exposed to moisture or water, is summarized in Figure 2.2.

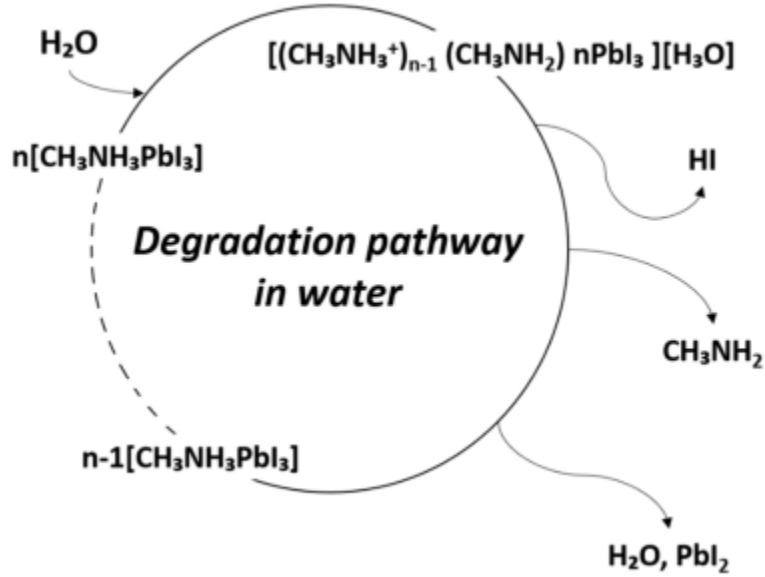


Figure 2.2. Decomposition mechanism of lead-based perovskite films (D. Kim *et al.*, 2020).

Some researchers suggest that atmospheric moisture acts as a catalyst to accelerate the degradation of $MAPbI_3$ into aqueous CH_3NH_2 , HI , and PbI_2 which is solid (L. Zhang *et al.*, 2016); these compounds can further degrade into HI , I_2 , CH_3NH_2 and Pb clusters (Babayigit *et al.*, 2016). PbI_2 is toxic and highly soluble in water ($\approx 761 \text{ mg L}^{-1}$); the dissolved PbI_2 can eventually leak into the environment even if the devices are fully encapsulated, this makes it difficult for safe long-term use of Pb -perovskite photovoltaic devices (J. Liu *et al.*, 2023). Pb is therefore a danger during the fabrication, use and disposal of Pb -based solar technology devices (Cui *et al.*, 2021). Therefore, there is a need for the replacement of Pb in the PSCs with nontoxic or less toxic elements. Possible Pb replacement includes copper (Cu), bismuth (Bi), Sn , and germanium (Ge) elements (Igbari *et al.*, 2019; W. Liao *et al.*, 2016). However, most research is concentrated on Sn as an appropriate potential replacement for Pb because Sn -perovskites have ideal electrical and optical properties for photovoltaic applications (J. Cao *et al.*, 2019). In addition, it has been shown that Sn -perovskites have some better optoelectrical properties similar to that of Pb -perovskite (Kayesh *et al.*, 2018). Sn -perovskites have high light absorption ability, a small bandgap of between $1.2 - 1.4 \text{ eV}$, and a high charge carrier mobility ($500 \text{ cm}^2 V^{-1} s^{-1}$) (Cui *et al.*, 2021; He *et al.*, 2020; P. Li *et al.*, 2020).

2.3 Tin-Perovskite Solar Cells (Sn-PSCs)

The toxicity of Pb is the primary challenge in the commercialization of PSCs technology. Sn-perovskite is considered less toxic and can accelerate the commercialization idea of PSCs technology (Lanzetta *et al.*, 2021). The energy band gap of Sn-perovskite is ~1.3-1.4 eV, which can enable it to absorb a wide spectrum of solar radiation and generate high short-circuit current; and because of its band gap, the PCE of Sn-PSCs is theoretically predicted that it can reach ~32% Shockley-Queisse efficiency limit (Sanchez-Diaz *et al.*, 2022). The high theoretically predicted PCE makes Sn-perovskite a better option as an absorber material in PSCs technology.

The first hybrid organic-inorganic Sn-PSCs was reported by Snaith's group in 2014 (Noel *et al.*, 2014). The group used methylammonium tin iodide (MASnI₃) and they achieved an efficiency of 6.4 % with poor stability. The record efficiency for Sn-PSCs was achieved in 2021 when B. Yu *et al.* (2021) achieved an efficiency of 14.81% with a certified PCE of 14.03%. The PCE and long-term durability of Sn-PSCs are stagnantly low as compared to the Pb-PSCs counterpart. In the subsequent sections of this study, the cause for the low PCE and stability, and the outstanding works done to advance the PCEs and stability of Sn-PSCs are considered.

2.3.1 Degradation mechanisms of tin-perovskites in the ambient environment

Tin is the most promising substitute amongst the possible materials to replace lead in the organic hybrid perovskite systems. However, the inferior ambient condition stability of tin-perovskites impedes the development of devices with competitive performances (Lanzetta *et al.*, 2021). The stability issues of Sn-perovskites primarily originate from the facile creation of Sn⁴⁺ due to Sn²⁺ oxidation (S. J. Yang *et al.*, 2021). The Sn⁴⁺ created in the perovskite is harmful to the PCE and stability of Sn-PSCs as it forms centers for nonradiative recombination of the photogenerated charges within the device (L. Xu *et al.*, 2021). Thus, scientists must oblige to understand the decomposition process of tin-perovskites to counter the stability issues and increase the PCE of Sn-PSCs.

The degradation mechanisms of tin-perovskites have not yet been robustly understood like their lead counterpart. A few researchers through various studies have tried to explain how tin-perovskites degrade in the ambient environment. ASnX₃ upon exposure to air and moisture (which are considered the main degrading agents) can degrade to A₂SnX₃ and SnO₂, the degradation

products of tin perovskite in the air such as SnO_2 make tin perovskite less toxic since the product is water/moisture insoluble and also inert (J. J. Cao *et al.*, 2022). Other studies have shown that the perovskite can decompose into a mixture of an organic cation iodide (such as FAI or PEAI), SnI_4 , and SnO_2 (Z. Lin *et al.*, 2021; Savill *et al.*, 2021; L. Xu *et al.*, 2021). Figure 2.3 is a summary of the possible degradation routes for tin-perovskites: (1) Formation of SnI_4 after ASnI_3 interactions with atmospheric oxygen and endogenously formed iodide (this is iodide vapour resulting from the sublimation of iodide within the perovskite film); (2) Formation of solid-state A_2SnI_6 resulting from AI and SnI_4 reaction; (3) HI formation after hydrolysis of SnI_4 by H_2O ; (4) I_2 creation after reaction of HI and O_2 ; and (5) I_2 aided oxidation of Sn-perovskite and SnI_4 formation (Savill *et al.*, 2021). For an iodide-based tin-perovskite, the cyclic degradation is a result of aggravated degradation resulting from the presence of the iodine (Lanzetta *et al.*, 2021).

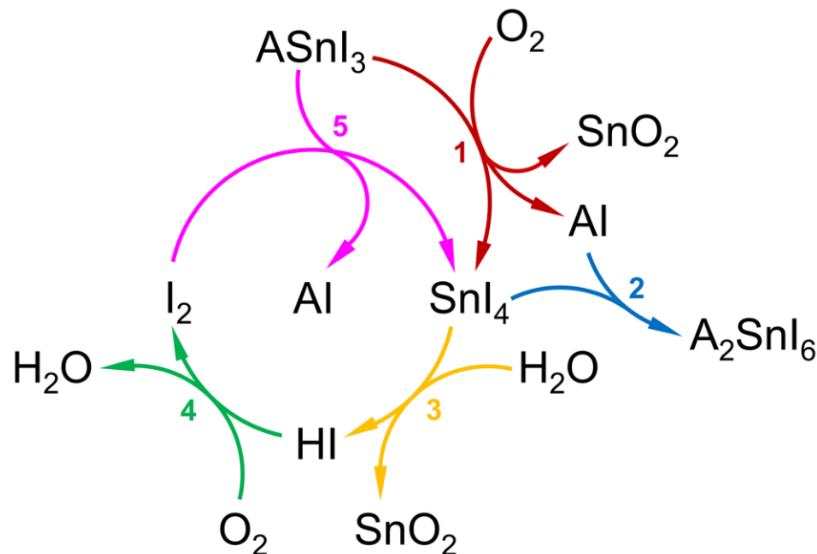
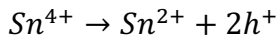


Figure 2.3. Predicted degradation routes of tin-perovskite in the ambient environment (Lanzetta *et al.*, 2021).

2.3.2 Electronic impact of the instability of tin-perovskite

The primary challenge in fabricating high-performing Sn-PSCs is the sudden oxidation of Sn^{2+} to Sn^{4+} in Sn-perovskites. Sn^{4+} formation can be due to exposure of the perovskite to oxidizing agents or due to lattice instability. Sn^{2+} oxidation is unfavoured in the bulk Sn-perovskite according to Angelis group's prediction in 2020 (Ricciarelli *et al.*, 2020). It therefore implies that Sn^{4+} in the bulk perovskite transforms to Sn^{2+} and as a result release holes to the valence band as shown in the chemical equation 2.3 and Figure 2.4. The released holes, p-dope the perovskites and result in what

is known as self-p-doping in Sn-perovskites; self-p-doping magnifies nonradiative charge recombination by increasing the background hole carrier density to $\sim 10^{20} \text{ cm}^{-3}$ (Milot *et al.*, 2018). The Sn^{2+} oxidation is favoured in the non-passivated perovskite surface resulting in charge trap centers and by extension nonradiative recombination in Sn-perovskite devices. Both p-doping and Sn^{2+} oxidation are sources of charge traps and hence the low performance of Sn-PSCs. Sn-perovskites containing Sn^{4+} have poor optoelectronic properties and hence result in low PCE if used as photovoltaic absorber materials.



2.3

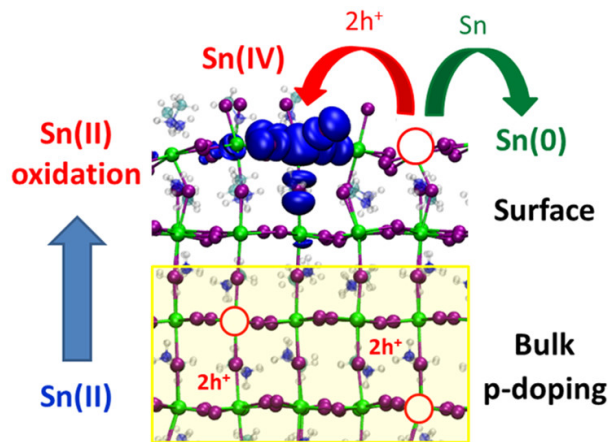


Figure 2.4. A summary of the oxidation process in Sn-perovskites (Ricciarelli *et al.*, 2020)

2.4 Improving the Photovoltaic Properties of Sn-PSCs

In the hope of commercialization of Sn-PSCs researchers have employed many techniques to advance both the durability and PCE of Sn-PSCs. Some of the techniques used include device architectural engineering, film morphology control, use of additives and co-additives, mixing of organic components of the perovskite/perovskite engineering, and perovskite dimensionality engineering. The successes of the use of these approaches are examined in the succeeding subsections.

2.4.1 Architectural Engineering of Sn-PSCs

The conventional PSCs configuration is the n-i-p, which involves the incorporation of mesoscopic TiO₂ as ETL and spiro-MeOTAD as HTM. TiO₂ ETL has produced some of the best-performing PSCs (Alharbi *et al.*, 2019; E. H. Jung *et al.*, 2019); it is however faced with several challenges such as its electron mobility is not high enough to enhance further improvements in PSCs PCEs. TiO₂ is unstable under light and degrades if illuminated with ultraviolet light leading to degradation of PSCs; also, TiO₂ requires high-temperature processing to remove the unwanted organics during its deposition-this can lead to high production cost, which can discourage commercialization of PSCs (L. Lin *et al.*, 2020; Xiong *et al.*, 2018). The optoelectronic properties of spiro-MeOTAD are also enhanced by the use of dopants; one of these dopants is lithium bistrifluoromethanesulfonimide (LiTFSI) (Suzuki *et al.*, 2016). One of the primary challenges of LiTFSI is its hygroscopicity, which means it absorbs any traces of moisture from its surrounding (Y. Zhang *et al.*, 2021); this can hasten the degradation of perovskite absorber layer since the perovskite and spiro-MeOTAD are in contact in a complete solar cell. Therefore, it is obligatory to change the PSCs architect to advance both the stability and PCE of Sn-PSCs.

Figure 2.5 illustrates the collective efforts researchers are making in the engineering of Sn-PSCs structure (Sun *et al.*, 2021). FTO-coated glass/compact TiO₂/mesoporous TiO₂/CH₃NH₃SnI₃/Spiro-MeOTAD/Au was the structure of the first reported Sn-PSCs (Noel *et al.*, 2014). Because of the presence of the Spiro-MeOTAD and TiO₂, the stability and PCE of Sn-PSCs were low; the devices degraded in a minute upon exposure to atmospheric conditions and the performance was only 6.4% (Noel *et al.*, 2014; Y. Zhang *et al.*, 2021). To eliminate the effects of spiro-MeOTAD, the p-i-n (ITO/ PEDOT:PSS/FASnI₃/fullerene(C60)/BCP/Ag) architecture was first reported (W. Liao *et al.*, 2016). Liao and the group achieved an efficiency of 6.22%, but with improved stability. Liao's work became a pivot for revolutionizing Sn-PSCs research. Many researchers have now employed the p-i-n structure and outstanding efficiencies of between 10 and 14% and better stability are reported (J. J. Cao *et al.*, 2022; Chen *et al.*, 2022; Zhou *et al.*, 2022; Z. Zhu *et al.*, 2022).

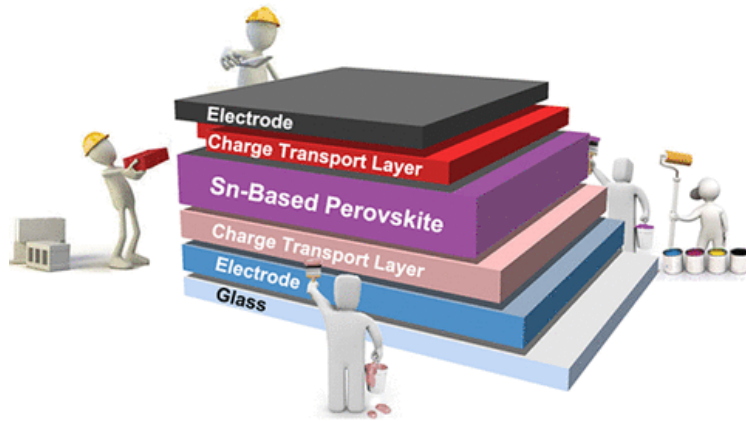


Figure 2.5. An illustration concerted efforts researchers are putting on designing stable and high performing Sn-PSC structure (Sun *et al.*, 2021)

2.4.2 Film Morphology

Most of the tin-perovskites are solution-processed. Solution-processed tin-perovskites are marred with poor film coverage due to unpredictable crystallization during film formation (Girolamo *et al.*, 2021; Hao *et al.*, 2015; F. Li *et al.*, 2021). The reaction leading to the formation of Sn-perovskite film is faster as compared to the reaction of formation of Pb-perovskites; this results to the creation of a nonhomogeneous Sn-perovskite film over a large area (Liang & Gao, 2018). Thus, it is critical to control the crystallization of Sn-perovskite to form homogeneous and pinhole-free films. The retardation process can be achieved by allowing the perovskite to form in a stepwise manner; that is the development of an in-between phase before the full crystallization of the perovskite (Ke *et al.*, 2019).

The commonly used perovskite solvents include dimethylformamide (DMF) and dimethyl sulfoxide (DMSO) (Ke *et al.*, 2019). Other solvents such as γ -butyrolactone (GBL) and N, N-dimethylacetamide (DMA) are also sparingly used (M. Jung *et al.*, 2019); and so, emphasis will be on the use of DMF and DMSO. Tin iodide (SnI_2) has poor solubility in DMF and hence can lead to the creation of low-quality Sn-perovskite films full of pinholes and having a rough morphology if used as the sole solvent (Ke *et al.*, 2019). DMSO on the other hand has a strong coordination effect and is capable of retarding the interactions between SnI_2 and MAI/FAI during film formation (X. Jiang *et al.*, 2021) and can lead to the creation of the much-needed intermediate phase identified as $\text{SnI}_2 \cdot 3\text{DMSO}$ which retards the rapid crystallization rate of Sn-perovskite (Hao *et al.*, 2015;

Zhao *et al.*, 2017). According to an observation, SnI₂.3DMSO manifests in a pale-yellow color before annealing, but after annealing the colour of the film changes to black symbolizing the formation a Sn-perovskite film (Hao *et al.*, 2015). However, DMSO has a high viscosity and can be difficult to spin-coat during the deposition process (Hao *et al.*, 2015; X. Liu *et al.*, 2018). Therefore, researchers have resorted to mixing DMSO and DMF in a predetermined ratio of 1:4 to deposit defect-free Sn-perovskites films, where DMF is used as a dilutor of DMSO (X. Liu *et al.*, 2018).

The mixing of solvents to form a uniform film is known as solvent engineering. A complete solvent engineering process entails the application of antisolvents during the spin coating process; the commonly used antisolvents include ethyl acetate (EA), chlorobenzene (CB), diethyl ether (DE), methyl acetate (MA), iodobenzene and toluene (TL) (Bandara *et al.*, 2019; M. Jung *et al.*, 2019; X. Liu *et al.*, 2018; Zhao *et al.*, 2017). The antisolvent is dripped during spin coating as displayed in Figure 2.6. The antisolvent must be mixable with the used solvent but must not wash away the perovskite layer.

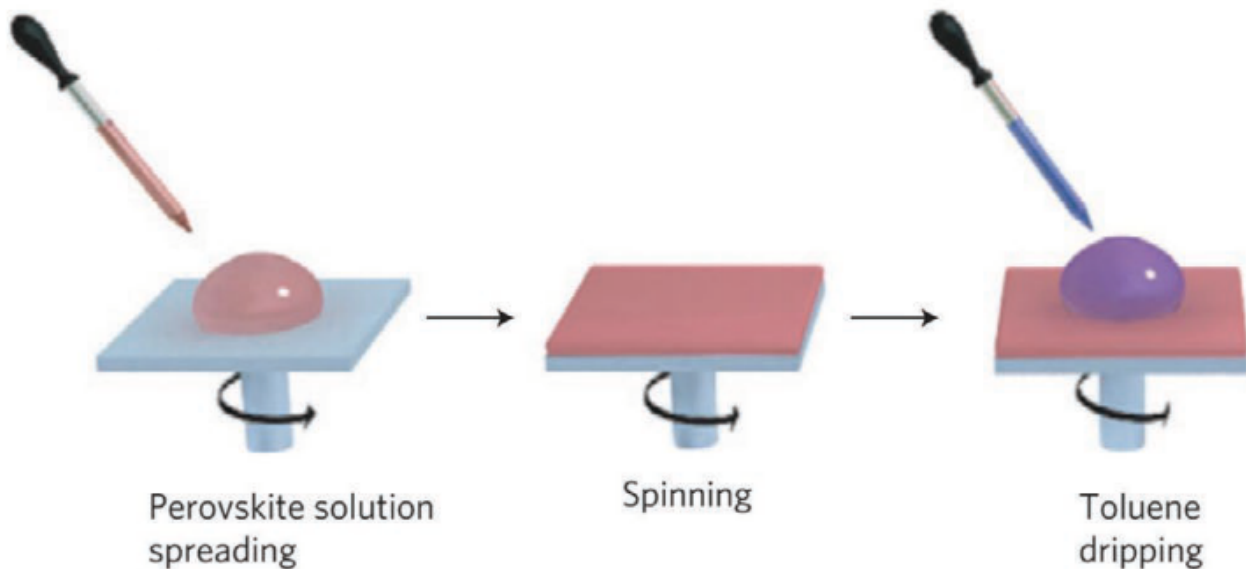


Figure 2.6. An illustration of how to use the antisolvent (Jeon *et al.*, 2014).

Perovskite film development is a combination of nucleation and crystal growth. Depositing a compact layer of the perovskite film requires a concentrated number of nucleation sites and a slow growth rate (X. Liu *et al.*, 2018). The antisolvent flushes all the solvents in the precursor and leaves

a supersaturated precursor with a high number of nucleation sites on the substrate (Konstantakou *et al.*, 2017). The antisolvents also reduce the rate of crystallization by reducing the reaction speed between SnI₂ and FAI/MAI (Jeon *et al.*, 2014). The antisolvents are good for the formation of highly crystallized films, but care must be taken in choosing the right one, as noted by Liu *et al.* (2018), the film quality is correlated to the antisolvent used to a large degree (X. Liu *et al.*, 2018). Having high-quality films is essential in Sn-PSCs, by using the solvent engineering technique the efficiency of Sn-PSCs has leaped from the 6.2% to above 14% (X. Jiang *et al.*, 2021).

2.4.3 Use of additives and co-additives

An absorber film quality plays a primary function in the enhancement of a solar cell PCE. To advance the PCE of Sn-PSCs, the film quality of the perovskite must be remarkably good (Z. Zhu *et al.*, 2022). Researchers have employed additive engineering to perovskite precursor solutions to subdue the facile oxidation of Sn²⁺ ions in tin perovskite films and solar cells to enhance Sn-perovskite film and solar cell stability (W. Yu *et al.*, 2022). The incorporation of additives into Sn-perovskites dates back to 2013 when SnF₂ additive was used to suppress the oxidation of Sn²⁺ and inhibit the metallic conductivity caused by the formation of Sn⁴⁺ in the Sn-perovskite film (Kayesh *et al.*, 2018; Kumar *et al.*, 2014). It was noted that the inclusion of SnF₂ into the precursor solution does not result in a notable change in the Sn-perovskite film lattice parameters; this is because fluoride (F⁻) anions have a smaller ionic radius (1.33) as likened to the iodide (I⁻) in anion (2.20), and hence cannot substitute I⁻ (Kumar *et al.*, 2014).

Researchers have shown that apart from inhibiting Sn²⁺ oxidation, SnF₂ aids the crystal growth of Sn-perovskite films; SnF₂ has a limited solubility hence it will precipitate quickly during the spin-coating process (M. Xiao *et al.*, 2018). The resulting SnF₂ particles result in more nucleation sites and hence aid in the formation of homogenous and compact films (M. Xiao *et al.*, 2018). However, researchers have noted that an excess of SnF₂ is destructive to the morphology of the perovskite layer, the excess leads to phase segregation observed on Sn-perovskite film surfaces (W. Liao *et al.*, 2016). The creation of unwanted phases on an absorber surface is detrimental as it results in carrier charge trapping and hence reduction in lead-free perovskite films (Igbari *et al.*, 2019).

SnF₂ has proven important in making of Sn-PSCs and therefore it is only necessary to get rid of the unwanted phases that come with excess SnF₂. The coordination chemistry of SnF₂ and other compounds has been extensively studied since 2016; particularly for application in the

enhancement of both stability and performance of Sn-PSCs (Liang & Gao, 2018; G. Liu *et al.*, 2020; Pascual *et al.*, 2021; X. Xu *et al.*, 2017). In 2016, Seok's group became the first research group to investigate the interaction of SnF₂ and other compounds (commonly known as co-additives) where they used pyrazine to homogeneously disperse the excess SnF₂ through the formation of SnF₂-pyrazine complex (S. J. Lee *et al.*, 2016). The group noted that the complex enriched the morphology of the absorber and reduced the ease of oxidation of Sn²⁺; they achieved a performance of up to 4.8% and improved stability, and the solar cells retained up to 98% of their PCEs after 100 days of storage (S. J. Lee *et al.*, 2016).

Since Lee and co-workers work, so many researchers continue to employ the co-additive method to further the durability and PCE of Sn-perovskite devices. In 2019, Cao and coworkers combined tin chloride (SnCl₂) and ammonium hypophosphite (NH₄H₂PO₂) to fabricate efficient Sn-PSCs (J. Cao *et al.*, 2019). SnCl₂ works in a similar way as SnF₂, it inhibits the oxidation of Sn²⁺, but results in phase aggregation when used in excess just like SnF₂ (J. Cao & Yan, 2021). NH₄H₂PO₂ was used by the group to get rid of the detrimental unwanted phases created by SnCl₂ and also acted as a reducing agent that could prevent the facial oxidation of Sn²⁺ (J. Cao *et al.*, 2019). NH₄H₂PO₂ contains H₂PO₂⁻ component, which interacts with SnCl₂ to produce a complex salt, which passivated the Sn-perovskite grain boundaries and lowered the charge trap densities; the approach led to devices achieving a PCE of 7.3%, the devices retained 70% of their PCEs being kept in a nitrogen environment for 1000 hours (J. Cao *et al.*, 2019).

In 2020, Ning's group used ammonium thiocyanate (NH₄SCN) as a co-additive to control perovskite film orientation and modify crystal growth; they achieved an efficiency of up to 12.4% with an improved V_{oc} of 0.94 V (X. Jiang *et al.*, 2020). The high V_{oc} was linked to decrease in defects concentration in the perovskite films. The group also noted that the NH₄SCN-based Sn-PSCs were stable, retaining up to 90% of their PCEs for over 3800 hours (X. Jiang *et al.*, 2020). The use of a co-additive approach is important, as it has enabled much progress in Sn-PSCs PCE and stability.

2.4.4 Mixing of organic cations

The primary challenge of Sn-perovskite is its vulnerability to oxygen and moisture. Therefore, in fabricating Sn-perovskite films the organic cations must be chosen carefully to effectively protect the film from impending degradation arising from the ambient atmosphere. Researchers have

resorted to mixing the commonly used organic cations (FA^+ and MA^+) to upsurge the photovoltaic properties and stability of Sn-PSCs (F. Wang *et al.*, 2018). FASnI_3 is much more stable due to its high defect-formation energy (S. J. Yang *et al.*, 2021) at room temperature as compared to MASnI_3 (Ke *et al.*, 2019); the oxidation rate of FASnI_3 is slower as compared to MASnI_3 (S. J. Lee *et al.*, 2016; Z. Zhu *et al.*, 2018). Zhao *et al.* (2017), noted that cation mixing is essential in improving the V_{oc} and PCE of Sn-PSCs due to better film morphology and reduced nonradiative recombination resulting from charge trap centers caused by pinholes in poorly formed films (Zhao *et al.*, 2017). B. Yu *et al.* (2020) demonstrated that incorporating MA^+ into FASnI_3 film dramatically increased the orientation and crystallization of the FASnI_3 film (B. Yu *et al.*, 2020); this shows that MASnI_3 is highly crystalline and well-oriented (F. Li *et al.*, 2021). In addition, MASnI_3 has a smaller bandgap and can thus help in reducing the band gap of FASnI_3 (1.4 eV) to help improve the optical absorbance range properties of the perovskite films (Konstantakou & Stergiopoulos, 2017). Thus, by using the FA/MA cations mixture, a relatively stable and better-performing device is achievable.

2.4.5 Dimensionality Adjustment in Sn-Perovskite Absorber Material

Sn-perovskites materials mostly applied in photovoltaics exist in the 3D crystal lattice structure with the general formula of ABX_3 . The 3D perovskites are appealing in fabricating solar cells because of their superb light-absorbing properties (Shao *et al.*, 2018). However, the device's stability is compromised by the hydrophilic nature of the cations (FA^+ and MA^+) present in the 3D structure (W. F. Yang *et al.*, 2020). To improve the stability of such devices; researchers have incorporated low dimensional hydrophobic perovskites known as 2D Sn-based Ruddlesden-Popper (R-D) into the 3D Sn-perovskite absorbers, leading to the creation of 2D-quasi-2D-3D perovskite as shown in Figure 2.7 (D. H. Cao *et al.*, 2017; Jokar *et al.*, 2018, 2019; F. Wang *et al.*, 2018; H. Xu *et al.*, 2019). The stability is improved by the 2D perovskite through 'nanoscale' encapsulation (F. Wang *et al.*, 2018). The 2D perovskite are hydrophobic in nature and have high formation energy; this improves their stability against atmospheric moisture (P. Li *et al.*, 2020).

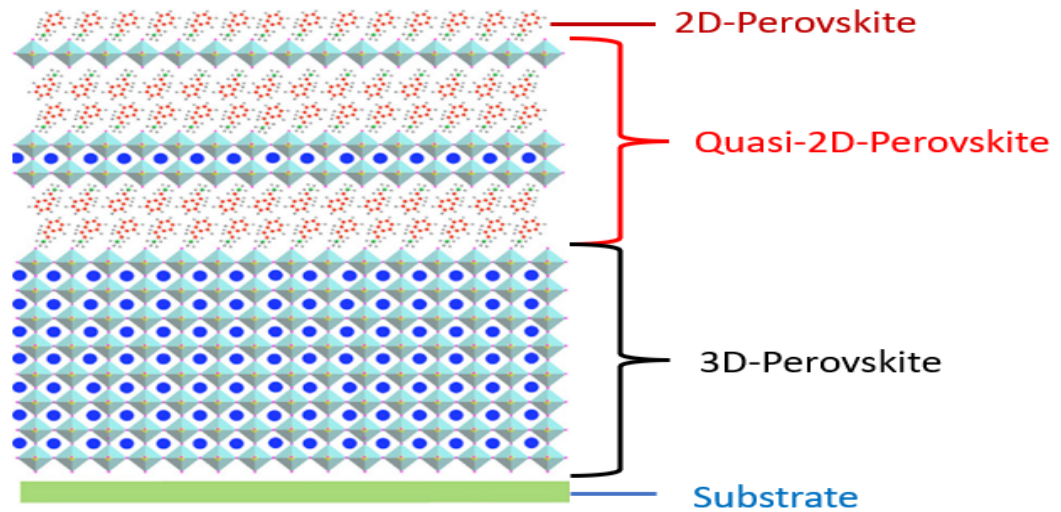


Figure 2.7. 2D-quasi-2D-3D perovskite resulting from depositing a bulky ammonium cation on the 3D perovskite absorber (F. Wang *et al.*, 2018). The same structure also is formed if a bulky ammonium cation is included in the Sn-perovskite precursor.

2D Sn-based Ruddlesden – Popper (R-P) perovskites are formed if a bulky hydrophobic monovalent ammonium cation, such as phenyl ethylammonium (PEA^+), butylamine BA^+ , among others, is added to the 3D perovskite precursor solution or casted on 3D perovskite films, leading to formation of stacks of 2D perovskites. The general formula of 2D perovskites is $\text{A}_2\text{B}_{n-1}\text{SnI}_{3n+1}$, where A represents an organic spacer cation separating inorganic octahedral layers (SnI_6), B is a small organic cation (MA or FA, or the mixture of FA and MA), $\langle n \rangle$ is the number of octahedral sheets sandwiched between two organic interlayers (F. Li *et al.*, 2020; H. Xu *et al.*, 2019). From the results of different research groups, the addition of 2D perovskite into the 3D-perovskite has led to an enhancement in PCEs, stability, and reproducibility of tin-PSCs (X. Jiang *et al.*, 2020; Y. Liao *et al.*, 2017; Rath *et al.*, 2019; Shao *et al.*, 2019; Yuan *et al.*, 2019). The improved tin-PSCs stability is related to the hydrophobic nature and passivation ability of 2D perovskites (D. H. Cao *et al.*, 2017; Jokar *et al.*, 2018).

The 2D amounts added into the 3D perovskite must be moderate as excess can lead to film quality deterioration, which eventually create shunt paths and hence lower the PCE of Sn-PSCs (Shao *et al.*, 2018). 2D Sn-perovskites have a modest PCE thus the need to combine it with the 3D perovskite in small quantities (D. H. Cao *et al.*, 2017). The use of mixed 3D/2D Sn-perovskite absorber layers has led to Sn-PSCs with good efficiencies ranging between 8% and 14%, which is a good leap in the development of Pb-free perovskite PV systems (X. Jiang *et al.*, 2020; Jokar *et al.*, 2019; H. Xu *et al.*, 2019; B. Yu *et al.*, 2021).

Researchers agree that 3D tin perovskite films have poor morphology, and are unstable due to the hydrophilic properties of FA and MA (D. H. Cao *et al.*, 2017; Shao *et al.*, 2018; F. Wang *et al.*, 2018). The 3D tin-perovskite films due to rapid crystallization have grains with sharp boundaries which lead to increased structural defects concentration in the perovskite absorber material (Igbari *et al.*, 2019; Ke & Kanatzidis, 2019); the defects along the grain boundaries reduce the PCE of the photovoltaic devices by acting as charge trap centers leading to increased nonradiative recombination of photogenerated charges. According to Snaith's and Loi's groups, the addition of an insignificant amount of 2D bulky ammonium ions helps in fusing the grains of 3D tin perovskite to get rid of the harmful grain boundaries (Shao *et al.*, 2019; Z. Wang *et al.*, 2017). X. Jiang *et al.* (2020), report that the addition of the right amount of 3D PEA into the FASnI₃ film absorber leads to an improvement in open circuit voltage in Sn-PSCs, which they attributed to reduced structural defect density along the grain boundaries (X. Jiang *et al.*, 2020). Wang and coworkers noted that the addition of large organic molecules on top of 3D FASnI₃ leads to an encapsulation effect by the formation of low-dimensional perovskite inserted between large organic molecules (F. Wang *et al.*, 2018). From the mentioned works, it is clear that the incorporation of 2D bulky ammonium cation can help improve the film properties and the PCE of PSCs by minimizing the defect densities.

The commonly used solvents in preparing Sn-perovskites precursor solutions are DMF and DMSO, and in most cases, the DMSO is diluted with DMF at a ratio of 1:4. D. H. Cao *et al.* (2017) noted that the solvent used in preparing the bulk perovskite precursor containing BA, MA, and triethylphosphine (H₃PO₂) and SnF₂ determines the film growth and orientation (H₃PO₂ and SnF₂ were used as additives) (D. H. Cao *et al.*, 2017). The films were oriented parallel to the substrate when a 100% DMSO was used as the solvent, and perpendicularly to the substrate when the ratio of DMF:DMSO was 4:1; the conclusion was based on XRD and GIWAX measurements. From the XRD pattern, the parallel orientation is revealed by the (0h0) planes, h is an integer, and the (111) and (202) planes show perpendicular orientation. The alignment of the bulky ammonium cation influences the charge dynamics in the perovskite film hence the need to know the right solvent to use to get an appropriate orientation for better PCEs of Sn-PSCs.

The 2D perovskite layers act as platelets within the 3D perovskite layers. The 2D perovskite acts as an insulator if oriented in a parallel direction within the 3D perovskite. The insulation aspect

reduces charge mobility, and increases charge accumulation at the perovskite/ETL interface, resulting to amplified bimolecular recombination of photogenerated charges, which is detrimental to the performance of PSCs (Quan *et al.*, 2016). The PCE is significantly increased if the platelets are oriented vertically since the 3D blocks are oriented vertically to favour charge transfer and reduce recombination (H. Xu *et al.*, 2019). Therefore, by using the 2D ammonium cation appropriately the PCE and stability of Sn-PSCs is increased.

In summary, a number of groups have tried several approaches to improve the stability and PCE of Sn-PSCs. The techniques used include: use of additive engineering, use of solvent engineering, compositional engineering and dimensionality adjustments of the perovskite layer, and architectural manipulation of the solar cells. However, despite these efforts, the efficiency and stability of Sn-PSCs still remains inferior. Therefore, there is need of more research to identify the best additives to improve both the PCE and the stability of Sn-PSCs. Also, during the architectural engineering, many researchers have commonly used BCP as a cathode interfacial layer, but research has shown that the electrical properties of BCP is thickness sensitive. The thickness sensitivity of BCP layer, makes it difficult to fabricate and reproduce high performing devices. Thus, there is need to seek for alternative buffer layers. The alternative buffer layer should not be thickness sensitive and also should have higher electrical conductivity to ensure better ohmic contact and better charge flow between the ETL and the cathode.

CHAPTER THREE

THEORETICAL BACKGROUND

3.1 Ostwald Ripening

Sn-PSCs are expected to realize outstanding PCEs since they bear exceptional optoelectronic characteristics. However, the primary drawback is the hurried crystallization of Sn-perovskites, which leads to small grain sizes with rough surfaces; which has negative effects on the PCEs of Sn-PSCs (Cui *et al.*, 2021). Large grains are necessary in improving the performance of Sn-PSCs as they help in minimizing defects originating from grain boundaries. More often, the solution processing of Sn-perovskite is based on a cold precursor solution. The main motive for this is that the cold precursor solution results in "sparsely" distributed nuclei during film deposition allowing for space for grain growth during the thermal treating process (M. Jung *et al.*, 2019).

The growth of the small grains into large grains is aided by the decomposition of the smallest grains, which eventually collapse into relatively large grains in a process known as Ostwald ripening (M. Jung *et al.*, 2019). Ostwald ripening depends on the solubility of nanoparticles depending on their sizes; small particles due to their high chemical potential or surface energy tend to dissolve in the residual solvents such as DMSO which has relatively low evaporation and redepositing themselves onto the larger particles. This leads to the disappearance of the smaller particles and the further growth of large particles with low surface energy. The process involves matter transfer to large grains from small grains through intermediate mobile species, accelerated by the size-dependent stability of the grains. Cold precursors and low processing temperatures accelerate the ripening (Cui *et al.*, 2021). Ostwald ripening helps in depositing pinhole-free absorber layers and therefore improves the PCE of Sn-PSCs. The ripening can be investigated by doing the morphological analysis of perovskite films before and after annealing.

3.2 Urbach Energy (Absorption Band Tail) of Perovskite Absorber Material

The optical absorption spectra of perovskite films are important in determining their band gap and dimensionality. The absorption spectra of perovskites are divided into three sub-regions; the weak absorption region originating from defects within the absorber, the absorption edge region arising from perturbation of disorder and structure of the material, and the strong absorption region where

the band gap is estimated (Hassanien & Akl, 2016). The absorption coefficient (α) of perovskites absorber materials can be calculated using $\alpha = 2.303A/d$, where A is the absorbance data from the UV-Vis spectrophotometer; this data can be plotted against the photon energy, and band gap of a material approximated from the graph. There is an exponential region along the absorption coefficient curve, just before the optical band gap, this region is known as the Urbach tail (Kaiser *et al.*, 2021). The Urbach tail strongly appears in poorly crystallized semiconductors, amorphous semiconductors, and semiconductors with structural disorders. The tail appears in such semiconductors because of localized states, which extend into the band gap (Hassanien & Akl, 2016).

The correlation between the absorption coefficient, band gap, and photon energy is given by equation 3.1, known as Urbach empirical rule (S. Wang *et al.*, 2023). The Urbach energy (E_U) of a semiconductor can be calculated using equation 3.1, (after some algebra as shown below to equation 3.3). Urbach energy is important in comparing the structural defects within a semiconductor after the addition of an additive or after surface passivation (X. Jiang *et al.*, 2020; S. Wang *et al.*, 2023).

$$\alpha = \alpha_0 \exp\left(\frac{hv - E_g}{E_U}\right) \quad 3.1$$

Where α is the absorption coefficient, E_g is the band gap of the absorber material, hv is photon energy and E_U is the Urbach energy.

$$\frac{\alpha}{\alpha_0} = e^{\left(\frac{hv - E_g}{E_U}\right)}$$

$$\ln\left(\frac{\alpha}{\alpha_0}\right) = \ln\left(e^{\left(\frac{hv - E_g}{E_U}\right)}\right)$$

$$\ln\left(\frac{\alpha}{\alpha_0}\right) = \left(\frac{hv - E_g}{E_U}\right) \ln e$$

$$\ln\left(\frac{\alpha}{\alpha_0}\right) = \left(\frac{hv - E_g}{E_U}\right)$$

$$\ln\alpha - \ln\alpha_0 = \frac{hv}{E_U} - \frac{E_g}{E_U}$$

$$\ln\alpha = \frac{hv}{E_U} - \frac{E_g}{E_U} + \ln\alpha_0 \quad 3.2$$

$\frac{E_g}{E_U} + \ln\alpha_0$ in equation 3.2 are constants, therefore equation 3.2 can be treated as a straight-line graph equation ($y = mx + c$) and written as:

$$\ln\alpha = \frac{1}{E_U} hv + c \quad 3.3$$

From equation 3.3, Urbach Energy (E_U) is the reciprocal of the slope of the linear part of the graph of $\ln\alpha$ vs hv .

3.3 Power Conversion Efficiency (η) of a Photovoltaic Cell

The quality of a solar cell is determined by how efficiently it converts the incident photons to electric power. It is denoted by η , and known as the percentage of the highest power generated by the solar cell to the power injected (P_{in}) by the incident light. In experimental work, η is determined from the $J - V$ curves of a solar device. From the $J - V$ curves, the parameters that are used to determine η such as the fill factor (FF), J_{sc} , and V_{oc} can be extracted and used according to equation 3.4.

$$\eta = \frac{J_{sc}V_{oc}FF}{P_{in}} \quad 3.4$$

Figure 3.1 is an equivalent circuit model for analyzing the photovoltaic output of a solar device, it includes a diode, shunt resistance (R_{sh}), series resistance, and constant current source. The constant current source is indicated by J_{ph} , which is the photocurrent density produced by a solar cell under constant illumination. The diode signifies the recombination of the photogenerated charge carriers at a forward-bias voltage ($V + I.R_s$) (Boyd et al., 2011). R_{sh} is associated with resistance in the solar cell due to pinholes which create shunt pathways for generated carriers. Series resistance is associated with resistance due to the functional layers and the sheet resistance of the device front and rear contacts. According to Figure 3.1, the produced current density ($J(V)$) of a photovoltaic device is calculated as shown in equation 3.5.

$$J(V) = J_{ph} - J_0 \left[\exp\left(\frac{q(V+JR_s)}{nkT}\right) - 1 \right] - \frac{V+JR_s}{R_{sh}} \quad 3.5$$

Where the 2nd and 3rd term in the right-hand side of equation 3.0 represents current losses in the diode due to charge recombination, and due to shunt resistance, respectively. k , n , q , T , and J_0 are

Boltzmann constant, the ideality factor, elementary charge, absolute temperature (300 K), and the dark current of the diode, respectively.

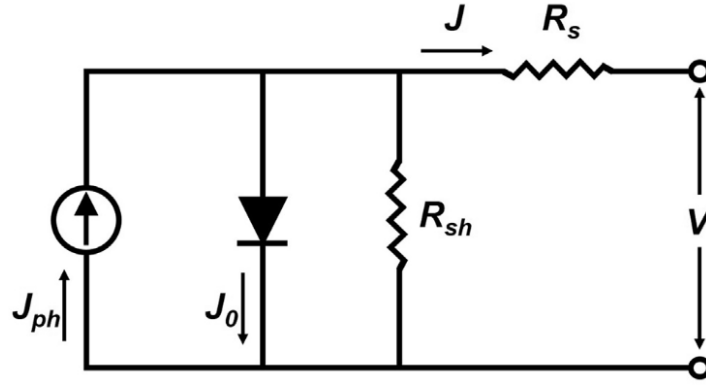


Figure 3.1. Equivalent circuit model for a solar cell (T. Wu *et al.*, 2021)

3.4 Open-Circuit Voltage (V_{oc}) of Sn-PSC

Sn-perovskites have comparable optoelectronic characteristics to its Pb counterpart. Surprisingly the PCE of Sn-PSCs is still inferior to that of Pb-PSCs. The primary drawback of Sn-PSCs is the low V_{oc} , the V_{oc} of most of Sn-PSCs ranges between 0.2 and 0.7 eV (Khan *et al.*, 2022; Moghe *et al.*, 2016; Rath *et al.*, 2019). The low V_{oc} is attributed to excess V_{oc} loss due to high charge carrier recombination within the perovskite film and the interlayers in the Sn-PSCs (X. Jiang *et al.*, 2020; T. Wang *et al.*, 2022). Therefore, it is important to appreciate the fundamentals of the V_{oc} loss of Sn-PSCs to explore ways of reducing the losses. Equation 3.5 can be organized to define the V_{oc} of a solar cell, the basic assumptions are; the value of R_{sh} is sufficient to inhibit the current passing through it to negligible values, and the diode is well designed. Using these assumptions, equation 3.5 can be simplified to equation 3.6.

$$V_{oc} = \frac{nkT}{q} \ln \left(\frac{J_{ph}}{J_0} + 1 \right) \quad 3.6$$

Where J_0 is calculated as shown in equation 3.7.

$$J_0 = q \left(\frac{D_n n_i^2}{L_n N_A} + \frac{D_p n_i^2}{L_p N_D} \right) \quad 3.7$$

Where D_n and D_p are electrons and holes carrier diffusion coefficient, correspondingly. N_A and N_D represent the doping densities of acceptors and donors, correspondingly. n_i is the dark carrier

density, and L_n and L_p represent the diffusion length of the minority carriers in n-type and p-type regions, respectively. L_n and L_p values can be calculated using equation 3.8 (Kamarudin *et al.*, 2019).

$$L = \sqrt{D\tau} \quad 3.8$$

Where τ is the symbol for carrier lifetime obtained from time-resolved photoluminescence (TRPL) measurement.

J_{ph} is the photocurrent density and is dependent on the conversion efficiency of the incident photons to electrons in a photovoltaic device. From equation 3.6, V_{oc} is directly and inversely proportional to J_{ph} and J_0 , respectively, implying that J_0 must operate at minimum values for high V_{oc} . J_0 originates from charge recombination in the perovskite film or the PSCs (J. Chen *et al.*, 2019). Charge recombination within the Sn-perovskite photoactive films results from excess defects due to Sn^{2+} oxidation, pinholes, and Sn-vacancies (Z. Zhu & Mi, 2022). While, the recombination at the interfaces results from defects at the boundaries of each layer or excess charge accumulation due to poor charge transfer at the layers' boundaries (X. Jiang *et al.*, 2020). This shows that V_{oc} losses primarily originate from the charge recombination at the defects within the absorber layer, and interfaces within the PSCs. Therefore, the charge recombination in perovskite devices has to be minimized to reduce V_{oc} losses if the efficiency has to pass the 14% mark so far achieved.

The charge diffusion length in equation 3.8 ($L = \sqrt{D\tau}$) can be directly estimated using photoluminescence (PL) data of an absorber material. The PL quenching technique can be employed to study the PL response of the perovskite material and the PL of the perovskite when it is deposited on an HTL or if an ETL is coated on it. The PL quenching helps in explaining how efficiently charges are extracted from the perovskite by either the ETL or HTL (X. Jiang *et al.*, 2020). Using the PL data and equation 3.9, the charge diffusion length can be estimated (P. Li *et al.*, 2020).

$$L \approx \frac{2d}{\pi} \sqrt{2 \left(\frac{\tau}{\tau_{quench}} - 1 \right)} \quad 3.9$$

Where τ_{quench} , τ , and d are the quenched carrier lifetimes, the charge carrier lifetime, and the photoactive film thickness.

Charge mobility in the PSCs is also crucial to the improvement in *the* V_{oc} of the devices (X. Jiang *et al.*, 2020). The carrier mobility of charges both holes and electrons, can be estimated using equation 3.8 and Einstein's relation in equation 3.10.

$$D = \frac{\mu kT}{q} \quad 3.10$$

Where μ is charge mobility and other parameters as defined before.

3.4.1 Open-Circuit Voltage (V_{oc}) Loss and Approaches used in Improving the V_{oc} in Sn-PSCs

The V_{oc} loss (V_{loss}) of solar cells is calculated using equation 3.11.

$$V_{loss} = \frac{E_g}{q} - V_{OC} \quad 3.11$$

Where E_g is the band gap of the absorber film, and q is the elementary charge in eV . According to Shockley-Queisser's (SQ) equilibrium, V_{loss} arises from radiation (ΔV_1), thermodynamic (ΔV_2), and non-radiative (ΔV_3) losses (Duan *et al.*, 2021). Therefore, equation 3.11 can be modified to equation 3.12 to contain all three the losses (X. Zhang *et al.*, 2022).

$$q\Delta V = (E_g - qV_{OC}^{SQ}) + (qV_{OC}^{SQ} - qV_{OC}^{rad}) + (qV_{OC}^{rad} - qV_{OC})$$

$$q\Delta V = q(\Delta V_1 + \Delta V_2 + \Delta V_3)$$

$$\Delta V = (\Delta V_1 + \Delta V_2 + \Delta V_3) \quad 3.12$$

Different research groups have tried ways of minimizing V_{oc} loss. Ning's group made the first effort to advance the V_{oc} of Sn-PSCs by manipulating the ETL in a p-i-n structured Sn-PSCs (X. Jiang *et al.*, 2020). The group used ICBA in place of the commonly used PCBM to fabricate devices with PEDOT:PSS/Perovskite/ICBA/BCP/Ag structure. The group achieved a V_{oc} of 0.94 V. ICBA has a shallower LUMO level as compared to PCBM; this implies that PCBM has a higher Fermi level and more states are electron occupied, the elevated electron concentration in PCBM can only be sustained by remote doping of iodine at the perovskite/ETL interface (Zheng *et al.*, 2023). The high electron state density can promote charge recombination at the ETL/perovskite interface and result in V_{oc} loss. On the hand, ICBA has a shallower LUMO level and thus forbids electron injection

from iodide, this helps in maintaining the perovskite stability and decreases charge buildup and recombination at the perovskite/ETL interface hence minimizing V_{oc} loss. From X. Jiang et al. (2020) work, it is important to comprehend the energy level of the perovskite before choosing an appropriate ETL layer with matching energy levels for achieving maximum V_{oc} .

A commonly used approach in improving the V_{oc} in Sn-PSCs is the enhancement of the Sn-perovskite film quality. Many researchers use different approaches to passivate the Sn-perovskite to eliminate deep and shallow defects responsible for the V_{oc} loss. T. Wang et al. (2022) achieved a V_{oc} of 1.01 V in a 2D/3D Sn-PSCs after eliminating the pinholes and forming a stratified heterojunction by treating the films by vacuum polling in the glove box antechamber before thermal annealing (T. Wang *et al.*, 2022). The stratified heterojunction junction formed enabled efficient charge separation and hence improved the V_{oc} . Jiang et al. (2022) eliminated defects by use of ethylenediammonium halide salts (EDA I_2 and EDABr $_2$) as defects passivating agents and achieved a V_{oc} of up to 0.82 V. Cao et al. (2022) used potassium thiocyanate (KSCN) interlayer as a base passivation approach to Sn-perovskite; KSCN performed the roles of aligning energy levels of the perovskite and the HTL, assisted in perovskite crystallization and promoted the charge transport (J. J. Cao *et al.*, 2022). The group achieved a V_{oc} of up to 0.84 V due to reduced charge recombination within the device. From the few noted works, it is important to limit defects responsible for charge recombination in Sn-PSCs for an improvement in their V_{oc} .

3.5 Photoluminescence (PL) and Time-Resolved Photoluminescence (TRPL) Spectroscopy

PL characterization is a contactless nondestructive technique for probing semiconductor materials in laboratories. It is widely used due to its simplicity and affordability of the instrumentation; the equipment is not sophisticated and hence needs little time in mastering its use. In PL spectroscopy, light is illuminated onto a material, where it is absorbed and an electron photoexcitation takes place due to the excess absorbed energy. The excited electron jumps from the VB (some authors prefer using HOMO (highest occupied molecular orbital)) to the CB (some authors prefer using LUMO (Lowest unoccupied molecular orbital)); the photoexcited electron relaxes within a given period to regain its equilibrium or ground state energy.

During the relaxation, the photoexcited electron returns to the VB and recombines with the created hole in a nonradiative or radiative process. In the radiative recombination, another photon is emitted

during the recombination, while no or very small intensity photons are emitted during the nonradiative recombination, the process is summarized in Figure 3.2. The emission of photons during electron relaxation is known as luminescence, hence the name photoluminescence because the process involves both photoexcitation and luminescence. The absorption and emission of a photon can result in phosphorescence and fluorescence processes where the latter is majorly applied in the characterization of biological samples and the former to characterize semiconductor materials. Fluorescence can be minimized in PL measurement by choosing an appropriate laser wavelength.

The intensity of the emitted light during PL processes can be analyzed spectrally to give useful characteristics of materials. PL is useful in probing both intrinsic and extrinsic properties of semiconductors (perovskites) such as (i) recombination process, (ii) materials quality, (iii) impurity and defect detection, (iv) band gap, and (v) semiconductor composition in case of mixed phases, (vi) surface and interface behaviour, and homogeneity mapping (Perkowitz, 1993). In semiconductors, PL happens as a result of electron transition between VB and CB, in which the energy difference is the band gap of the film. The radiative transition takes into account all the impurity and defect levels within the semiconductor; the presence of other unwanted levels in the semiconductor lowers the intensity of the radiated photon (Mahalingam, 2018). Thus, the purity and quality of a semiconductor can be determined from its PL spectrum.

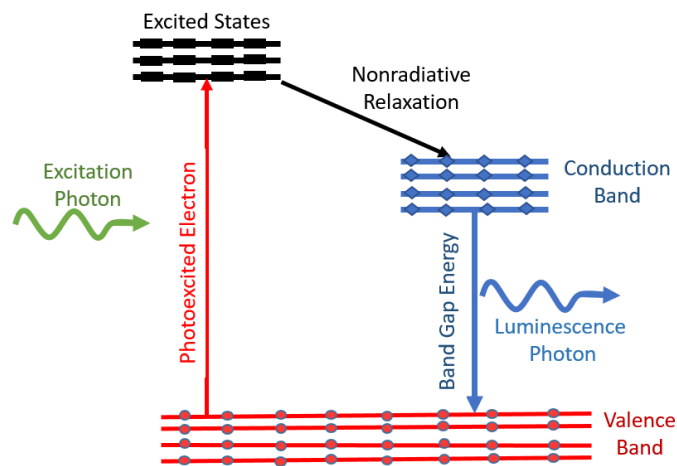


Figure 3.2. Basic principles of PL spectroscopy

TRPL is also a contactless probing technique used to evaluate the charge dynamics in semiconductors. In TRPL, a short laser pulse excites a material, and a fast detector is used to collect

and transmit the transmission of the material as a function of time. TRPL is used to understand charge recombination in semiconductors or at the interfaces of a solar cell. TRPL can also help in determining the quality of a semiconductor, high-quality materials tend to have longer emission time as compared to low-quality materials (M. Kim *et al.*, 2019; G. Liu *et al.*, 2020). However, in a solar cell, TRPL's shorter emission time between interfaces is considered best as it shows good charge extraction between the interfaces, probably because of low interfacial defects or proper band energy alignment at the interface. Table 3.1 gives a summary of how to interpret the TRPL data.

Table 3.1. Summary of TRPL data interpretation

Consideration	TRPL Emission Time	Film or Interface Quality
Absorber Film	Short	<ul style="list-style-type: none"> ❖ Poor film quality ❖ Existence of a large number of charge trap centers ❖ Fast charge recombination in the film
	Long	<ul style="list-style-type: none"> ❖ Good quality film ❖ Carrier recombination is slow and allows time for charge extraction ❖ Reduced defects in the film
ETL/Absorber interface or HTL/Absorber interface	Short	<ul style="list-style-type: none"> ❖ Faster charge extraction ❖ Suppressed charge recombination. ❖ Low defects at the interface ❖ Proper band alignment between the ETL or HTL and the absorber
	Long	<ul style="list-style-type: none"> ❖ Poor charge extraction ❖ A large number of defects at the interface ❖ Increased charge accumulation ❖ Poor band alignment between the HTL or ETL interface

3.6 Charge Recombination (monomolecular and bimolecular) in PSCs

The uncontrollable fast crystallization of Sn-perovskite is a recipe for nonhomogeneous Sn-perovskite film morphology. These films are marred with small grains, pinholes and many sharp irregular grain boundaries (Z. Lin *et al.*, 2021). The grain boundaries as observed earlier have a lot of structural defects (X. Jiang *et al.*, 2020), these defects act as charge trap centers within the absorber layer giving rise to what is known as non-radiative or monomolecular recombination (Z. Lin *et al.*, 2021). The rough morphology arising from fast crystallization also does not favour proper contact between the perovskite layer and other charge transport layers; leading to bimolecular recombination which occurs due to poor charge mobility across the solar cell layers, that is between the perovskite/ETL/contact or perovskite/HTL/contact.

The charge recombination types in PSCs can be evaluated by measuring the J_{sc} and V_{oc} of the cell measured under different light illumination intensities (T. Lee *et al.*, 2021). Equation 3.13 shows the relation of V_{oc} and J_{sc} of planar-inverted PSCs (Y. Liu *et al.*, 2020). From basic principles, $J_{sc} \propto I(\text{light intensity})$ and $J_{sc} \gg J_o$, (Z. Zhang *et al.*, 2022), which leads to the simplification of equation 3.13 to equation 3.14. By linearly fitting V_{oc} against light intensity a slope of $\frac{nk_B T}{q}$ can be determined to comprehend the charge recombination in solar cells during operation under light intensity (Yukta *et al.*, 2022). The ideality factor n for a solar cell with perfect crystallinity in the absorber layer and zero defects is always 1. Deviation of n values from 1 is a sign of nonradiative recombination, the bigger the deviation the larger the recombination. Nonradiative recombination results from deep defects in the absorber layer (Z. Xiao *et al.*, 2019), while radiative defects occur at the related solar cell interfaces (Y. Liu *et al.*, 2020).

$$V_{oc} = \frac{nk_B T}{q} \ln \left(\frac{J_{sc}}{J_o} + 1 \right) \quad 3.13$$

$$V_{oc} = \frac{nk_B T}{q} \ln I \quad 3.14$$

Where k_B is the Boltzmann constant, n is the diode ideality factor, J_o is the saturation current density in the dark, T is the absolute temperature (300 K), and q is the basic charge.

In addition, by using the Shockley diode equation 3.15, the presence of bimolecular recombination in a solar cell can be determined. Equation 3.15 can be modified to equation 3.16 (Z. Zhang *et al.*, 2022), which makes it easier to determine the value of n directly from the slope of the graph of

$\ln J_{SC}$ against \ln of light intensity, to avoid symbol confusion between radiative and nonradiative recombination, most books and research articles use α instead of n .

$$J = J_0 \left[\exp \left(\frac{qV}{nk_B T} \right) - 1 \right] \quad 3.15$$

$$n = \left(\frac{kT \partial \ln J}{q \partial V} \right)^{-1} \quad 3.16$$

3.7 Charge Trap Density Concentration in Sn-Perovskite Layers

The defect/trap density concentration in perovskites can be evaluated by constructing electron-only and hole-only devices (Jahandar *et al.*, 2019; Ryu *et al.*, 2023). In electron-only devices, the devices are constructed with perovskite layer inserted between 2 electron transport layers, for example, ITO/ETL/perovskite/PCBM/Au (Y. Li *et al.*, 2023). In hole-only devices, the perovskite absorber film is positioned between two p-type semiconductor layers such as ITO/PEDOT:PSS/perovskite/P3HT/Au (Ryu *et al.*, 2023). In summary, the perovskite is sandwiched between two materials of same type of charge transport, which are aligned to either its conduction band or valence band, in a manner that either electrons or holes can be injected (Le Corre *et al.*, 2021). The devices are characterized under dark conditions to obtain their current density-voltage ($J - V$) curves (B. Li *et al.*, 2023; F. Wang *et al.*, 2020). A plot of $\log J$ versus $\log V$ (example shown in Figure 3.3) is used to determine the charge trap density.

$\log J$ versus $\log V$ has three regions. The first region at low bias voltage shows a linear $J - V$ correlation known as the Ohmic region. During SCLC measurement, charge carriers are injected to a semiconductor through the contacts. At low voltages (low electric field), the injected carriers are less than the intrinsic carriers; and since the injected carriers are few, they end up trapped in the semiconductor and dislodge some of the intrinsic carriers to the materials conduction band and finally the charges are collected; the charge transport is smooth and fast and can be described as linear. This implies that the generated current increases linearly as voltage, $J \propto V$.

After the ohmic region, the curve experiences a kink and starts to increase non-linearly and exponentially. As the voltage or electric field rises, the Fermi level of the materials move near the conduction band or towards the valence band for n-type and p-type semiconductors (Jain *et al.*, 2007). In the process, the charge traps, which were above the Fermi level, are filled up and more electrons are free to jump to the conduction band (Jain *et al.*, 2007). The current density therefore

risers rapidly due to increased charge carriers in the trap-filled region (G. Liu *et al.*, 2020). The traps are filled at a voltage known as trap-filled voltage, V_{TFL} , and is estimated by intersecting the linear part of the second portion of SCLC graph and the Ohmic part through extrapolation, the meeting point of the two lines is the V_{TFL} . The trap concentration of the perovskite layer can be estimated by employing trap-filled voltage and equation 3.17 (Ryu *et al.*, 2023).

$$N_{defects} = \frac{2\epsilon\epsilon_0 V_{TFL}}{qL^2} \quad 3.17$$

With the parameter defined as: defect density is $N_{defects}$, the permittivity of free space is ϵ_0 , the relative dielectric constant of the absorber material is ϵ , the basic charge is q , the thickness of the absorber layer is L and V_{TFL} is the trap filling limited voltage (Yukta *et al.*, 2022).

The third region is identified as the space charge limited current (SCLC) region or Child's region or Mott-Gurney drift regime. In this section, all the traps are occupied then charge mobility is governed by the injected carries. The identification of the trap-filled and Child's region can be done by considering the log-log gradient ($g(V)$) of the curve after the kink; the region where the gradient of the nonlinear part of the graph is greater than 3 ($g(V) > 3$) is the trap-filled region and the region where ($g(V) \approx 2$) is the SCLC region.

The SCLC region is important in determining the charge mobility of the absorber layer using the Mott-Gurney law, equation 3.18 (J. J. Cao *et al.*, 2022).

$$\mu = \frac{8JL^3}{9V^2\epsilon_r\epsilon_0} \quad 3.18$$

Where μ is charge mobility, J/V^2 is the $g(V)$ in the SCLC region and the rest of the other variables are as defined in equation 3.17.

The principle is important in comparing the defect concentration in perovskite absorber layers made by incorporating different precursor contents or by comparing trap densities of perovskites deposited on different substrates (J. J. Cao *et al.*, 2022; H. Jiang *et al.*, 2018).

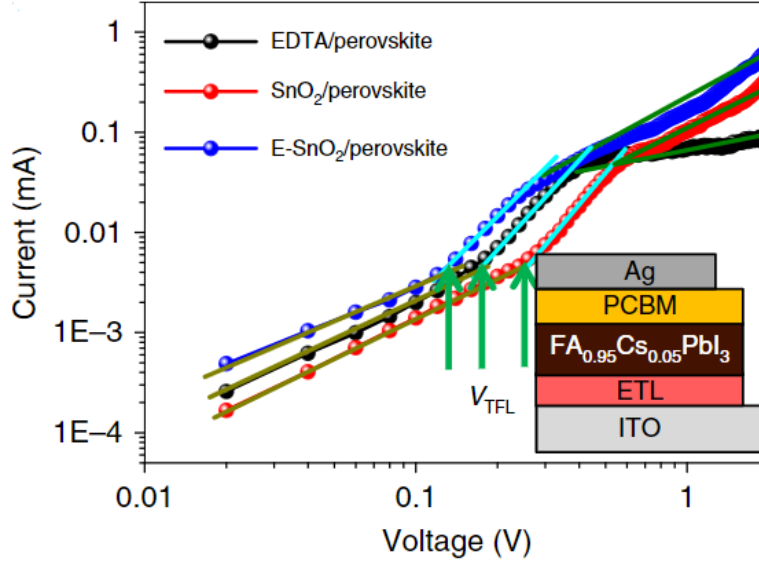


Figure 3.3. Electron-only device (D. Yang *et al.*, 2018)

3.8 Mott-Schottky (M-S) Analysis

M-S measurement analysis of PSCs is a powerful way of deeply understanding why solar cells have different power conversion efficiencies. The M-S can give information on the flat-band potential, which is known as built-in potential (V_{bi}), and the defects concentration (N_D) of PSCs (Sivula, 2021). In PSCs especially Sn-PSCs, the estimated defects concentration is mostly treated as the density of defects within the perovskite absorber material since most defects originate from the absorber material (Almora *et al.*, 2016; C. Wang *et al.*, 2020).

The first step in M-S measurement is conducting electrochemical impedance spectroscopy (EIS) measurement of the respective device over a range of potentials. During EIS measurement, an alternating current (AC) potential small perturbation at a given frequency (angular) is applied to a device and the device AC response is recorded. The impedance is gotten from the real and imaginary parts of the obtained EIS spectrum of the AC response. The EIS is measured at different frequencies and the M-S plot is chosen from a given frequency since the capacitance of devices depends on frequency.

In the M-S plot, the V_{bi} is directly read from the intercept of the graph and the x-axis, the meeting point is arrived at after linearly extrapolating the M-S curve to the x-axis. N_D is approximated from the slope of the linear part by employing equation 3.19 (Ma *et al.*, 2014).

$$\frac{1}{C^2} = \frac{2}{\epsilon\epsilon_0qA^2N_D} \left(V - V_{bi} - \frac{k_B T}{q} \right) \quad 3.19$$

Where C is the space-charge capacitance in Farads, V is applied voltage, A is the device active area in cm^2 , ϵ is the relative permittivity of the perovskite, ϵ_0 is the vacuum permittivity ($8.85 \times 10^{-14} F cm^{-1}$), q is the elementary charge ($1.60 \times 10^{-19} C$) and the rest of the parameters are as defined earlier. The value of $k_B T/q$ if calculated comes to 0.02, which is negligible as compared to other parameters and therefore can be ignored, the equation therefore can be written as equation 3.20:

$$\frac{1}{C^2} = \frac{2}{\epsilon\epsilon_0qA^2N_D} (V - V_{bi}) \quad 3.20$$

Using Figure 3.4, which is an M-S plot of a Sn-PSC, equation 3.20 can be rewritten as equation 21.

$$\frac{C^{-2}}{(V-V_{bi})} = \frac{2}{\epsilon\epsilon_0qA^2N_D} \quad 3.21$$

Where $\frac{C^{-2}}{(V-V_{bi})}$ is the slope of the linear part of the graph. Therefore N_D is as in equation 3.22

$$N_D = \frac{2}{\epsilon\epsilon_0A^2e(slope)} \quad 3.22$$

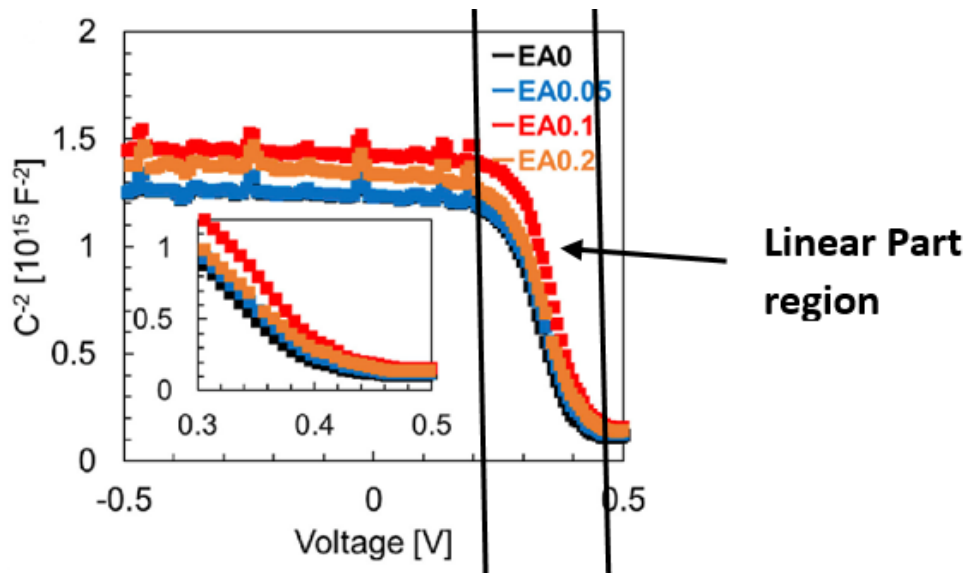


Figure 3.4. An example of an M-S plot (Nishimura *et al.*, 2020)

3.9 Principles of Fourier Transform Infrared Spectrometer (FTIR)

Spectroscopy

Infrared (IR) spectroscopy studies the interaction between matter and infrared radiation. Most materials have dipole moments and active in the IR region (Lopes *et al.*, 2018). Incident IR passes through a material; the material absorbs the radiation leading to excitation, which is manifested in form of vibration of the molecular bonds. The molecular bond vibrations take place at specific wavenumbers in the IR region for different samples, and occur in the form of stretching, rocking, twisting, bending, out-of-plane deformation and wagging. The peaks of the wavenumbers of the absorbed IR are dependent on the physicochemical properties of a molecule. After absorption, part of the remaining IR is transmitted through the material. The peaks are interpreted as the characteristic fingerprint of the functional group present within that corresponding material.

Infrared spectroscopy forms the backbone to Fourier transform infrared spectrometer (FTIR). FTIR spectroscopy is preferred over other dispersive spectrometers because of its accuracy, ease of handling, better sensitivity, precision and accuracy (Xiang, 2018). Figure 3.5 shows a block diagram of working principal of FTIR, adapted from (Undavalli *et al.*, 2021). FTIR has an IR source, which passes through an interferometer, the interferometer measures the energy of IR reaching the sample. The radiation from the interferometer is either transmitted through the sample or bounces from the sample surface, the sample absorbs a specific wavelength of the incident IR. The light from the material then passes through a detector and to a processing computer for transformation of energy signals to Fourier signals.

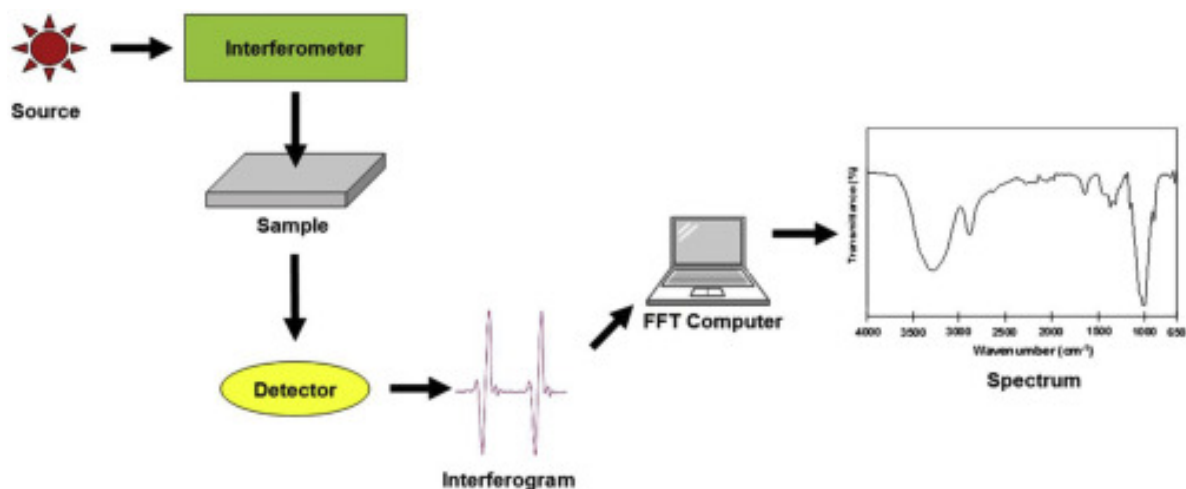


Figure 3.5: Block diagram of working principal of FTIR spectroscopy (Undavalli *et al.*, 2021).

3.10 Use of PDINN as a Buffer Layer and Cu as an electrode in Sn-PSCs

The primary challenges of Sn-PSCs remain instability and low power conversion efficiencies (Y. Chen *et al.*, 2022; T. Wang *et al.*, 2022). Copper (Cu) electrode is used instead of the commonly used silver (Ag) or gold (Au) electrodes. Cu can effectively be used as an alternative electrode due to its comparable physiochemical properties as Ag and Au and it is less costly as compared to the commonly used electrodes. The conductivity of Cu, which is $5.96 \times 10^7 \text{ Sm}^{-1}$ is comparable to that of Ag ($6.30 \times 10^7 \text{ Sm}^{-1}$) and Au ($4.10 \times 10^7 \text{ Sm}^{-1}$) at 20 °C (Z. Xu *et al.*, 2022). Cu also shows a similar work function ($\sim 4.7 \text{ eV}$) as Ag and Au with function values of $\sim 4.6 \text{ eV}$ and $\sim 5.1 \text{ eV}$, respectively.

Cu is attractive to the fabrication of stable Sn-PSCs due to its stability. Cu has excellent corrosive resistance to ambient moisture and excess halides from perovskites absorber materials. PSCs suffer ion migration when photoexcited or when exposed to high temperatures (Su *et al.*, 2022; Zheng *et al.*, 2023). The ion migration involves the movement of iodine (I⁻) ions from the lattice of the perovskite into other layers of the PSCs during the device degradation. The diffusion of I⁻ can lead to interaction between the counter electrode and the halide. It has been shown that for Ag electrode Ag-I interaction leads to creation of an insulating AgI compound which inhibits charge transport and charge collection in PSCs (Teymourinia *et al.*, 2021). The interaction between Ag and the migrating I⁻ makes it difficult to fabricate long-term stable and high-performing devices. Au, which is considered stable as compared to Ag, has also been shown to react with halide ions in humid conditions (Z. Xu *et al.*, 2022). Cu on the other hand has shown stability toward corrosion with I⁻ making it possible to build long-term stable devices (Wijesekara *et al.*, 2021). In addition, the reaction between Cu and I⁻ in case it happens, results in a semiconductor that has minimal impedance to charge transfer in the devices (Wijesekara *et al.*, 2021). Thus, using copper cathode can prolong the lifetime of Sn-PSCs.

The function of the buffer layer is to provide ohmic contact between the ETL and the cathode (Shi & Jayatissa, 2018; W. F. Yang *et al.*, 2020). BCP has the challenge of thickness control in fabricating devices, it lowers the *FF* and PCE of devices if extremely thin or thick (C. Chen *et al.*, 2017). The optimized thickness of BCP is $\sim 8 \text{ nm}$ (C. Chen *et al.*, 2017), which may be difficult to control using solution-based processing techniques. Thick BCP reduces its conductivity, which is

manifested in reduced J_{SC} and FF of devices fabricated by other research groups, due to increased charge accumulation at the cathode/BCP interface (Asgary *et al.*, 2021).

CHAPTER FOUR

MATERIALS AND METHODS

4.1 Fabrication and Characterization of $\text{FA}_{0.50}\text{MA}_{0.45}\text{PEA}_{0.05}\text{SnI}_{3.00}$ and FASnI_3 Solar Cells

4.1.1 Materials

The materials that were used include; indium-tin-oxide (ITO) coated glasses, *N,N*-Dimethylmethanamide (DMF) (99.8%), chlorobenzene (CB) (99.8%), phenethyl ammonium iodide (PEAI) (>98%), [6,6]-phenyl-C60-butyric acid methyl ester (PC₆₀BM), anilinium hypophosphite (AHP) (97%), dimethyl sulfoxide (DMSO) (99.8%), tin (ii) iodide (SnI_2) (99.999%), formamidinium iodide (FAI) (>98%), tin fluoride (SnF_2) (>99%), bathocuproine (BCP) (99.99%), methylammonium iodide (MAI) (99%), were acquired from Sigma Aldrich. PEDOT:PSS water dispersion (AI 4083) was procured from Ossila. The materials were deemed pure and hence no further purification was performed during the usage of the materials.

4.1.2 Substrate Cleaning

The substrates used were indium-tin-oxide (ITO) coated glasses. During the cleaning process; the substrates were soaked in water containing 2% Hellmex detergent for 12 hours, then scrubbed using cotton buds under running deionized water to remove all the dirt residue on the ITO surfaces. The samples were then sequentially ultrasonicated in distilled water, acetone, and ethanol for 900 seconds each; acetone and ethanol were used to eliminate all organic impurities on the substrate. The clean substrates were then blow-dried by employing a nitrogen gas gun to ensure uniform drying without solvent stains, and then treated by a UV-ozone cleaning machine before use.

UV-ozone cleaning is important in removing any residual organic contaminants after ultrasonication of the substrates in the various organic solvents. UV-ozone cleaning is a non-mechanical process that does not require specialized conditions, as long as the machine is available. Figure 4.1 is a block diagram of a UV-Ozone machine. The basic operation principle is summarized in Figure 4.2; it involves ozone generation, ozonolysis, and decomposition of organic matter. The mercury lamp generates UV light with wavelengths of 184.9 and 253.7 nm (S. Wang, 2014). The 184.9 nm wavelength UV breaks down the oxygen molecules within the chamber to generate

ozone, O_3 . The 253.7 nm wavelength UV interacts with the ozone and decomposes it to produce high-energy oxygen, the ozonolysis process.

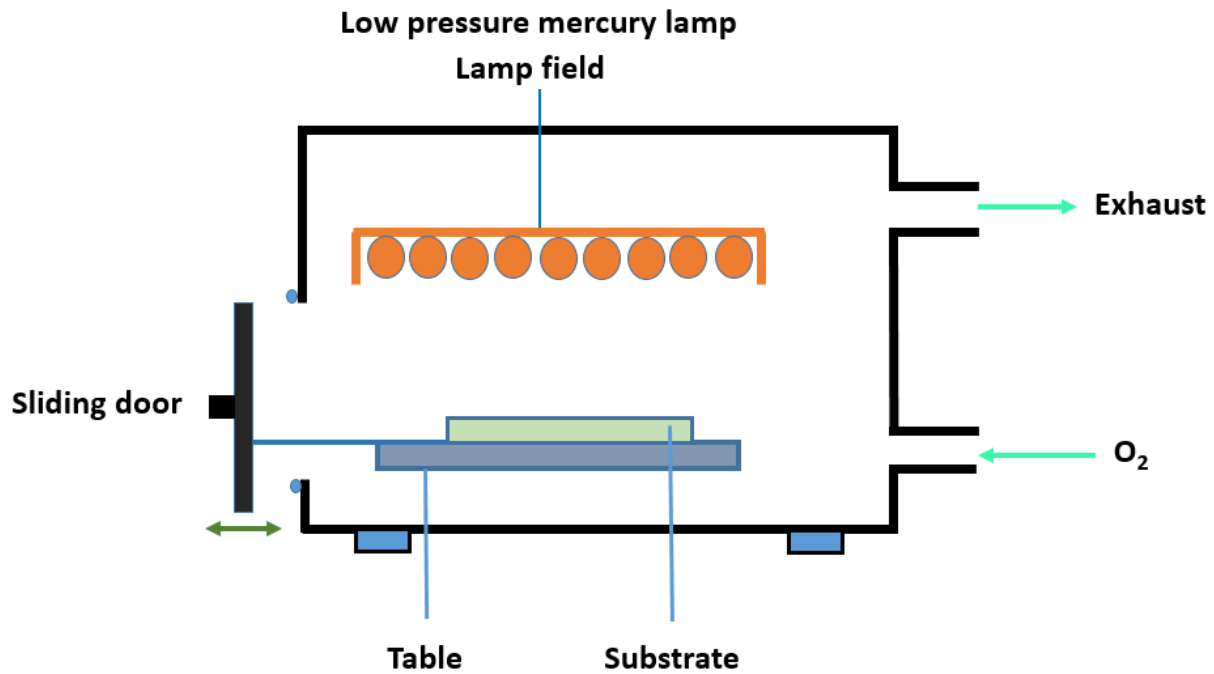


Figure 4.1. The block diagram of the UV-ozone cleaner machine

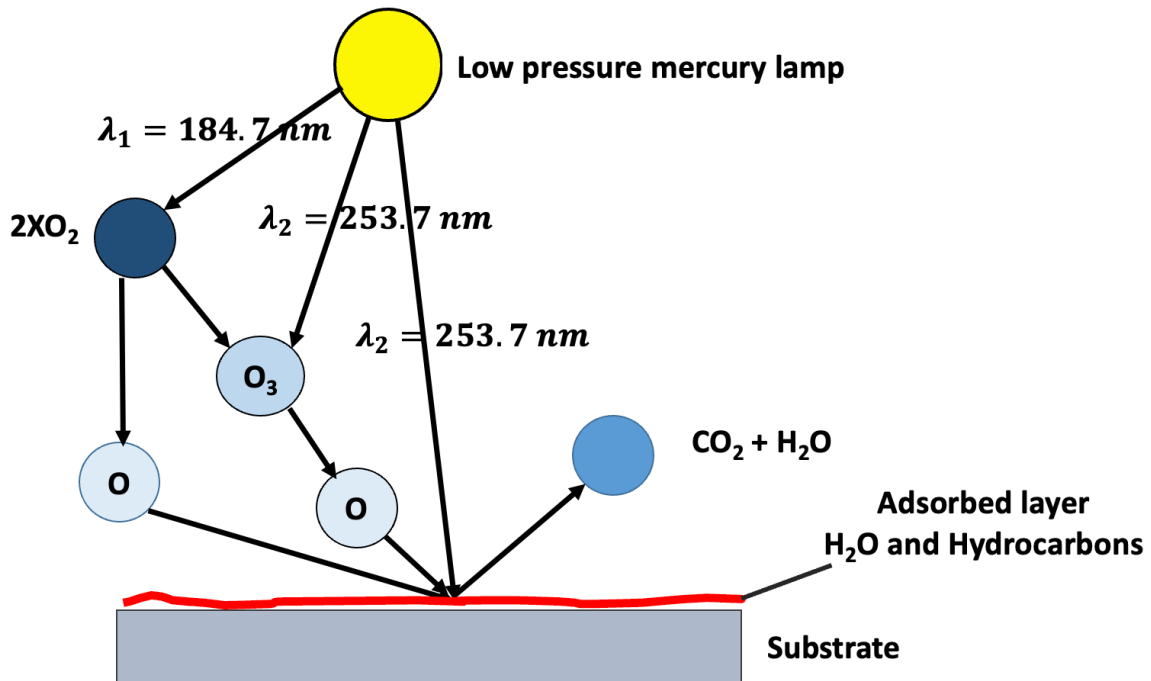


Figure 4.2. The mechanism of UV-ozone cleaning (S. Wang, 2014)

The 253.7 nm wavelength also decomposes the residual organic contaminants on the substrate; the decomposed contaminants then react with the high-energy oxygen to form volatile molecules such as CO₂ and H₂O; the volatile materials can then evaporate and escape the chamber through the exhaust hence leaving the substrates surfaces ultraclean. The UV-ozone treatment is also beneficial for surface treatment of the ITO substrates, for ease of deposition of polar and nonpolar solutions (Weber *et al.*, 2023). The treatment enhances the surface energy of the substrates through the formation of hydroxyl functional groups; the 253.7 nm wavelength can break water molecules within the chamber to produce OH and O free radicals. The OH radicle if adsorbed on the substrate surface, can lead to the creation of a functional group, which has high bonding energy, this process increases the surface energy of substrates. The increased surface energy improves the wettability of the substrates hence the ease of depositing a layer on the substrate.

4.1.3 Solution Preparation

PEDOT:PSS solution was used as purchased from the manufacturer.

4.1.3.1 Perovskite Solution

Solvent engineering involving the mixing of DMSO and DMF at a ratio of 100:400 was used. DMSO is important in Sn-perovskite film formation as it retards the crystallization of the perovskite layer by forming SnI₂.3DMSO intermediate adduct before the complete crystallization of the perovskite film (Ke *et al.*, 2019). The intermediate phase helps in the development of homogeneous layers with good spread on the substrate (Igbari *et al.*, 2019). However, DMSO has a higher viscosity and is not easy to spin, hence the need to dilute it using DMF.

1 M perovskite precursor solution was made by dissolving SnI₂, MAI, FAI, PEAI, and SnF₂ in the ratio of 1.00:0.45:0.50:0.05:0.10. AHP as a co-additive was added into the solution at varied amounts between 0.00 and 0.10 M. Sn-perovskite is very unstable and thus SnF₂ was used as an antioxidant (Kayesh *et al.*, 2018). The AHP was added to act as Sn²⁺ oxidation inhibitor and to eliminate the detrimental effects of excess SnF₂ as is discussed in Chapter 5 in this study.

4.1.3.2 PCBM and BCP solutions

20 mg of PCBM was diluted in 1 mL of CB; this is a predetermined concentration by other research groups and commonly used within the perovskite community (X. Jiang *et al.*, 2020; Z. Yang *et al.*,

2019; S. J. Yang *et al.*, 2021). 0.5 mg of BCP was dissolved in 1 mL ethanol. All the solutions were left to dissolve overnight without stirring.

4.1.4 Sn-PSCs Fabrication

The solar cells were fabricated on pre-cleaned ITO-glass substrates. All the solutions were filtered through a 0.45 μm polytetrafluoroethylene membrane (PTFE) before use. 30 μL of PEDOT:PSS was spin-coated on the ITO substrate at 5000 rpm for 30 s and thermally treated in air at 150 $^{\circ}\text{C}$ for 1200 seconds. The PEDOT:PSS layers were allowed to cool to room temperature and shifted to a nitrogen-filled glovebox for subsequent layers depositions.

The absorber layer was deposited on PEDOT:PSS by spin coating of 20 μL of the filtered perovskite solution at 5000 rpm for 40 s in two steps; the substrate was allowed to spin for 10 s at 1000 rpm in the first step, and 5000 rpm in the remaining 30 s. At the 25th s of the spin coating, 150 μL of CB was dropped gradually on the spinning substrate to splash away the excess solvent from the film; the process is as shown in Figure 4.3. The layer was then thermally treated inside the glovebox at 70 $^{\circ}\text{C}$ for 1800 seconds. The film with perovskite deposit was left to cool before 20 μL of PCBM was deposited on it at 2000 rpm for 30 s. The PCBM layer was then annealed at 100 $^{\circ}\text{C}$ for 600 seconds. 75 μL BCP was immediately spin-coated on PCBM after cooling and then annealed at 80 $^{\circ}\text{C}$. The device was finalized by evaporating 70 nm thick silver on the BCP at $\sim 10^{-7}$ Torr vacuum level to create an active area of 0.0725 cm^2 .

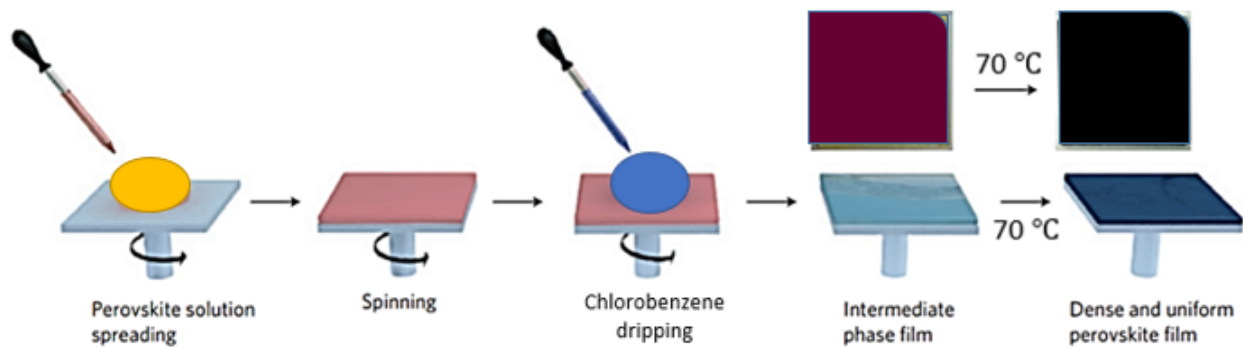


Figure 4.3. The two-step deposition procedure of the perovskite solution (Adapted from Jeon *et al.* (2014) and modified)

4.1.5 Films and Devices Characterization

This section of the study was aimed at refining the characteristics of Sn-perovskite absorber layer, and therefore all the film characterization was only done for the perovskite film. A good absorber material in a solar device should have a high absorption coefficient and absorb light in a broad range of the solar spectrum (T. Wu *et al.*, 2021). The fitness of Sn-perovskite to absorb an adequate amount of light was studied using PerkinElmer Lambda 900 UV-vis spectrophotometer (Shimadzu UV-2006). The absorbance was measured in the transmission mode, where the light was allowed to pass through the film, and the film faced the light source during measurements.

The charge dynamics and defects within the perovskite were studied by measuring the photoluminescence (PL) and time-resolved-photoluminescence (TRPL) by using Edinburgh Instruments Spectrometer (FLS1000). The PL and TRPL measurements were done using a 450 nm excitation laser with a 4.2 mW excitation intensity on a $2.5 \times 2 \text{ mm}^2$ area at 45° degrees laser inclination, in the transmission mode; transmission mode in PL is when the laser is directed from the glass substrate into the material, that is the film faces the same direction as the incident light. The TRPL decay data were fitted using a bi-exponential decay formula (the fitting was done directly during measurements); and the average decay time was determined using equation 4.1 (Nishimura *et al.* 2020).

$$\tau_{avg} = \frac{\tau_1 B_1 + \tau_2 B_2}{B_1 + B_2} \quad 4.1$$

Where τ_1 and τ_2 are the lifetimes of the 1st and 2nd components of the exponential fitting function, B_1 and B_2 are the amplitude of the 1st and 2nd components in the fitting range channel.

The crystallinity and structural effects of the additives on the perovskite structure were studied using X-ray diffractometer (XRD) measurements. The XRD pattern were measured by utilizing a PANalytical X'Pert Pro X-ray diffractometer with $\text{CuK}\alpha$ radiation at 40 kV and 40 mA. The X-ray was produced on a copper target at a wavelength of 1.54 angstrom.

A good absorber material must have good morphology for proper contact between the ETL and the absorber material to reduce chances of charge recombination; to determine this; a scanning electron microscope (SEM) measurement was utilized. The morphology of the film was measured by employing SEM (SEM, LEO 1550) with a resolution of between 1 - 5 nm.

In this study, two additives were used to deter the facile oxidation of Sn-perovskite. This necessitated the use of an instrument that can determine the interactions of the additives within the perovskite material. The measurement was achieved by using Fourier-transform infrared (FTIR) using a PIKE MIRacleVertex 70 spectrometer (Bruker) with a DLATGS detector at room temperature.

Lastly, the stability and performance of the devices were determined using their current density (J) versus voltage (V) curves. The $J - V$ curves were obtained from a 2400 series source meter (Keithley) with an air mass (AM) of 1.5 solar simulators.

4.2 Fabrication and Characterization of FA_{0.70}EA_{0.15}PEA_{0.15}SnI_{2.70}Br_{0.30} Solar Cells

4.2.1 Materials

BCP (Angene), poly(3-hexylthiophene-2,5-diyl) (P3HT) (Rieke metals), PC₆₁BM (Brilliant Matters), ethylenediammonium diiodide (EDAI₂ –Great cell solar), PEDOT:PSS (Clevios AI4083 Heraeus) and Trifluoroethanol perylene-diimide (PDINN). The rest of the chemicals were procured from Sigma Aldrich. Ethyl ether, Iodine ($\geq 99.8\%$), phenethylammonium iodide (PEAI), tin fluoride (SnF₂), tin powder ($< 45 \mu\text{m}$ particle size, 99.8% trace metals basis), tin powder ($< 150 \text{ nm}$ particle size $\geq 99\%$ trace metals basis), potassium thiocyanate (KSCN), tin powder ($< 45 \mu\text{m}$ particle size, 99.8% trace metals basis), asparagine (Asp), formamidinium iodide (FAI), pyrazine (PZ), ethylammonium iodide (EAI), chlorobenzene (CB), phenethylammonium iodide (PEAI), formamidinium bromide (FABr), DMF, Isopropyl alcohol (IPA), DMSO and anhydrous ethanol. Copper beads (Cu) and Tin-doped indium oxide (ITO) glass.

4.2.2 Synthesis of tin iodide (SnI₂)

The purity of SnI₂ is a major challenge in fabricating high-performing Sn-PSCs. Most of the SnI₂ used including the purest (99.999%) contain trace amounts of Sn⁴⁺; the presence of Sn⁴⁺ in SnI₂ lowers the performance of Sn-PSCs by forming charge nonradiative recombination centers within the absorber layer (Fu *et al.*, 2018; Hoefler *et al.*, 2017; Y. Li *et al.*, 2022). In this section, SnI₂ was synthesized using a one-step synthesis method according to Ning's group (2021) (X. Jiang *et al.*, 2021). The synthesis process was conducted in the glovebox to avoid chances of oxidation.

329.9 mg of iodine was dispersed in 810 μL of DMSO and stirred at 1500 rpm at 25 °C for 2 hours. The solution was then diluted with 490 μL DMF and stirred at 1500 rpm for 20 minutes. 1200 μL of the I_2 solution was taken and used to dissolve 118.7 mg of tin powder ($< 150 \text{ nm}$ particle size $\geq 99\%$ trace metals basis); the solution was stirred at 1500 rpm for 2 hours at room temperature to form SnI_2 solution. The solution was left to settle before further use.

4.2.3 Recrystallization of FAI, EAI, FABr and PEAI

FAI, EAI, FABr and PEAI were purified to eliminate impurities that can inhibit the PCE of solar cells. The purification was done through recrystallization of the materials. Supersaturated solutions of the materials were formed by dissolving excess of the materials in anhydrous ethanol; the solution was stirred until all the solute was dissolved. Steadily and sideways, ethyl ether (an antisolvent) was added to the solution to initiate the recrystallization process. The solutions containing the antisolvent were then stored in the fridge for 72 hours. The solution was filtered using a vacuum filtration process, during filtration; excess ethyl ether was used to wash the formed crystallites. The materials were then transited into a vacuum oven and dried at 45 °C for 24 hours. The ready materials were packed and kept back in a nitrogen-filled glove box to avoid air oxidation or contamination.

4.2.4 Solution Preparations

(2-10 mg) Potassium thiocyanate (KSCN) was diluted in 1 mL DMF and IPA to form the interlayer solution.

The synthesized SnI_2 solution which contained solvents (DMSO:DMF) in the ratio 5:3 was used in preparing tin perovskite solution. 1000 μL of the SnI_2 solution was added to FAI:FABr:PEAI:EAI: SnF_2 :Sn-powder ($< 45 \mu\text{m}$):PZ:Asp:EDAI₂ at a weight (in mg) ratio of 74.0:37.5:37.4:26.0:15.7:11.9:4.0:2.6:1.1. The solution was kept in the glovebox for 2 hours under stirring at 1100 rpm at 60 °C for 2 hours. During use, the perovskite solution was filtered through a 0.2 μm PTFE filter (Whatman) and kept stirring at 700 rpm on a 60 °C hot-plate during use.

A mixture of PCBM:P3HT (20:1 w/w mg) was diluted in 1 mL CB and kept stirring for 3 hours at 350 rpm at 60 °C. 1 mg of PDINN and BCP was dissolved in 1 mL and 2 mL anhydrous ethanol, respectively.

4.2.5 Device Fabrication

The solar cells were constructed on precleaned ITO substrates. The cleaning process involved ultrasonication of the substrates in deionized water mixed with detergent, deionized H₂O, acetone, and IPA for 25 minutes each, sequentially. The cleaned samples were dehydrated in a vacuum oven overnight and left to cool. The cool substrates were subjected to a UV-ozone cleaner for 20 minutes, then removed from the machine to cool. PEDOT:PSS was filtered through a 0.45 μm cellulose acetate membrane filter (Advantec) and then spin-coated on the ITO substrates at 5000 rpm for 30 s. PEDOT:PSS substrates were thermally treated at 150 °C for 20 minutes then left to cool and immediately transferred to the glove box for the deposition of the perovskite and other charge transport layers. The perovskite film was deposited in two steps from the filtered precursor solution, in the first step, the spin speed was 500 rpm for 5 s and in the subsequent step the spinning rate was 5000 rpm for 40 s. Chlorobenzene (CB) was gradually dropped on the spinning substrate between the 20th and 30th during the subsequent step. The perovskite was then annealed at 80 °C for 10 minutes. The perovskite was left to cool in the perovskite loading chamber at a vacuum level of -2 Torr for 30 minutes.

PCBM solution after filtration using a 0.2 μm polytetrafluoroethylene (PTFE) filter was spin-coated on the perovskite at 2000 rpm for half-a-minute and then annealed at 80 °C. PCBM films were again left to cool in the glove box loading chamber for 30 minutes. BCP or PDINN solutions were spin-coated on PCBM at 6000 rpm for 30 s and annealed at 80 °C in the glove box. The deposited layers were left in the glove box loading chamber overnight. The devices were finalized by thermally evaporating 100 nm copper as the cathode on them using an evaporator at a range of $\sim 10^{-6} - 10^{-7}$ Torr vacuum level, resulting in devices of 0.12 cm² active areas.

PDINN was chosen based on its outstanding electrical and physical properties. Firstly, the electron mobility of PDINN is high due to its $\pi - \pi^*$ backbone stacking (Valero *et al.*, 2020). Secondly, PDINN has an appropriate dipole moment to decrease the work function of the cathode to equal the energy levels of the ETL (Yao *et al.*, 2020). Thirdly, the secondary amine in the PDINN chain can form hydrogen bonding with the ETL to enhance the ohmic contact between the ETL and the counter electrode. Lastly, PDINN has excellent oxidative and thermal stability making it easy to improve the stability of Sn-PSCs. Therefore, using PDINN as Cu interfacial layer can help in fabricating high-performing and stable Sn-PSCs.

4.2.6 Characterization of Films and Devices

The optical properties of some of the deposited films (pristine and treated PEDOT:PSS, and perovskite) were obtained from the Shimadzu UV-2550 spectrophotometer (UV-3600I Plus –UV-Vis-NIR spectrophotometer).

The photovoltaic properties of the made devices were determined from Polaronix K201 Solar Simulator LAB50, McScience, under 1 sun illumination (100 mWcm^{-2} AM 1.5G). The solar simulator was calibrated using a Si-reference cell (RSCiG5, PVM977) certified by PV Measurements Inc., USA. The $J - V$ measurements from the simulator at intervals of time were used to study the PCE performance stability of the finished devices. The charge recombination mechanism of the devices was also studied using the solar simulator, by measuring the $J - V$ characteristic of the devices at different light intensities. The light intensity was varied by using neutral optical glasses with different light transparency between 91.6 and 3.2 %. Deeper charge recombination studies in the devices were studied using electrochemical impedance spectroscopy (EIS), using a computerized potentiostat (IVIUMSTAT Tech). The EIS measurement was done between 1 MHz and 500 Hz frequency range in dark conditions. The measurement was done at a bias voltage of 0.6 V (unless stated otherwise in the results section) with 10 mA sinusoidal ac perturbation. The EIS data were fitted using ABC EISanalyzer (Bondarenko & Ragoisha, 2005) to determine the series and recombination of the devices. The EIS instrument was also employed to understand the capacitance-voltage properties of the devices at a potential range of -0.2 to 0.7 V, to determine the defect density and the in-built potential (V_{bi}) of the devices. The transient photocurrent (TPC) and transient photovoltaic (TPV) were measured using all-in-one characterization system (PAIOS, Fluxim AG, Switzerland) to additionally comprehend charge transfer and recombination in the solar cells.

CHAPTER FIVE

RESULTS AND DISCUSSION

5.1 FA_{0.50}MA_{0.45}PEA_{0.05}SnI_{3.00} films and solar cells

In this section, the morphological and optoelectronic properties of FA_{0.50}MA_{0.45}PEA_{0.05}SnI_{3.00} layers are discussed. Also, the photovoltaic properties and stability of Sn-PSCs based on FA_{0.50}MA_{0.45}PEA_{0.05}SnI_{3.00} absorber layer is discussed.

5.1.1 Morphology of the Perovskite Layer

The morphology of the deposited absorber layer was determined from the SEM imaging as exhibited in Figure 5.1. Sn-perovskites facially degrade as a result of fast oxidation of Sn²⁺. Researchers have always opted for the use of antioxidants or oxidation inhibitors to facilitate the stability of Sn-perovskites. The utilization of SnF₂ as an additive to inhibit the facial oxidation of tin-perovskite is a common practice in the tin-perovskite field among different researchers (Li *et al.*, 2019). However, excess of SnF₂ is detrimental to the devices as it results in phase segregation in the perovskite films, the unwanted phases act as charge trap centers and thus lowers the performance of devices made from such films (Zhao *et al.*, 2020). Most researchers are opting for the co-additive approach to mitigate the phase segregation caused by SnF₂ (Tai *et al.*, 2019), in this study AHP has been employed as a supplement additive.

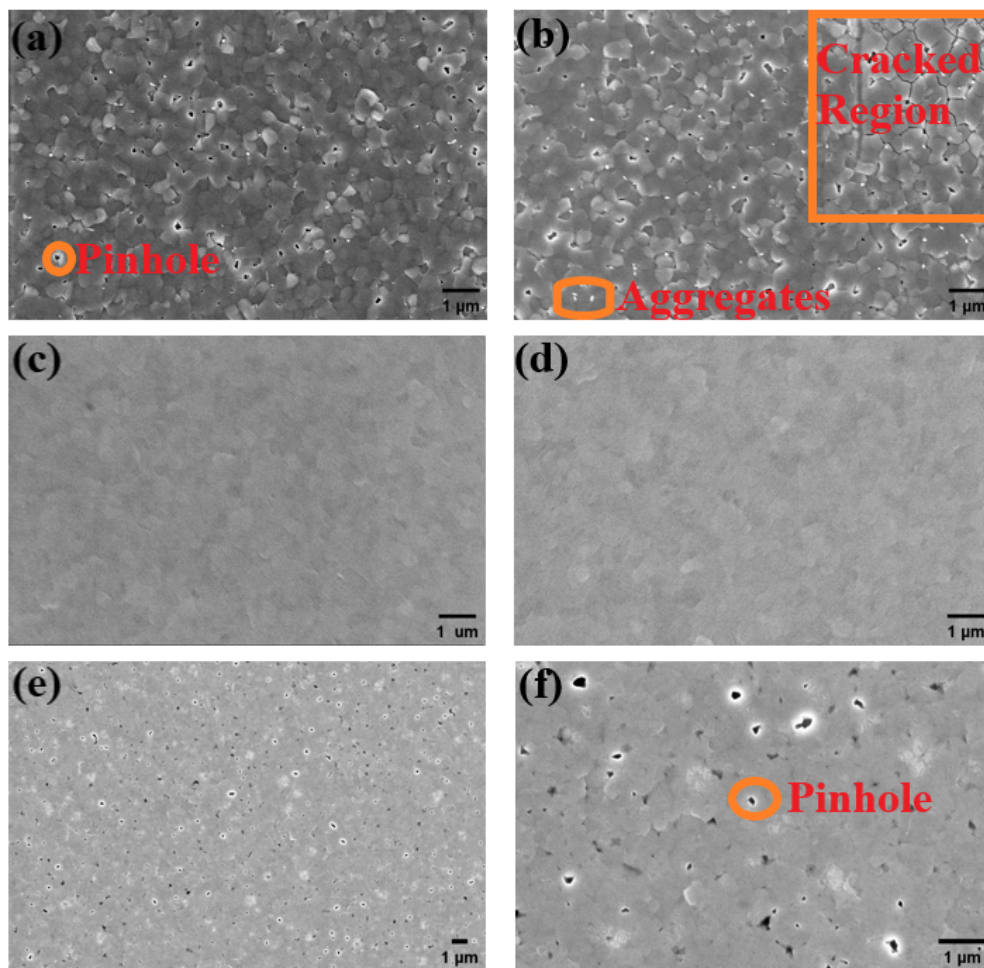


Figure 5.1. Scanning electron microscope images of $\text{FA}_{0.50}\text{MA}_{0.45}\text{PEA}_{0.05}\text{SnI}_{3.00}$ films having 0 (%) (a) and (b), 5% (c) and (d), and 10% (e) and (f) AHP under different magnifications.

In Figure 5.1 (a and b), the films containing SnF_2 exhibited non-uniform morphology and several pinholes. In addition, the films were unstable as shown in Figure 5.1(b), the cracked region shows that the films degraded upon exposure to the SEM electron beam. The pinholes, non-uniformity, and un-stability of films are not desirable for the development of stable and high-performing devices as they only result in charge trap centers. Figure 5.1 (c, d, e, and f) shows the morphology of the films prepared by incorporating AHP as a supplement additive to SnF_2 in the perovskite precursor solution; the films look dense and uniform. It was discovered that 5% AHP is beneficial to the film as it results in compact films without any pinholes, (as displayed in Figure 1(c and d)), also the surface of the films is ‘looking smooth’, which can enhance the contact at the perovskite/electron transport layer interface to enhance the charge transfer across the device (Zhou

et al., 2022). However, excess of the AHP led to a dense film with many pinholes, as shown in Figure 5.1(e and f), thus not suitable for photovoltaic applications. Pinholes in perovskite devices imply poor absorber layer substrate coverage, which can lead to many charge trap centers and hence lower device performance because of the low shunt resistance (Lee *et al.*, 2019). Therefore, it is better to maintain the co-additive at a low quantity for improvement in film quality and device performance.

5.1.2 Fourier Transform Infrared Spectroscopy Measurement and Reaction Mechanism

After observing aggregates due to SnF₂ disappear upon the addition of AHP, it was hypothesized that there must be a reaction between AHP and SnF₂ resulting in the aggregates and pinholes annihilation. The interaction may have led to the formation of a complex salt accountable for the passivation of the film's grain boundaries and pinholes. The passivated films exhibited no grain boundaries, showing that the formed complex deposited itself around the perovskite grains and on the surface of the film. The creation of the complex salt was investigated by utilizing Fourier transform infrared spectroscopy as shown in Figure 5.2.

AHP is a phosphite complex possessing a P=O double bond, the stretching vibration band region of P=O is placed in the region between 1320 and 1140 cm⁻¹ in the FTIR measurement spectrum (Açikel *et al.*, 2018). Figure 5.2(a) displays the characteristic bond stretch of P=O at 1146 cm⁻¹ when the FTIR measurement was run on a pure AHP film deposited on a glass slide. When a mixed precursor solution of AHP and SnF₂ was deposited on the glass substrate, the FTIR bond stretch shifted from the initially observed 1146 cm⁻¹ to 1111 cm⁻¹ as shown in Figure 5.2 (a), the red curve. The peak shift towards the lower frequency region is due to SnF₂ interacting strongly with AHP, which confirms the initial speculation. SnF₂ interaction with AHP could have resulted in the creation of a complex salt, with a chemical formula such as Sn(H₂PO₂)₂.SnF₂, the complex salt is responsible for the observed surface and grain boundaries passivation.

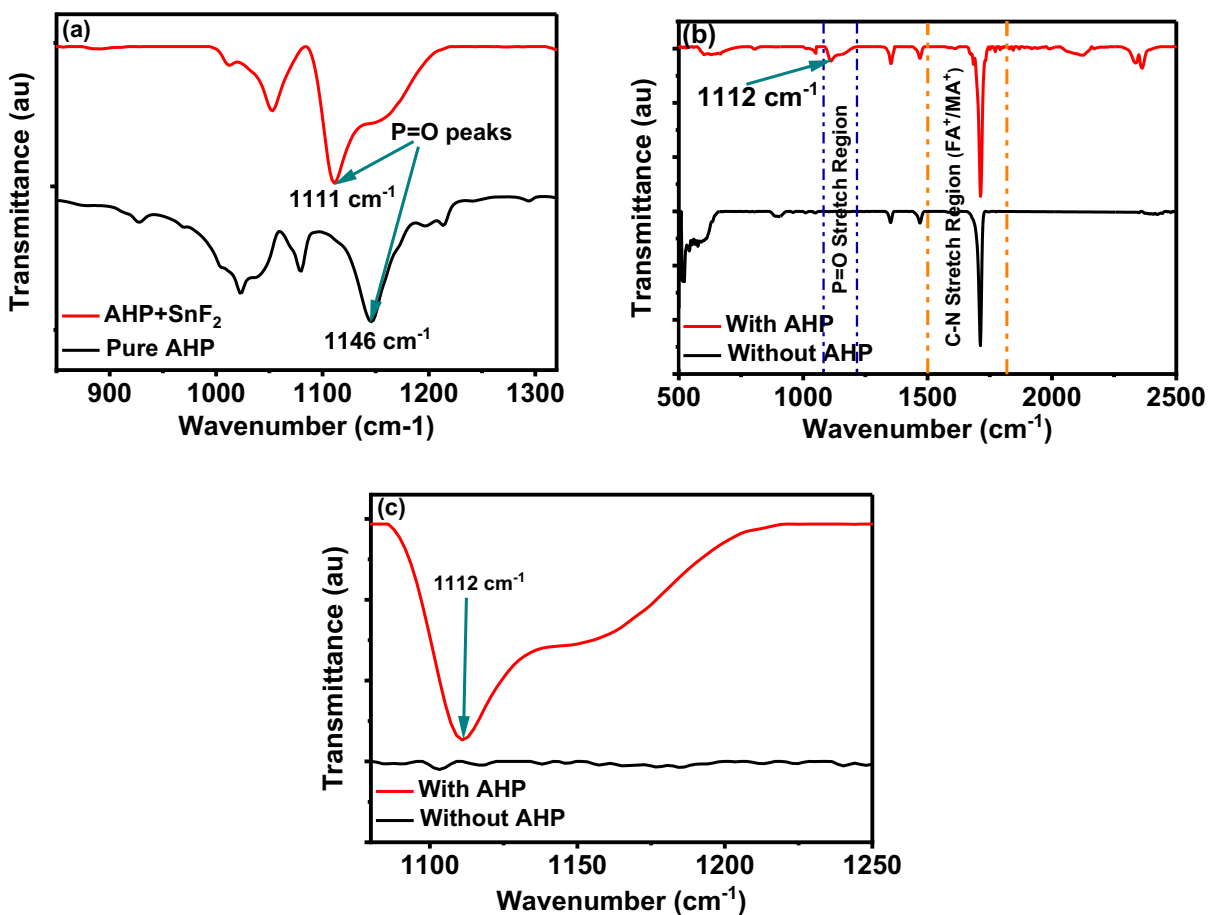


Figure 5.2. The FTIR spectra of (a) AHP, and a mixture of AHP and SnF₂ (b) tin-perovskite film with and without AHP as a co-additive, and (c) the extract of the region between 1086 and 1250 cm⁻¹ of (b) for easy visibility.

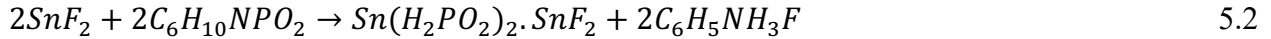
FTIR measurement was conducted on the Sn-perovskite film to determine the presence of the proposed complex salt in the deposited perovskite as exhibited in Figure 5.2(b). From Figure 5.2(b), the perovskite deposited from a precursor solution comprising of AHP showed a typical bond stretch of P=O at ~1112 cm⁻¹, while the film deprived of AHP had no peak in the region between 1320 and 1140 cm⁻¹. This is an evidence that AHP is still contained in the film even after annealing which is beneficial to the film's stability and uniformity. Figure 5.2(c) was extracted to help in showing clearly that the peak at 1112 cm⁻¹ is only present in the film containing the AHP additive.

A chemical equation of the possible reaction was suggested to help in understanding the reaction between AHP and SnF₂. C₆H₅NH₃H₂PO₂ is the empirical formula of AHP, the compound contains

H₂PO₂⁻ anion, which can reduce Sn⁴⁺ to Sn²⁺ due to its reducing ability according to the suggested equation 5.1, proposed earlier by another research group (Wang *et al.*, 2018).



However, from the FTIR data, there is also a reaction between SnF₂ and AHP resulting in a complex salt. The equation of reaction is suggested as shown in equation 5.2:



From equations 5.1 and 5.2, it is noted that there are byproducts such as PH₄⁺ and C₆H₅NH₃F, which are formed because of AHP interaction with SnF₂ and Sn²⁺ in the perovskite film. These byproducts are thought to have decomposed and are released into the glovebox environment during the film annealing process. The two equations also show that AHP is a multifunctional additive with the ability to inhibit phase separation resulting from excess SnF₂ and to decrease the oxidation of Sn²⁺ in the Sn-perovskite. The complex salt formed is important as it helps in the smoothening away of the defects in the perovskite films.

5.1.3 X-Ray Diffraction Measurement Results

The structural stability and crystallinity of the films with and without AHP were investigated using the XRD measurements as shown in Figure 5.3. The stability test was carried out in the open air, with a hotness range of 15 – 25 °C and relative humidity of between 20-30%. The FA_{0.50}MA_{0.45}PEA_{0.05}SnI_{3.00}-perovskite film contained mixed organic cation, MA⁺ and FA⁺, and a bulky ammonium cation, PEA⁺; such a recipe is important for the stability and crystallinity of the perovskite film. The bulky ammonium cations are hydrophobic in nature and can passivate the perovskite film to prevent it from degradation and improve its stability (Shao *et al.*, 2018; Z. Xiao *et al.*, 2019). In addition, the bulky ammonium cation has been shown to enhance perovskite crystallinity and thus helps in improving the open circuit voltage of the perovskites (X. Jiang *et al.*, 2020).

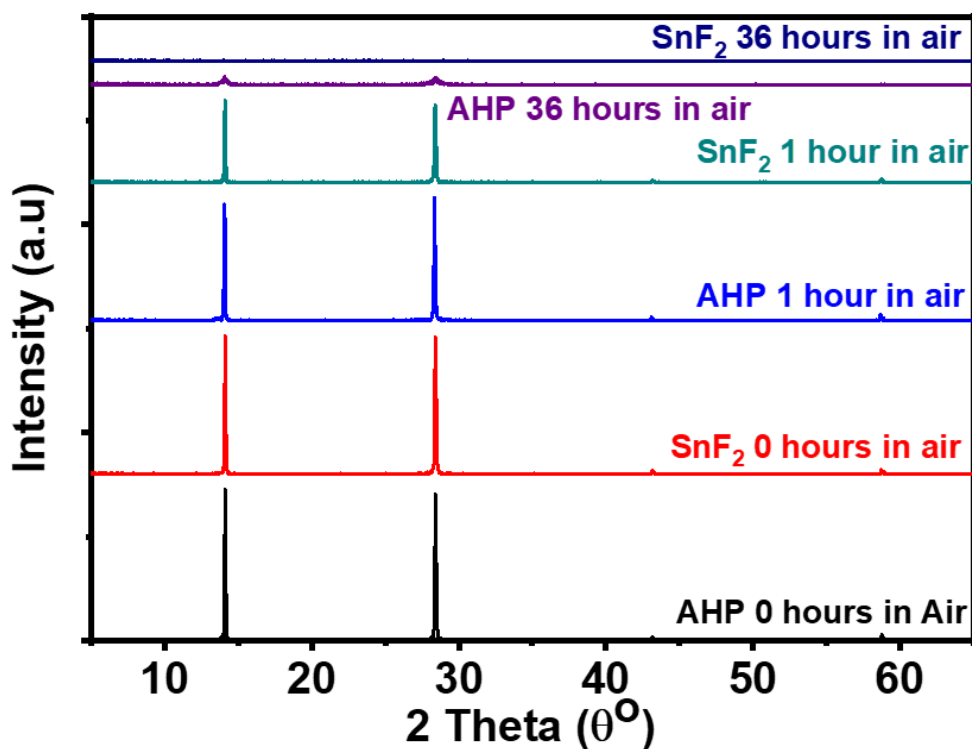


Figure 5.3. The XRD peaks of FA_{0.50}MA_{0.45}PEA_{0.05}SnI_{3.00} upon exposure to air at varied time intervals

From Figure 5.3, the XRD peaks of both the control and AHP-modified layers exhibited spikes at 14.1° and 28.5° falling on the (100) and (200) planes, correspondingly. The XRD-patterns of the perovskite show two distinctive diffraction patterns at (100) and (200) which are well enhanced in both cases showing a preferred crystal orientation; the orientation could have been enhanced by the presence of PEA⁺ cation as noted earlier (X. Jiang *et al.*, 2020). The peak intensity slightly increased in the films with AHP, showing a more enhanced orientation and improved crystallinity. The crystallinity was verified using the full width at half maximum (FWHM) values of the 14.1° peak as shown in Figure 5.4. FWHM values of the film containing AHP was 0.076°, which is smaller than 0.091° for the pristine film. The smaller FWHM shows improved crystallinity and suggests a growth in the grain sizes of the films (Y. Jiang *et al.*, 2022). Improved crystallinity is important in films intended for photovoltaic applications as it shows reduced defects and hence fewer charge trap centers (Z. Xing *et al.*, 2023).

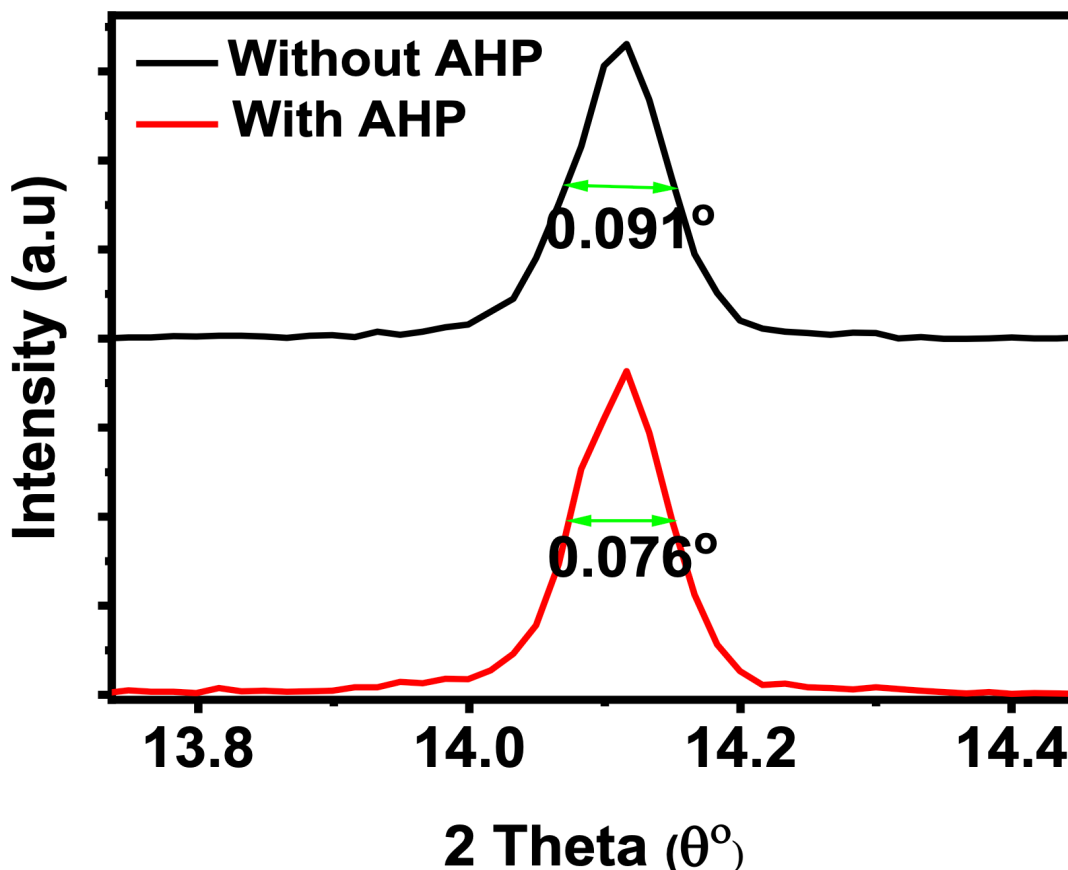


Figure 5.4. The FWHM of the perovskite layer with and without AHP at zero hours exposure to normal atmospheric conditions.

As presented in Figure 5.5, the decomposition rate of the film in ambient conditions was studied using the XRD measurement data in Figure 5.3. The decay pattern of the (100) peak for the film with and without AHP was extracted and plotted as shown in Figure 5.5. In the first 3 hours, the XRD peak intensity of the films reduced considerably, but the most affected film was the film without AHP as it lost almost half of its original peak intensity. The perovskite layers were continuously exposed to air and the XRD peak of the film without AHP completely diminished while the AHP film retained at least 5% of its original intensity. This test together with the SEM images additionally confirm that AHP improved the stability of the Sn-perovskite layer. The enhanced stability is credited to the capability of AHP to hinder the oxidation of Sn^{2+} in air and its ability to interact with SnF_2 to passivate the perovskite film.

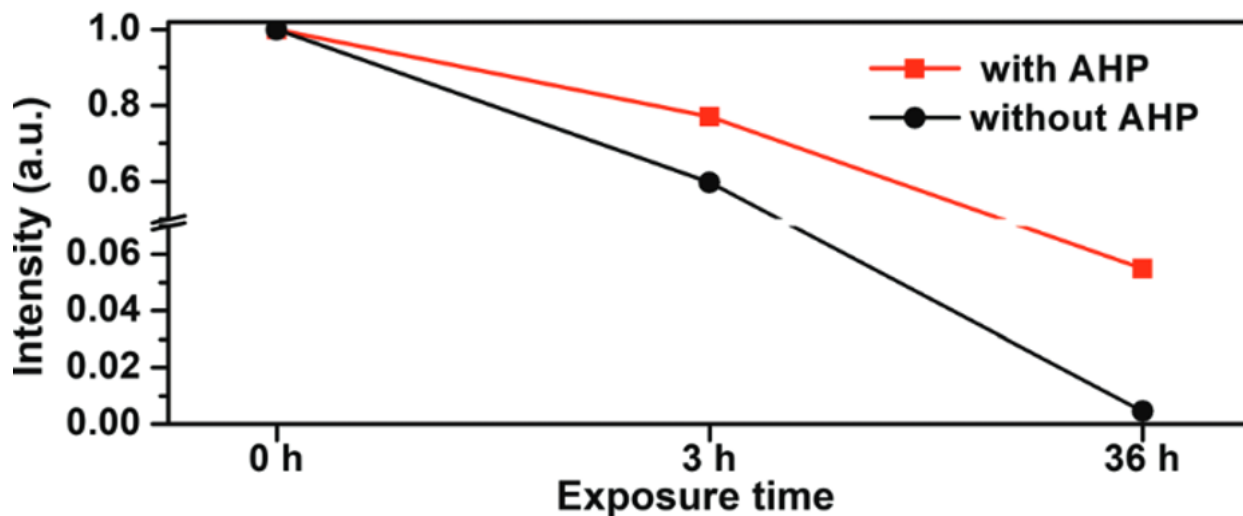


Figure 5.5. The rate of peak intensity decay time for films with and without AHP.

5.1.4 Absorption Spectra of $\text{FA}_{0.50}\text{MA}_{0.45}\text{PEA}_{0.05}\text{SnI}_{3.00}$

The effect of AHP on the perovskite film optical absorbance was investigated using the absorbance spectra data as presented in Figure 5.6. The UV-vis spectra of the control and AHP-based film were obtained to understand the changes occurring in the light absorption capability and the band gap of the layers upon the addition of AHP. The AHP film showed better absorbance likened to the pristine film, which further proves that AHP can better the PCE of tin-PSCs. In addition, the absorbance data shows improved characteristic of Sn-perovskite films upon the insertion of AHP as established by the SEM and XRD data. The absorption onset of the pristine and film with AHP are 928 nm and 933 nm, respectively, equivalent to a band gap of 1.33 eV and 1.31 eV, correspondingly. The band gap is within the range of band gaps obtained for Sn-perovskite layers in previous studies (Igbari *et al.*, 2019; Ke *et al.*, 2019) The slight suppression in the band gap of the perovskite after adding AHP could be because of the AHP-SnF₂ complex salt passivating the perovskite surface; according to the XRD data, the AHP did not alter the perovskite structure and thus the variation in the band gap cannot be credited to the AHP in the bulk perovskite.

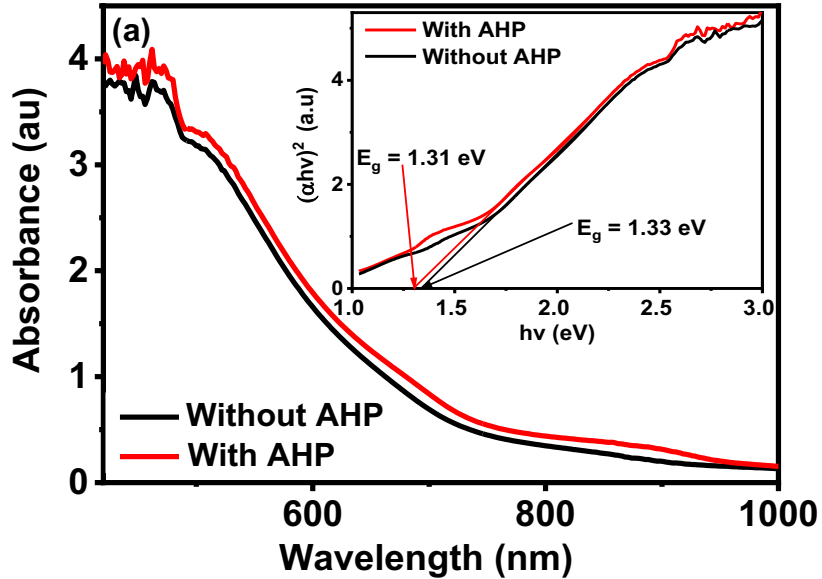


Figure 5.6. Absorption spectra of Sn-perovskite films containing and without 5% AHP; the inset shows the band gaps of the films with and without AHP.

5.1.5 Photoluminescence and Time-resolved photoluminescence measurement

The charge carrier dynamics of the pristine and AHP-based films were studied using the PL and TRPL spectroscopy as shown in Figure 5.7. In addition, the PL spectra were used to verify the optical absorbance onset and band gap of the absorber materials. From Figure 5.7(a), the pristine and film with AHP have PL peaks at 928 nm and 933 nm, which corresponds perfectly to the absorbance onset under the UV-vis measurements. The slight red shift of the peaks could be a result of improved crystallinity as observed under the XRD results, and enhanced quality of the absorber material upon the addition of AHP (J. Cao *et al.*, 2019). The PL intensity of AHP-based films was enhanced as likened to the films with only SnF₂ additives. The increased PL intensity is a suggestion of reduced nonradiative charge carrier recombination in the perovskite material (C. Wang *et al.*, 2021).

Defects within the perovskite layer always act as charge recombination sites leading to reduced PL intensity. As shown in the SEM images under morphology study, SnF₂ though best as an antioxidant in tin perovskites, leads to films with separated phases and pinholes. The phase segregation and pinholes in the absorber material act as charge recombination centers leading to non-radiative charge recombination hence the reduced PL peak intensity. Upon the addition of

AHP, the PL intensity is intensified because AHP annihilated the phase aggregates caused by SnF₂. In addition, AHP as co-additive assisted in passivating the surface of the perovskite layer leading to reduced deep imperfections within the film; most deep defects originate from the surface of the film (Li *et al.*, 2021). Thus, it can be established that improving the properties of Sn-perovskite film can improve its charge dynamics by reducing charge recombination.

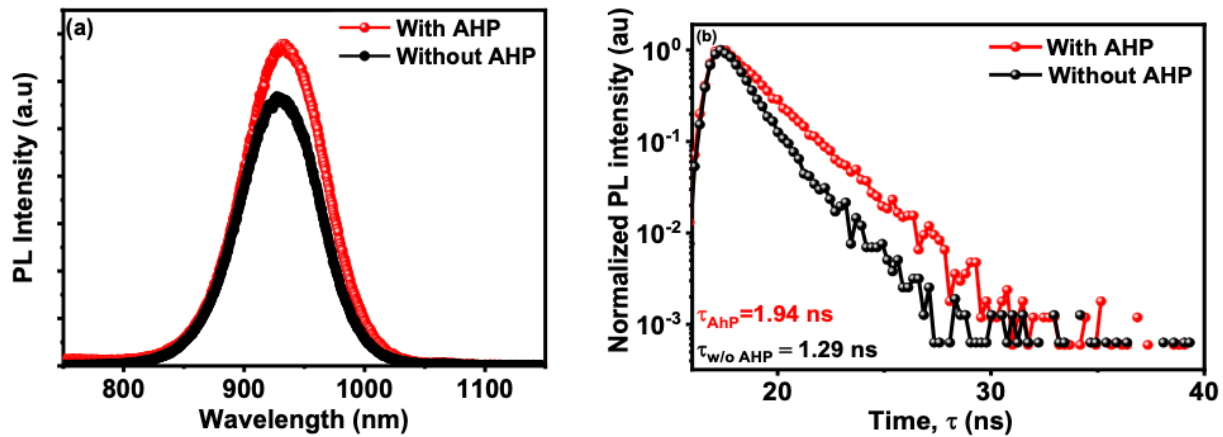


Figure 5.7. (a) PL spectra of FA_{0.50}MA_{0.45}PEA_{0.05}SnI_{3.00} with and without AHP additive, (b) TRPL spectra of FA_{0.50}MA_{0.45}PEA_{0.05}SnI_{3.00} having and without AHP.

TRPL spectra shown in Figure 5.7(b) were also obtained to ascertain the passivation property of AHP as a co-additive. The charge carrier lifetime of the AHP-based film is 1.94 ns which is higher than 1.29 ns for the film with SnF₂ only as the additive. The improved carrier lifetime is an indication of improved film quality as observed under the SEM, XRD, and UV-vis measurements. The short carrier lifetime exhibited by the films with SnF₂ only is a result of numerous charge recombination centers resulting from pinholes and phase segregation caused by SnF₂ in the absorber layer (M. Kim *et al.*, 2019; G. Liu *et al.*, 2020). The carrier lifetime is increased with the addition of AHP because it helps in eliminating most of the carrier recombination centers. Increased carrier lifetime decay can help in improving the PCE of Sn-PSCs since most of the charges can be collected by the ETL and HTL.

5.1.6 Photovoltaic Properties of the FA_{0.50}MA_{0.45}PEA_{0.05}SnI_{3.00} Solar cells

Based on the characteristics of control and AHP-based Sn-perovskite layers, inverted Sn-PSCs having a structure ITO/PEDOT:PSS/ FA_{0.50}MA_{0.45}PEA_{0.05}SnI_{3.00} (with only SnF₂ additive, and with

a mixture of SnF₂ and 5% AHP additives)/PC₆₀BM/BCP/Ag were fabricated. The active area of the devices during the $J - V$ measurement was 0.0725 cm². Table 5.1 shows the maximum PCEs and average photovoltaic performances of 10 reference devices and 33 devices fabricated from the addition of AHP into the absorber layer. The PCE of the reference solar cells was low, with the best device having a PCE of 4.74 % under the forward direction scan with a J_{SC} of 25.38 mA cm⁻², open circuit voltage (V_{OC}) of 0.44 V and a fill factor (FF) of 43.08%. The average performance of 10 reference devices was $4.05 \pm 0.59\%$. The PCE of the devices impressively improved upon the incorporation of 5% AHP into the absorber layer. The champion devices exhibited a PCE of 6.87%, FF of 57.16%, V_{OC} of 0.48 V, and J_{SC} of 25.21 mA cm⁻² in the forward scan direction. The average performance of 5% AHP-based devices was $5.21 \pm 0.63\%$, which is higher compared to the reference devices in Table 1. Figure 5.8 shows a display of the $J - V$ curves of the champion reference device and device with 5% AHP additive. The $J - V$ curves show both the forward and reverse scan direction for ease of estimation of the hysteresis occurring in the devices. The arrow pointing from the photocurrent density to the open circuit voltage indicates the forward scan direction, while the arrow pointing from the open circuit voltage to the photocurrent density indicates the reverse scan.

Table 5.1. Summary of the photovoltaic characteristics of the devices fabricated using FA_{0.50}MA_{0.45}PEA_{0.05}SnI_{3.00} perovskite absorber layer

Sample	V_{oc} (V)		J_{sc} (mA cm ⁻²)		FF (%)		PCE (%)	
	Forward	Backward	Forward	Backward	Forward	Backward	Forward	Backward
Without AHP (Champion)	0.44	0.42	25.38	25.26	43.08	41.18	4.74	4.42
Without AHP (Average)	0.43 ± 0.01	0.36 ± 0.10	18.14 ± 5.07	18.30 ± 5.00	53.87 ± 8.81	47.67 ± 8.97	4.05 ± 0.59	3.19 ± 1.28
With AHP (Champion)	0.48	0.47	25.21	25.38	57.16	55.98	6.87	6.65
With AHP (Average)	0.47 ± 0.02	0.45 ± 0.02	19.80 ± 3.97	19.74 ± 3.99	57.36 ± 7.29	54.70 ± 6.75	5.21 ± 0.63	4.77 ± 0.71

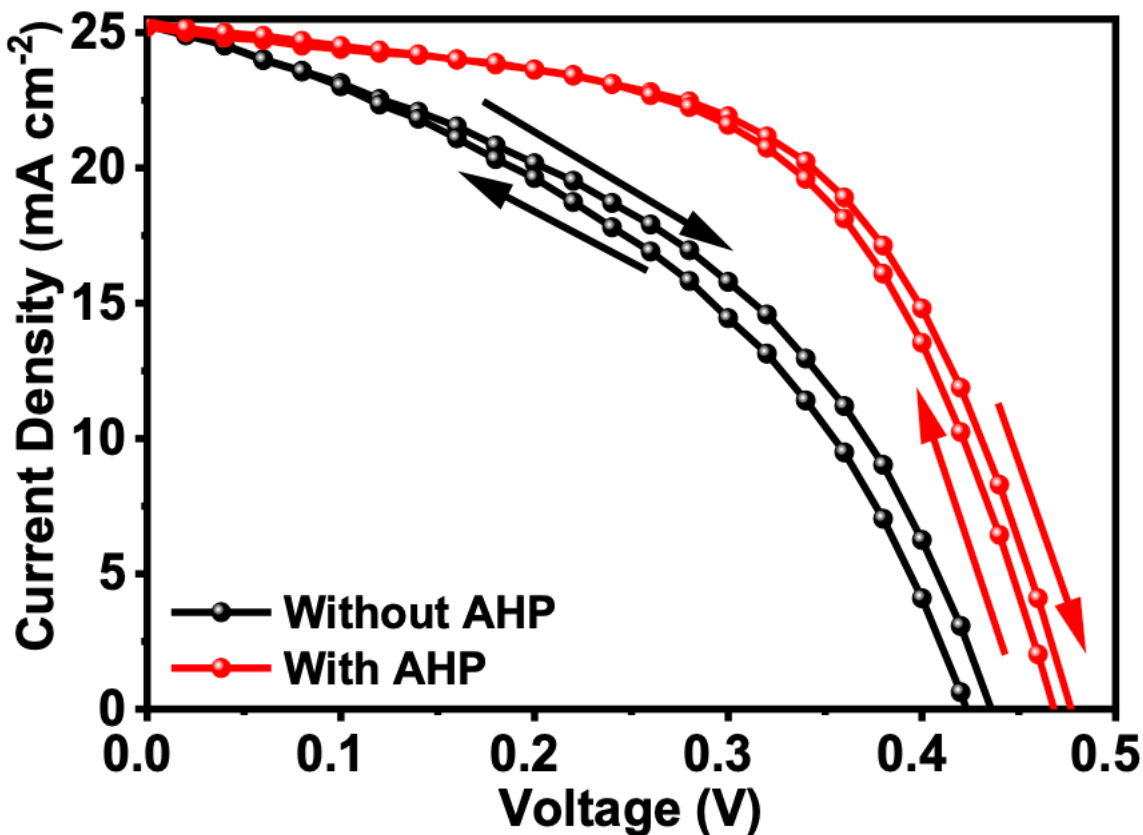


Figure 5.8. The J-V curves of the best solar cells fabricated from control films and films containing AHP.

The enhancement of the photovoltaic characteristics of the devices upon the addition of AHP is because of improved photoactive layer quality. When 5% AHP was included into the perovskite precursor solution, the final perovskite film showed magnified stability as compared to the reference film, the enhanced stability reduced chances of formation of Sn vacancies in the film. Sn vacancies are generated from the oxidation of Sn^{2+} in the perovskite film to Sn^{4+} ; the vacancies act as charge trap centers and hence increase charge non-radiative recombination in the devices (H. B. Lee *et al.*, 2019). The reference film showed lower performance due to low stability, poor charge transport in the film, and poor morphology as observed under XRD, TRPL, and SEM data respectively.

Perovskite solar cells, especially Sn-PSCs, experience anomalous $J - V$ responses on the voltage differing on the scan direction during photovoltaic characterization of the devices. This anomalous behavior is known as hysteresis. The actual PCE of Sn-PSCs is not easy to determine if the device

is experiencing hysteresis (B. Chen *et al.*, 2016). Hysteresis in devices is estimated using the hysteresis index (HI) equation, equation 5.3.

$$HI = \frac{PCE_{forward} - PCE_{reverse}}{PCE_{forward}} \quad 5.3$$

$$HI_{reference-device} = \frac{(4.74 - 4.42)}{4.74} = 0.0675$$

$$HI_{AHP-device} = \frac{(6.87 - 6.65)}{6.87} = 0.0320$$

The HI of the reference device is 0.0675, which is approximately twice that of 5% AHP-based devices. The reduced hysteresis in the AHP-based solar cells is because of improved charge extraction within the device, which is a result of reduced charge trap sites (B. Chen *et al.*, 2016). From the PL and TRPL data, the charge dynamics were noted to be poor in the reference devices because of the numerous defects resulting from phase segregation caused by excess SnF₂, and pinholes as observed under the SEM images. Thus, it can be conjectured that passivating defects within the photoactive layer of tin perovskite solar cells can greatly reduce the energy losses due to hysteresis in Sn-PSCs.

Steady-state power conversion efficiencies of the devices with and without 5% AHP were tracked as shown in Figure 5.9, to determine their reliability. The steady PCE was measured under light (standard illumination of AM 1.5 G), soaking with a bias voltage of 0.29 V and 0.34 V for devices without and with 5% AHP, respectively. The PCE of the two devices under light soaking for 130 s stood at 4.74% and 6.87% with a photocurrent density of 17.37 and 20.17 mAcm⁻² for devices without and with 5% AHP, respectively. All the devices seemed stable under light soaking for a short period, 130 s; showing that AHP does not only enhance the stability of the Sn-PSCs but in addition improves the PCE of the Sn-PSCs.

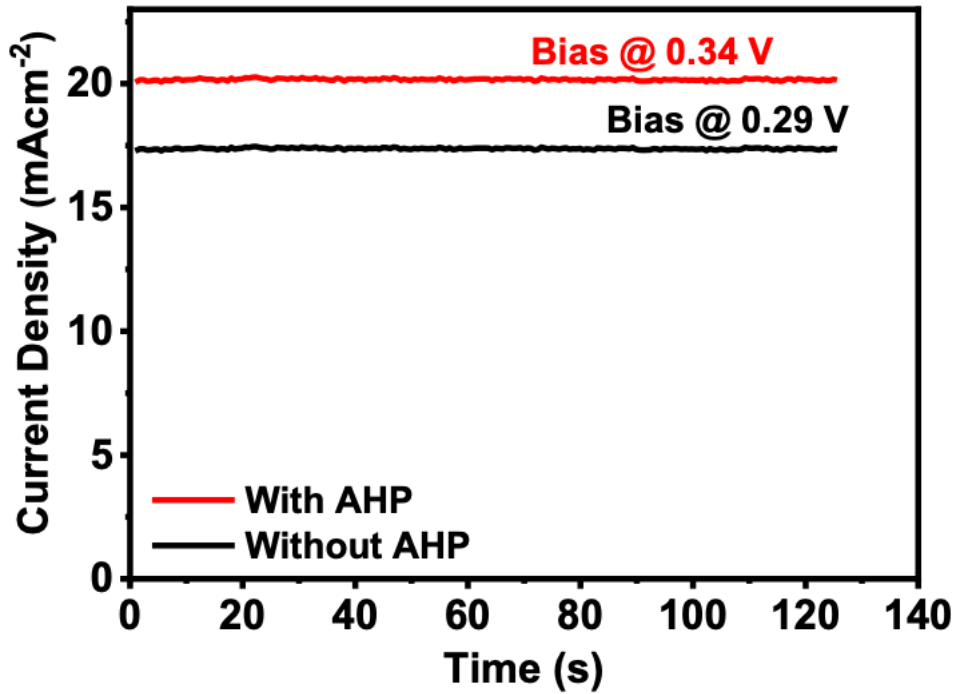


Figure 5.9. Steady-state PCE of devices fabricated with absorber film with and without 5 % AHP

The reproducibility of Sn-PSCs is a primary challenge in improving further its PCEs. Different research groups cannot reproduce the PCE results of other groups even if they follow all the procedures correctly. The main challenge is the facial oxidation of Sn²⁺ in the perovskite, some researchers have even noticed that different batches of SnI₂ irrespective of their purity, still contain some trace amount of Sn⁴⁺ (Hao *et al.*, 2014). Furthermore, the uncontrollable crystallization of Sn-perovskite films giving rise to poor morphology films with poor film-substrate coverage (Ji *et al.*, 2022). The poor-quality films lead to poor PCE as it contains many charge recombination centers. These challenges are also experienced at individual research groups and the performance of the Sn-PSCs in a group cannot be standardized. In this study, the devices having AHP additive in the photoactive layer showed some reproducibility as can be seen from the histogram, the AHP-based devices' performance ranged between 4 – 6.8% while the performance of the reference devices showed a range of 2.5 – 5%. The majority of the performing devices from the histogram are AHP showing that AHP can enhance the reproducibility of the Sn-PSCs.

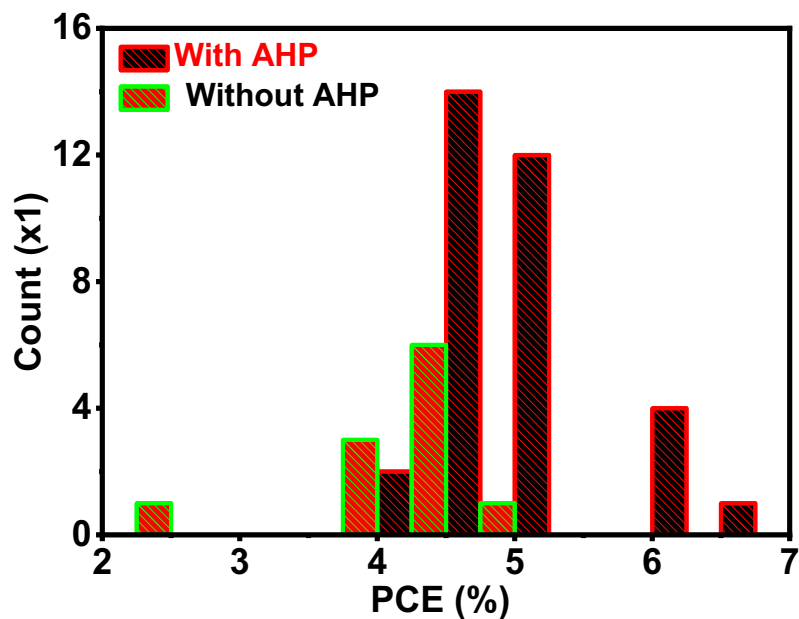


Figure 5.10. The histogram shows the performance of some of the fabricated devices.

The stability of both Sn-perovskite layers and devices is another challenge in improving the device PCE of Sn-PSCs. Sn-PSCs are very unstable in the ambient atmosphere because of the fast oxidation of Sn^{2+} ions in the perovskite (Fan *et al.*, 2020). The stability of the unencapsulated solar cells stored in the glovebox was measured for a period of 30 days at intervals of 5 days as shown in Figure 5.11(a). After 30 days, the AHP-based device retained up to 97% of its original PCE, and the pristine device reserved only 79% of its primary PCE. The enhancement in the stability of the devices shows that the trap states within the absorber layer and devices are greatly reduced due to the reaction between AHP and SnF_2 . The results further showed that using both AHP and SnF_2 could passivate the perovskite and hence improve its stability.

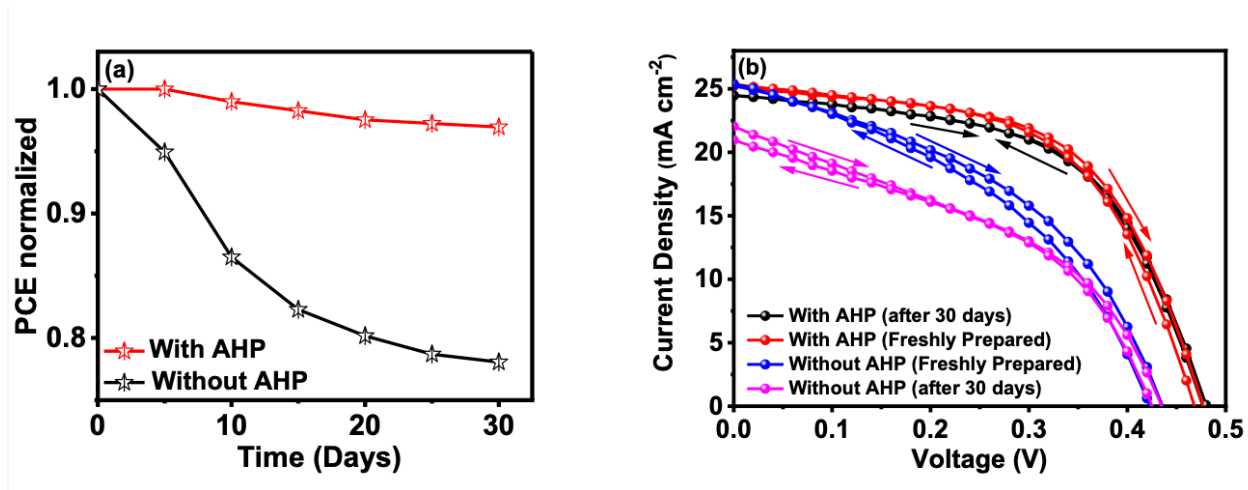


Figure 5.11. (a) Stability of the Sn-PSCs with and without 5 % AHP under light soaking (b) J-V curves of freshly fabricated devices and devices stored after 30 days.

The $J - V$ curves of the fresh and degraded solar cells are as indicated in Figure 5.11(b). The $J - V$ curve of the AHP-based film showed negligible hysteresis after 30 days of storage. The absence of hysteresis is a result of reduced or no trap states within the device. It is speculated that the devices with AHP underwent a self-healing process or recrystallization, which can involve the slow reduction of any Sn^{4+} ions present in the devices immediately after fabrication and gaining proper contact at the photoactive layer and other charge transport layers interfaces, with storage time. Proper interaction between the active layer and ETL reduces the interfacial layer defects and thus reduces the radiative recombination of charges within the devices.

5.1.7 External Quantum Efficiency of the Devices

EQE in solar cells is known as incident photon to current conversion efficiency (IPCE) or spectral responsivity of photovoltaic devices. EQE measures the ability of photovoltaic devices to convert each incident photon into electrons; the electrons are then transmitted to an external circuit. EQE is expressed as a percentage of the flux of electrons collected by an external circuit to the flux of incident photons in a photovoltaic device during operations. EQE is a measure of how well a photovoltaic device can convert solar energy to electricity.

Both devices showed a spectral response up to 933 nm wavelength and showed higher EQE values in the visible region, above 65% for the 350 – 700 nm wavelength range as exhibited in Figure 5.12(a). The AHP devices displayed magnified EQE; the passivation of defects by the complex salt

formed between AHP-SnF₂ makes the devices more capable of collecting more charges (Gao *et al.*, 2018) because its capable of harvesting more incident light as shown under the UV-vis absorption measurement. The integrated J_{SC} of the two champion devices were 23.10 and 22.64 mA cm⁻², for Sn-PSCs with and without AHP, correspondingly. The integrated J_{SC} is similar to the J_{SC} obtained from the $J - V$ measurement. The slight variation could be because of the facial oxidation of tin perovskite in the air. Setting of EQE equipment takes time before actual measurement commences. During the setup process, the Sn-PSCs could have degraded.

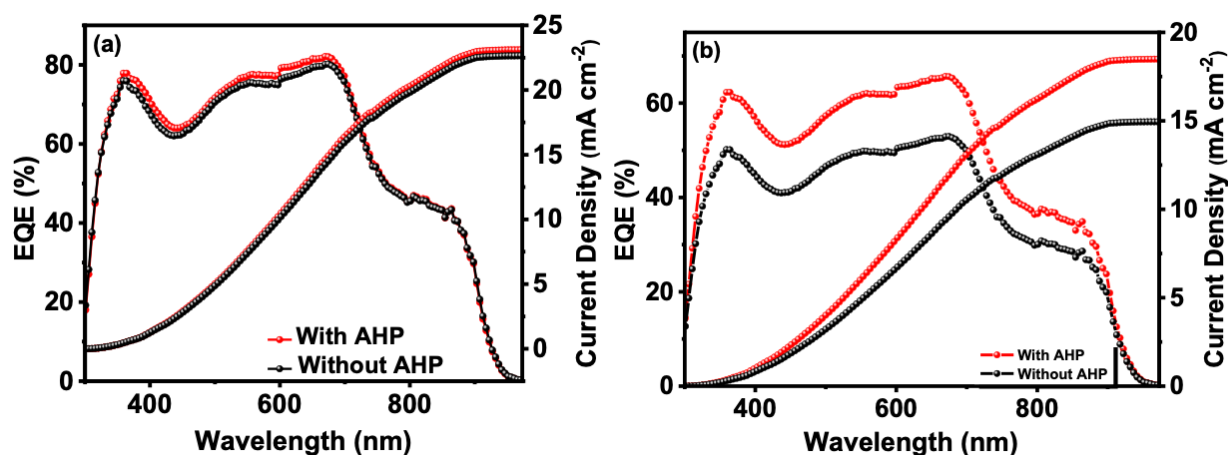


Figure 5.12. (a) EQE and the integrated photocurrent of Sn-PSCs with and without AHP. (b) EQE and the integrated photocurrent of the devices with and without AHP after exposure to air for 20 minutes.

The EQE measurement was later done 20 minutes after the films experienced the ambient atmosphere to justify the decomposition claim of the devices in the air as shown in Figure 5.12(b). The EQE and integrated J_{SC} substantially reduced; showing just how vulnerable the devices were to air oxidation. The result proved that AHP can passivate tin perovskite film to improve its quality for better device performance but still cannot inhibit oxidation if the device is exposed to the ambient atmosphere.

5.2 FASnI₃ films and solar cells

5.2.1 Film Morphology

After successfully using AHP as a co-additive on FA_{0.50}MA_{0.45}PEA_{0.05}SnI_{3.00} to annihilate the phase separation resulting from excess SnF₂, AHP was then employed on FASnI₃-based perovskite to improve the film optoelectronic properties and subsequently advance the PCE of Sn-PSCs resulting from AHP- FASnI₃ modified films. FASnI₃ was investigated since it shows improved stability as compared to its MASnI₃ counterpart, in addition, devices based on FASnI₃ show better performance and reproducibility (S. Li *et al.*, 2022). The morphology of the pristine FASnI₃ and AHP- FASnI₃ were studied using the SEM technique as displayed in Figure 5.13.

Figure 5.13(a) displays the morphology of the pristine FASnI₃ film, the pristine film has visible pinholes and many other unwanted phases on the surface of the film. The film coverage is perfect because of the solvent engineering technique that was involved in the deposition process. The magnified image in the inset of Figure 5.13(a) shows the unwanted phases lying on the surface of the film, causing non-uniformity in the film morphology. In addition, the magnified image shows grains with sharp grain boundaries and random orientation. The sharp grain boundaries are detrimental as they act as charge trap centers and inhibit proper contact between the absorber layer and subsequently deposited electron transport layer (Q. Jiang *et al.*, 2019; Y. Jiang *et al.*, 2022). The aggregates act as charge trap centers and hence the need to eliminate them. Even though SnF₂ has shown to be dangerous on the tin-perovskites, it has become an integral part of lead-free perovskite and cannot be eliminated; it assists in strengthening the Sn-I bond and boosts the strength of the [SnI₆]⁴⁻ octahedral structures. The strengthening of Sn-I and [SnI₆]⁴⁻ helps in having better films with improved photoelectric performance such as improved absorption coefficient (Xie *et al.*, 2021).

The aggregates disappeared upon the incorporation of the AHP in the film as exhibited in Figure 5.13(b and c). However, there are other black spots on the films containing excess AHP (Figure 5.13 (c)), the black phases could be a result of the formation of a thicker layer of the complex salt between SnF₂ and AHP. The mechanism of the disappearance of the aggregates is as earlier explained under the FTIR measurement in section 5.1.2. The grain sizes significantly improved and the uniformity of the perovskite surface improved. As indicated in Figure 5.14, the grain sizes of the pristine film were between 0.4 and 1.6 μm, with the majority of the grain falling between

0.8 and 1.0 μm as shown in Figure 5.14(a). The addition of 5% AHP improved the grain sizes and the majority of the grain sizes lay between 1.0 and 1.4 μm , Figure 5.14(b). However, excess AHP is detrimental as it reduced the grain sizes as displayed in Figure 5.14(c).

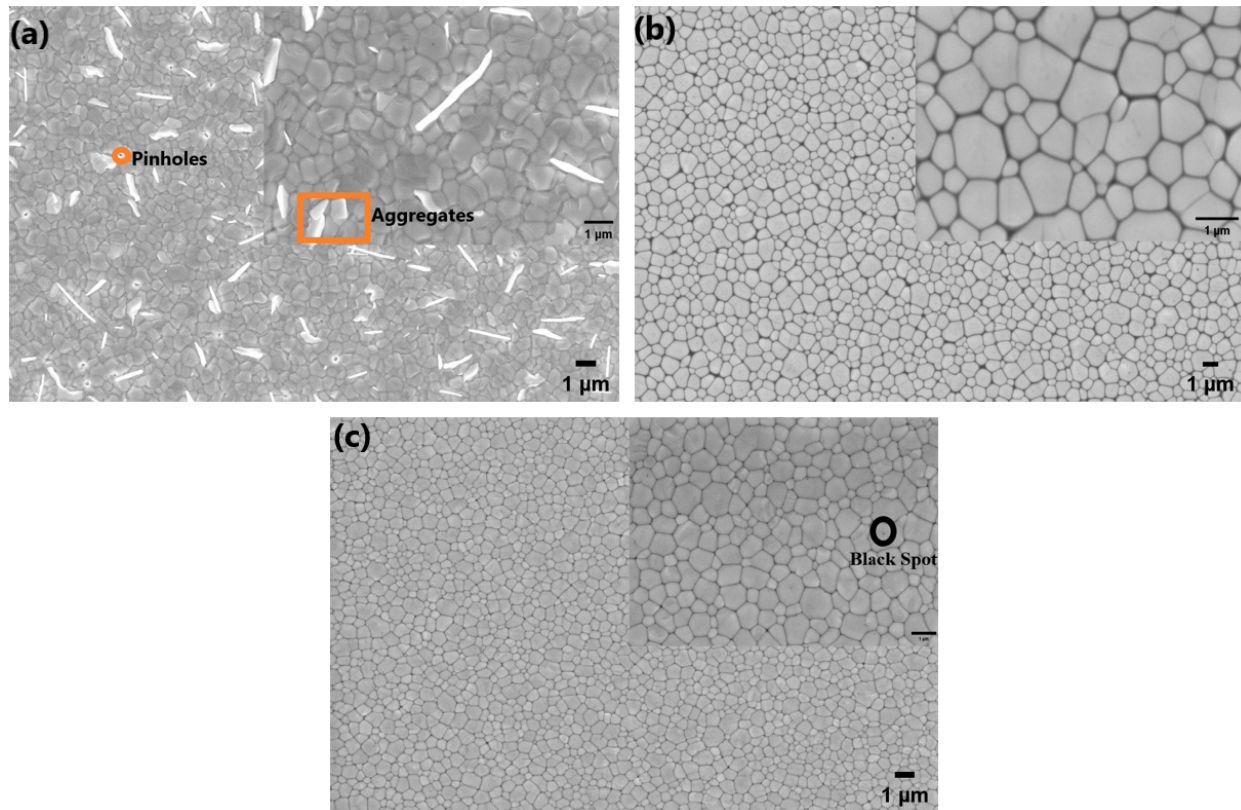


Figure 5.13. SEM images of the FASnI_3 films containing (a) 0% (b) 5% and (c) 10%, of AHP.

The spread of AHP- SnF_2 complex salt on the surface of Sn-perovskite layer was determined using SEM-EDS elemental mapping as shown in Figure 5.15. During the measurements, the distribution of the characteristic elements in the additives such as F and P was considered. From Figure 5.15(a and b), the distribution of the two elements is uniform and dense on the surface, showing that the complex salt formed after the reaction between AHP and SnF_2 clearly passivated the surface of Sn-perovskite layer.

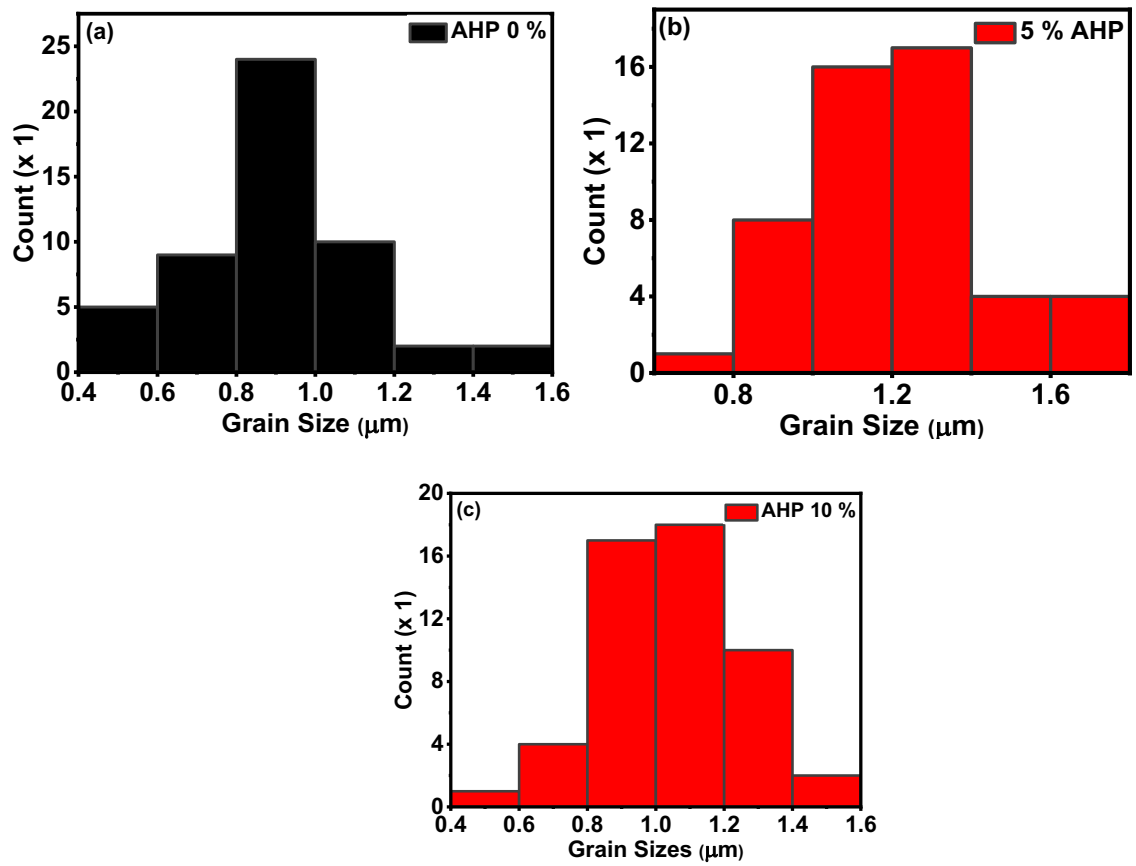


Figure 5.14. Histograms of grain sizes of the FASnI₃ films with varied amounts of AHP.

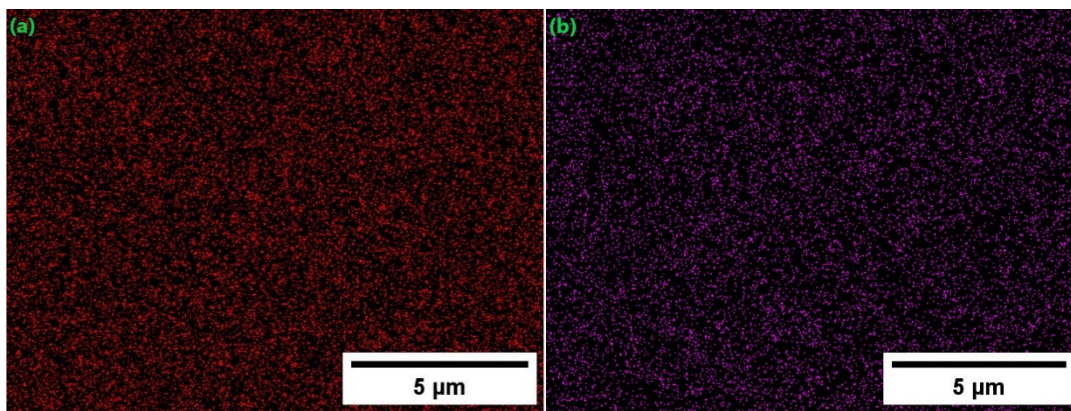


Figure 5.15. SEM-EDS elemental mapping of (a) F and (b) P distribution on film containing both AHP and SnF₂

5.2.2 The Perovskite Film Structural Measurement

The XRD pattern was used to investigate the structural effect of AHP on FASnI₃ perovskite as displayed in Figure 5.16. The main observed peaks are (100), (102), (200), (122), (222), and (213), which correspond to 14.0, 24.4, 28.1, 31.6, 40.4, and 42.9° of 2 theta. The addition of AHP into the film did not change its lattice structure, as the observed structure is the normal orthorhombic structure of FASnI₃ perovskite. Instead, the AHP enhanced the crystallinity of the films, which is shown by the increased XRD intensity peaks of the AHP films. From the morphology studies, it was discovered that the complex salt formed between AHP and SnF₂ interaction deposits on the film surface and grain boundaries. The complex salt as seen in the XRD data can be detrimental to the film if it is in excess, as the amount of AHP was increased to 10%, the peak intensity of the films reduced, which is in support of the results from the SEM. The small black spots observed in the morphology of the films having excess AHP are harmful to the superiority of FASnI₃ film, and thus the quantity of AHP should be maintained at 5% for better film quality and solar cell performance

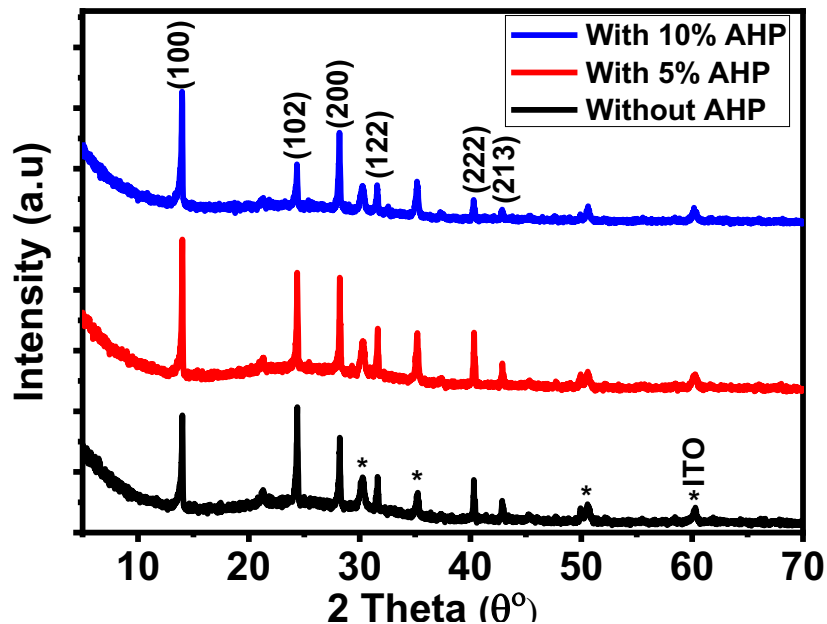


Figure 5.16. The XRD patterns of FASnI₃ films fabricated with varied amounts of AHP.

The crystallite size was approximated using the XRD pattern and Scherrer equation (equation 5.4) (Ahmed *et al.*, 2022).

$$D_{size} = \frac{K\lambda}{\beta_T} \cdot \frac{1}{\cos\theta} \quad 5.4$$

Where D_{size} , K , λ , θ , and β_T are the average crystallite size, Scherrer constant (taken as 0.9), the wavelength of incident X-ray radiation (0.154 nm), the diffraction angle, and the FWHM in radians.

The FWHM was approximated using the peak (100) located at 14° as shown in Figure 5.17. FWHM are 0.098° and 0.120° for the AHP and pristine film; the small FWHM of AHP-based film confirms the refined crystallinity of the perovskite film upon AHP addition. The calculated FWHM Crystallite size for films without AHP is 68.98 nm and that for films with AHP is 90.98 nm. The improved crystallite size shows that AHP can modify the crystallization of the Sn-perovskite, and hence improve the quality of the films.

The micro-strain (ϵ) in the perovskite films, AHP-based and pristine films were estimated using Williamson-Hall (WH) equation (equation 5.5) (Ryu *et al.*, 2023). All the parameters are as defined in equation 5.4, except for β_T which is in degrees. The values of the micro-strain are 11.87% and 8.87% for AHP and pristine perovskite films. Micro-strains induce defects and charge trap centers in perovskite films (S. Wang *et al.*, 2022). Therefore, the reduced micro-strain value of AHP film is an indication of reduced defects within the perovskite film. This result further confirmed the ability of AHP to inhibit defect formation in Sn-perovskite films.

$$\beta_T \cos\theta = \frac{K\lambda}{D_{size}} + 4\epsilon \sin\theta \quad 5.5$$

Where β_T represents FWHM in degrees, θ represents the Bragg angle, λ represents the wavelength of the used X-ray, D_{size} represents the average crystallite size,

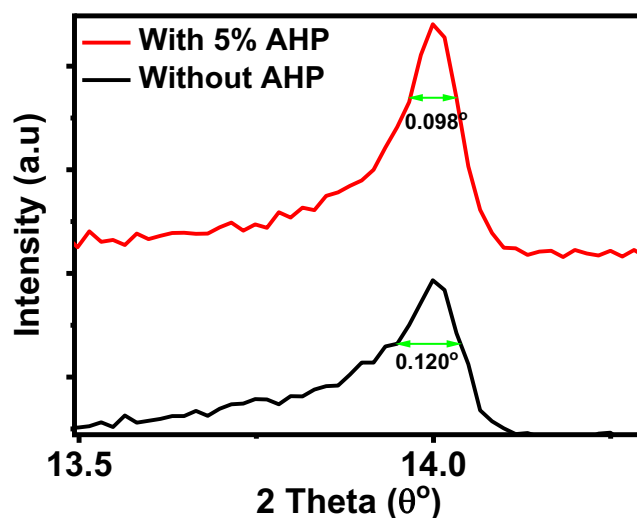


Figure 5.17 Magnification of peak (100) of Figure 5.16 for FWHM approximation for films with and without AHP.

5.2.3 Absorption Spectra of FASnI₃

The optical characteristics of FASnI₃ layers were studied using the UV-vis spectra as displayed in Figure 5.18(a and b). The AHP slightly enhanced the light absorption of the FASnI₃ film as shown in Figure 5.18(a), which is in accordance with the superb film morphology observed under the SEM scans. Adding excess AHP, 10 %, has no obvious effect on the absorption onset or absorption of the FASnI₃, and thus no need to find the band gap of the 10 % AHP-based film. NHIFP-ID

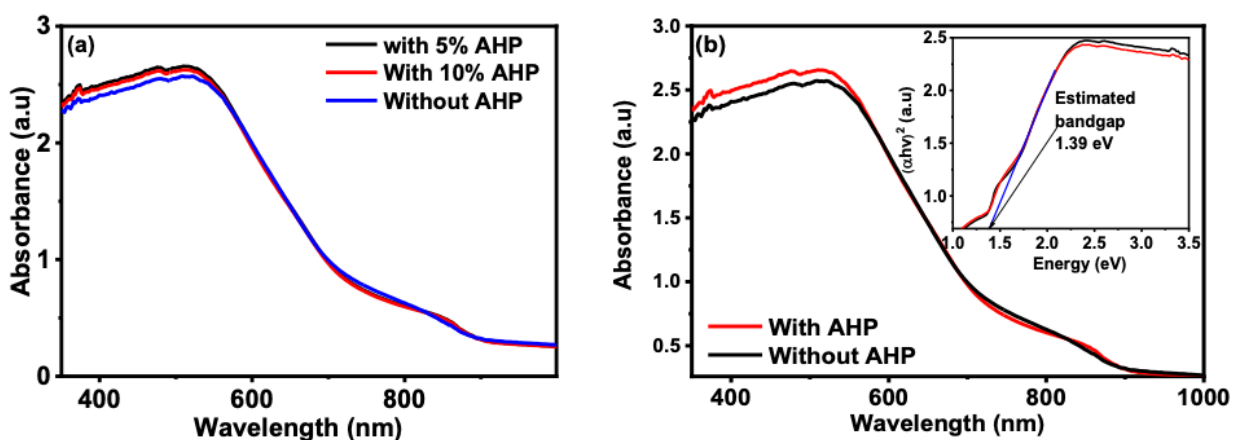


Figure 5.18. (a) Absorption spectra of films with varied amounts of AHP, (b) Absorption spectra of films with and without 5% AHP; the inset is a graph of $(\alpha hv)^2$ versus (hv) used to estimate the bandgaps of the films

5.2.4 Photoluminescence and Time-resolved photoluminescence measurement

Steady-state photoluminescence (PL) measurement was done to confirm the optical features and to comprehend the charge transport of the perovskite layers prepared by utilizing SnF₂ only and using a mixture of SnF₂ and AHP. There was no obvious PL peak shift in the PL spectrum as witnessed in Figure 5.19(a). The PL strength of the film comprising 5% of AHP was higher than the film having pure SnF₂, indicating that the additive can easily passivate both deep and surface defects in Sn-perovskite absorber layers. The passivation of defects results in the clampdown of charge recombination centers making the films favourable for the making of high-PCE Sn-PSCs (Z. Lin *et al.*, 2020). However, an increase in the amount of AHP reduced the PL peak intensity of the perovskite film; the reduced intensity is due to other unwanted phases instigated by the deposition of excess AHP-SnF₂ complex salt on the surface of the film.

Time-resolved PL (TRPL) spectroscopy was used to understand the charge dynamics of films with and without AHP. The TRPL spectra shown in Figure 5.19(b), were fitted by a bi-exponential

function, and the average carrier lifetime (τ_{avg}) calculated using $\tau_{avg} = \frac{\tau_1 B_1 + \tau_2 B_2}{B_1 + B_2}$, where τ_1, τ_2 ,

The AHP-based films exhibited amplified carrier lifetime, an sign of suppressed trap state concentrations in the films (Jokar *et al.*, 2021; J. F. Liao *et al.*, 2019). The observation under the TRPL measurement was in accordance with the SEM results; from the SEM images, the addition of AHP improved the quality of the film, observed in the elimination of phase segregation and pinholes, leading to reduced charge recombination centers (Kayesh *et al.*, 2018; Z. Lin *et al.*, 2020).

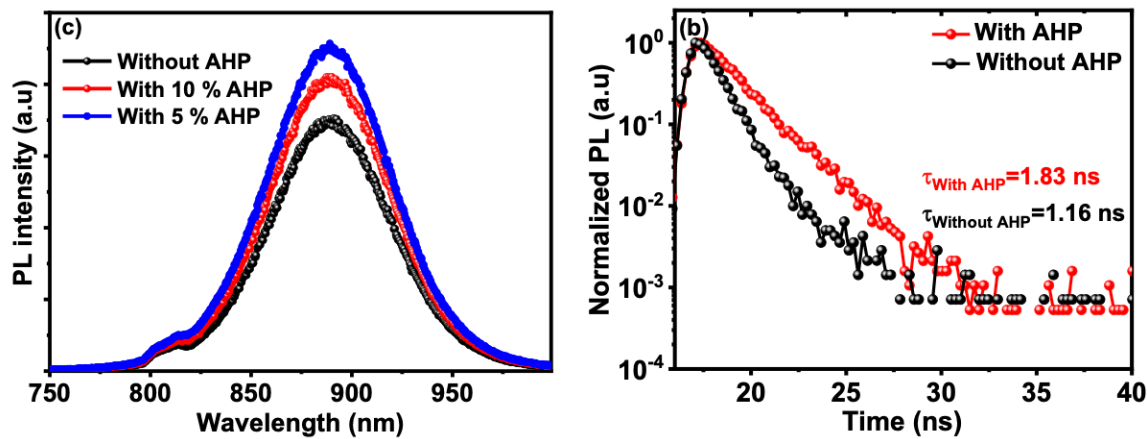


Figure 5.19 (a) PL spectra of FASnI₃ with varied amounts of AHP, (b) TRPL spectra of FASnI₃ with and without 5% AHP.

5.2.5 Photovoltaic Properties of the FASnI₃ Solar Cells

The effect of adding AHP to the FASnI₃ layer on the device's PCE was investigated. After studying the optoelectronic characteristics of the perovskite with 0, 5 and 10% AHP, it was decided that it would be best to only fabricate devices with 0% AHP, referred to as reference devices, and devices with 5% AHP, referred to as modified devices. The 10% AHP seemed to be reducing the quality of the FASnI₃ throughout and that is why it is not scientifically meaningful to fabricate devices consisting of 10% AHP. Inverted solar cells with the structure ITO/ FASnI₃ (with and without 5% AHP)/PC₆₀BM/Ag were fabricated for the PCE investigation.

Table 5.2 shows the summary of the PCE characteristics statistics of the devices fabricated based on the FASnI₃ perovskite absorber layer. The reference devices showed a PCE of 3.81±0.17%, J_{SC} of 21.91 mA cm⁻², V_{OC} of 0.31±0.01 V, and FF of 53.18±4.89% in the forward PCE scan direction, with the champion device showing a performance of 4.04% in the forward scan direction. The modified devices showed an average PCE of 4.43±0.41%, J_{SC} of 22.80±2.45 mA cm⁻², V_{OC} of 0.33±0.02 V, and FF of 57.79±5.06 % in the forward PCE scan direction, with the champion device showing a PCE of 5.48% with an improved FF and V_{OC} of 66.36 % and 0.37 V, respectively in the forward direction scan.

The statistics show that AHP addition to the absorber material obviously enhanced the PCE of the developed devices. From, the optoelectronic characterization of the FASnI₃ films, it was shown that AHP addition in the film improves the characteristic of the absorber film by eliminating the pinholes and unwanted phases formed because of SnF₂ addition. The PL and TRPL data further showed that AHP can help in suppressing the nonradioactive recombination in Sn-perovskite films and hence reduces the chances of charge recombination within the devices. Reduction of charge recombination ensures that as many generated charges in the absorber layer are collected at the contact to improve the PCE of the device.

Table 5.2. A summary of the photovoltaic properties of the developed devices, both modified and reference devices.

	V _{oc} (V)		J _{sc} (mA·cm ⁻²)		FF (%)		PCE (%)	
	Forward	Backward	Forward	Backward	Forward	Backward	Forward	Backward
Without AHP (Champion)	0.33	0.30	21.00	18.40	57.93	40.61	4.04	2.26
Without AHP (Average)	0.32±0.01	0.31±0.01	21.91±2.79	21.68±2.95	53.18±4.89	46.19±3.52	3.81±0.17	3.06±0.58
With AHP (Champion)	0.37	0.37	22.25	22.08	66.36	64.91	5.48	5.24
With AHP (Average)	0.34±0.02	0.33±0.02	22.80±2.45	22.79±2.67	57.79±5.06	54.13±6.41	4.43±0.41	4.02±0.61

Figure 5.20 shows the $J - V$ curves of both control and modified device. From the curves, it is evident that the two devices experience hysteresis. The HI was calculated as:

$$HI_{reference-device} = \frac{(4.04 - 2.26)}{4.04} = 0.4405$$

$$HI_{modified-device} = \frac{(5.48 - 5.24)}{5.48} = 0.0438$$

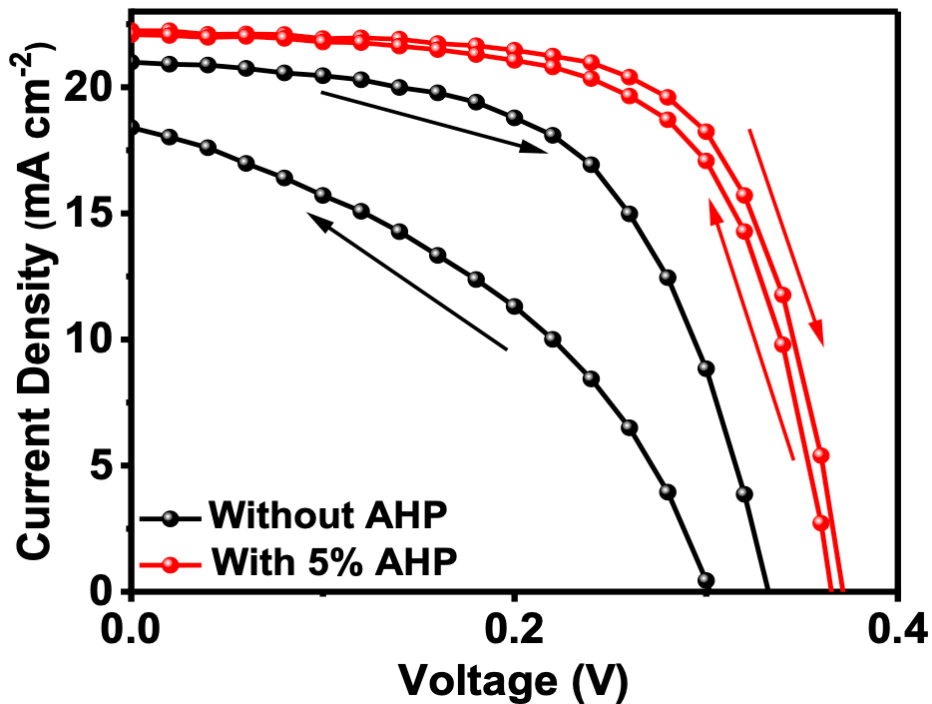


Figure 5.20. The $J - V$ curves of the best solar cells fabricated from control films and films containing both AHP and SnF₂ additives.

The reference showed almost 10 times more hysteresis than the modified device. Hysteresis in solar cells is mostly a result of excessive recombination of charges within the devices due to defects within the absorber layer or the other layers in the device (Ono *et al.*, 2015). In this study, the SEM images showed that the reference device harbours a large number of unwanted phases and pinholes which can act as charge trap centers and hence the hysteresis. From the TRPL data in this work, AHP-based devices have enhanced charge carrier lifetime allowing for enough time for charge extraction by the hole and electron transporting layer hence the reduced hysteresis. The V_{oc} of reference devices is also low due to the phase separation as witnessed in the SEM images. Figure 5.21 is a histogram showing the reproducibility of modified and control devices.

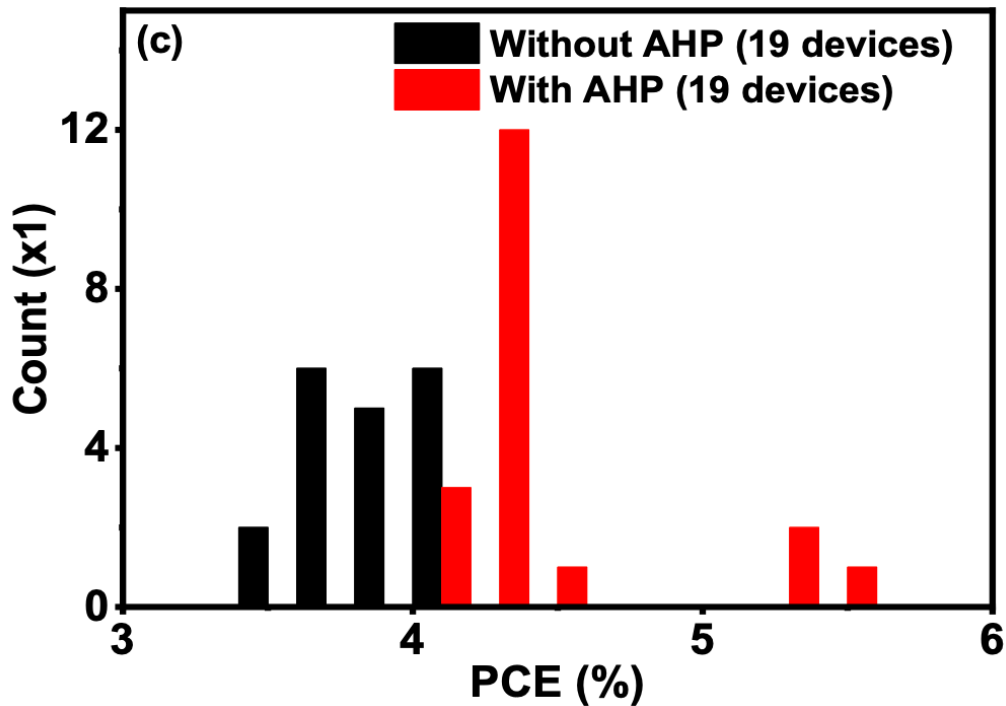


Figure 5.21. The histogram shows the performance of some of the fabricated devices.

Steady-state power conversion efficiencies of the modified and reference device were measured for a period of 120 s as indicated in Figure 5.22(a). The devices showed a steady power output of 4.00% and 5.40% for control and modified devices, the performances are comparable to performances under the $J - V$ curves. The stability of the unencapsulated devices kept in a nitrogen-filled glovebox was investigated as indicated in Figure 5.22(a). The modified device

showed better stability due to the passivation effect of AHP-SnF₂ complex salt. Therefore, AHP can improve both PCE and stability of FASnI₃-SCs.

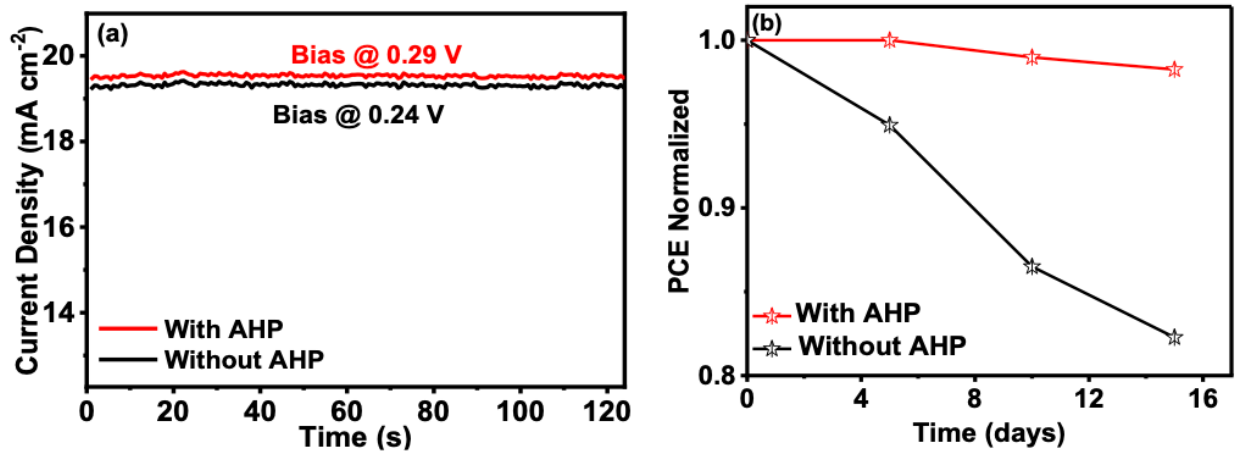


Figure 5.22. (a) Steady-state PCE of the reference and modified device (b) Stability test of the reference and modified device.

The EQE of the best reference and modified FASnI₃-PSCs were measured as indicated in Figure 5.23. The EQE curves confirm the better absorbance of AHP-based devices as was seen under the optical data. The integrated J_{SC} of the devices from the EQE graphs were 21.03 and 20.42 mA cm⁻², which are comparable to the J_{SC} , obtained under the J-V curve.

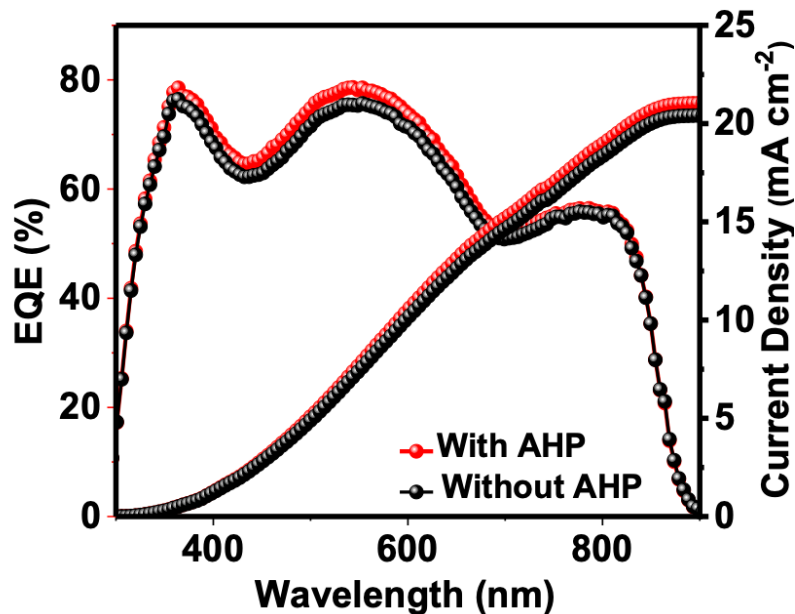


Figure 5.23. EQE and the integrated photocurrent of the cells of the reference and modified devices

5.3 FA_{0.70}EA_{0.15}PEA_{0.15}SnI_{2.70}Br_{0.30} Solar Cells

5.3.1 Photovoltaic Performance

Sn-PSCs with the architectural structure of ITO/PEDOT:PSS/perovskite/PC₆₁BM+P3HT/PDINN/Cu, ITO/PEDOT:PSS/perovskite/PC₆₁BM+P3HT/BCP/Cu and ITO/PEDOT:PSS/perovskite/PC₆₁BM+P3HT/Cu were fabricated.

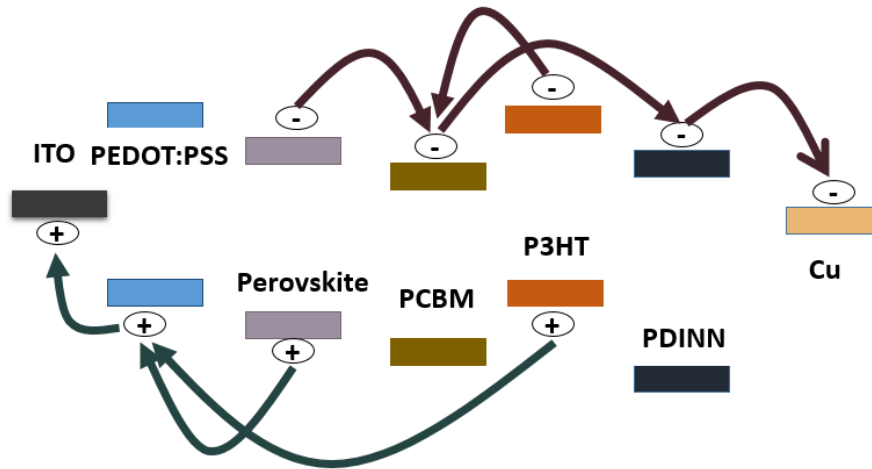


Figure 5.24. The possible flow of electrons and holes in a PCBM+P3HT system

P3HT system was used to boost the PCE and stability of the devices. Alidaei et al. (2019) noted that P3HT can enhance recombination resistance and result to a reduction in charge accumulation at the interfaces. The group also noted that P3HT is capable of enhancing the stability of perovskite solar cells (Alidaei *et al.*, 2019). The ability of P3HT to enhance the stability of PSCs is based on its ability to form on top of PCBM since it has a lower surface formation energy (Kokubu & Yang, 2012). The formed P3HT on top of the PCBM passivates the PCBM and encapsulates the other layers of the PSCs, thus protecting the absorber layer from degrading agents. P3HT leads to higher PSCs performance because of its ability to absorb photons in the visible region, thereby leading to the generation of more electrons and holes in the device (Alidaei *et al.*, 2019). The generated electrons and holes are collected as displayed in Figure 5.25, giving rise to increased performance.

The PCE of the devices was measured to relate the photovoltaic performances of devices with and without buffer layers. The PCE was measured for the freshly fabricated cells as shown in Figure

5.26(a), the champion devices for the devices without buffer layer and with BCP and PDINN measured in the forward direction were 7.34%, 9.94%, and 10.06%, respectively. The reduced performance of the device without a buffer layer as seen in Figure 5.26(a) is due to the reduced J_{SC} and V_{OC} of the device; the reduced J_{SC} could be due to the increased Schottky barrier between Cu and the ETL due to the lack of an ohmic contact (Asgary *et al.*, 2021). BCP and PDINN devices showed improved performance because of proper ohmic contact and possibly due to reduced charge accumulation and recombination at the Cu/ETL interface. However, the PDINN device showed a slightly better performance due to its ability to form strong contact with PCBM through its secondary amine groups (Yao *et al.*, 2020).

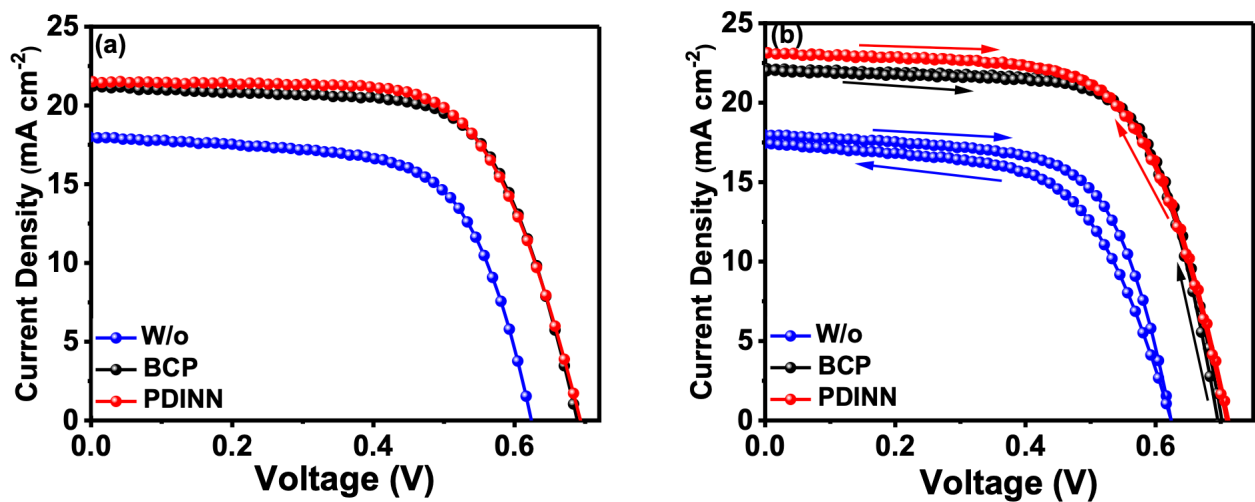


Figure 5.25. Current density-voltage ($J - V$) curves of (a) freshly prepared solar cells, (b) BCP and PDINN after 5 days, and the fresh device without buffer layer.

The Sn-PSCs were kept under a nitrogen-filled glovebox after the first measurement. All the measurements were done in the air with relative humidity between 26 and 38% and at room temperature. The PCE of PDINN and BCP devices improved to 10.99%, and 10.79%, respectively, while the performance of the device without a buffer layer reduced to 6.55%. Figure 5.26(b) displays the $J - V$ curves of the champion devices and therefore 7.34% of the pristine device curve was included instead of the reduced 6.55%. Figure 5.26(b) displays the $J - V$ curves of the PSCs after 5 days of storage (except for the control device); scanned in both reverse and forward directions. There was a slight PCE variation for the forward and reverse direction measurement, which is a result of hysteresis losses in the devices. The hysteresis was evaluated by determining

the hysteresis indexes of each device using $HI = \frac{PCE(forward) - PCE(reverse)}{and PCE(forward)}$. The HI of the control, BCP, and PDINN-based devices were 0.1076, 0.0092, and 0.0064, respectively. The reduced hysteresis in the devices with buffer layers is because of reduced charge accumulation at the ETL/Cu interface (Singh & Parashar, 2021).

The steady state PCE of the devices was measured and the curves were plotted as displayed in Figure 5.27(a). The steady power output and J_{SC} of the devices for 120 s at a bias voltage of 0.49, 0.54, and 0.54 V for control, BCP, and PDINN devices, respectively, were 7.33% (15.10 mA cm⁻²), 10.78% (20.29 mA cm⁻²) and 10.99% (20.31 mA cm⁻²), correspondingly. The PCE results are similar to those obtained from $J - V$ measurement curves. The reproducibility of the devices was determined using 20 independent devices as presented in Figure 5.27(b) and Table 5.3 (the table shows the parameters of the best devices based on each condition and the statistical average performance of the devices). The devices with buffer layers (PDINN and BCP) showed the lowest standard deviation showing high reproducibility. The low performance of the device without a buffer layer could be because of uncontrollable degradation during PCE measurements and storage. The buffer layer apart from creating ohmic contact can also provide self-encapsulation to the solar cells and hence protect them from naturally occurring degrading agents such as moisture and oxygen (N. Li *et al.*, 2017).

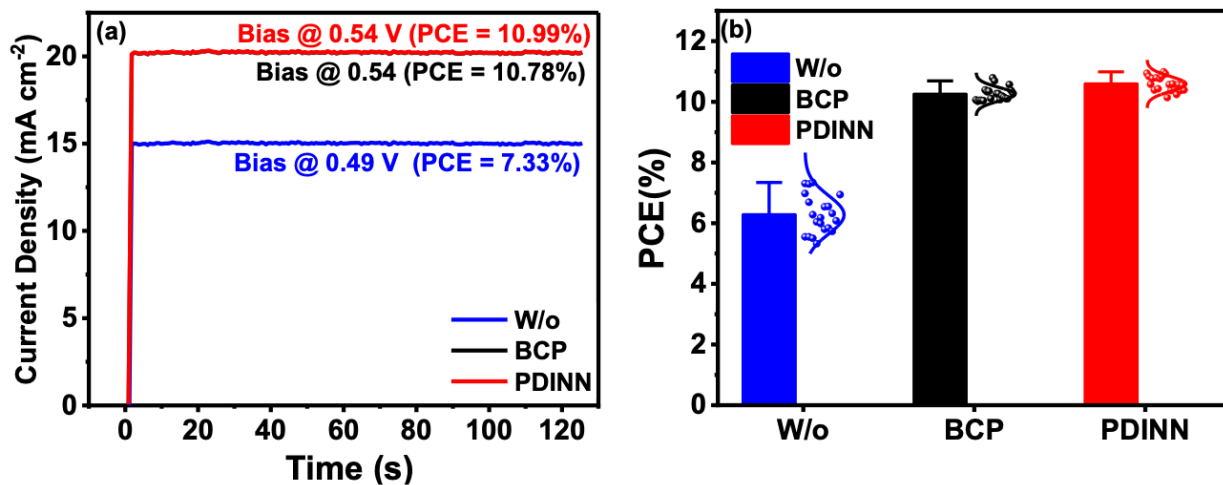


Figure 5.26. (a) Steady PCE output of the three devices. (b) The statistical representation of 20 devices of each condition.

Table 5. 3 Summary of the PCE parameters of the solar cells, for both individual champion cells and the statistical average.

	V_{oc} [V]	J_{sc} [mA cm^{-2}]	FF [%]	PCE [%]
W/o Champion	0.62	17.99	65.40	7.34
W/o Average	0.62 ± 0.02	16.56 ± 1.15	58.38 ± 6.54	6.02 ± 0.62
BCP Champion	0.70	22.14	69.41	10.79
BCP Average	0.69 ± 0.01	20.37 ± 0.31	69.55 ± 0.69	10.24 ± 0.20
PDINN Champion	0.71	23.15	66.65	10.99
PDINN Average	0.71 ± 0.01	22.09 ± 0.66	67.37 ± 1.50	10.60 ± 0.22

The EQE measurements of the devices were done with the spectra of the three champion devices in each condition plotted as shown in Figure 5.28(a). The EQE spectra ranged between 860 and 300 nm of light wavelength, the EQE onset at 860 nm reveals that the perovskite band gap was ~ 1.44 eV. The integrated current densities from the EQE measurement are 21.72, 21.62, and 17.43 mA cm^{-2} for PDINN, BCP, and pristine devices; the J_{sc} are comparable to those obtained from $J - V$ curves.

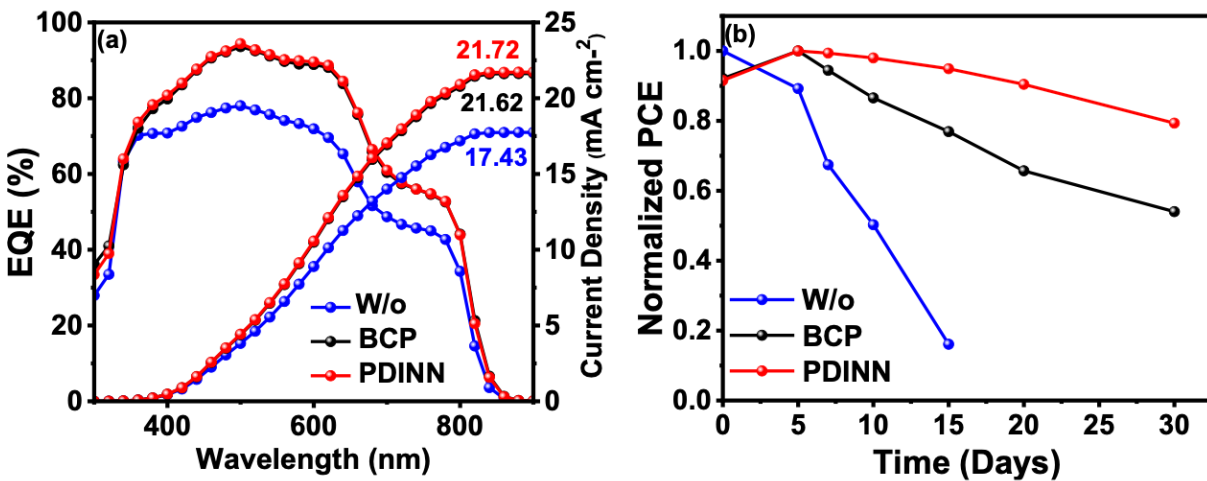


Figure 5.27. (a) The EQE curves of the three champion devices. (b) Stability measurement of the champion devices.

The stability of the devices was determined from the measurement of the storage stability of the unencapsulated devices. The stability graph shown in Figure 5.28(b) displays that the PCE of the pristine device declined throughout the storage time. Though, the performance of the devices with PDINN and BCP buffer layers peaked at the 5th day of storage and then started declining. The observation based on PDINN and BCP devices is consistent with observations of other researchers who have shown that the performance of perovskite solar cells can improve with an increase in storage time (Wijesekara *et al.*, 2021; Zheng *et al.*, 2023). Liu's group has associated the initial rise in PCE of Sn-PSCs to recrystallization of the perovskite film; where they showed that perovskite film quality can improve if stored in the right conditions and also if the right additive is used (Zheng *et al.*, 2023).

Zheng *et al.* (2023) however associated the rise in efficiency to n-type doping of the ETL (PCBM) by the escaping halides from the perovskite due to ion migration (Zheng *et al.*, 2023). In our case, we believe the two scenarios could have occurred leading to the rise in PCE. The sudden decline of PCE of the control device could be due to a lack of self-encapsulation as explained earlier. The device stability measurement of the control device was stopped on the 10th day since the PCE was very low and could not motivate further research in Sn-PSCs in terms of stability. After 30 days, the PDINN devices were able to retain up to 80% of their peak PCE, while the BCP device only maintained 54%. The high storage stability of PDINN devices was associated with its secondary amine group, which can create hydrogen bonds with PCBM to act as a strong sealant on the device, the sealing of the device keeps water and oxygen, which are the key degrading agents from reaching the perovskite. Figure 5.29(a, b, and c) displays the evolution of the $J - V$ curves with storage time.

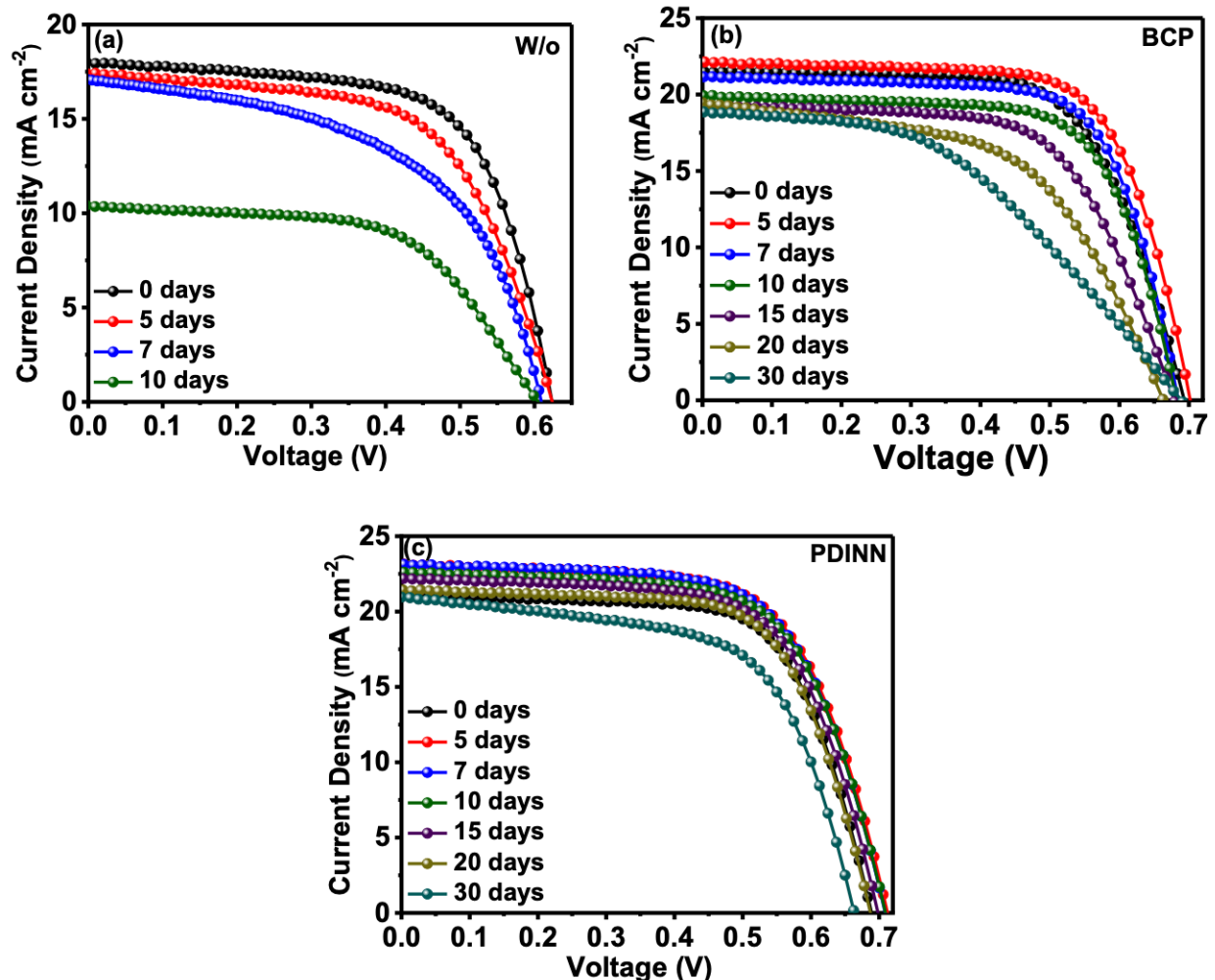


Figure 5.28. The storage evolution of the $J - V$ curves of (a) control device without buffer layer (b) BCP-based device and (c) PDINN-based device.

5.3.2 Potassium Thiocyanate (KSCN) and PDINN Optimization

The creation of highly-refined perovskite layers is critical in fabricating high-PCE PSCs. KSCN has been used by different research groups to improve the crystallinity, morphology, and stability of perovskite absorber material (F. Xu *et al.*, 2021). The use of KSCN has helped in the advancement of PCE and the reproducibility of Sn-PSCs (J. J. Cao *et al.*, 2022). Because of the advantages of KSCN, it was employed in this study to make the resulting solar cells. The KSCN concentration depends majorly on the perovskite material and thus must be optimized (J. J. Cao *et al.*, 2022; F. Xu *et al.*, 2021; R. Zhang *et al.*, 2019). KSCN optimization was done directly by fabricating solar cells with different concentrations of KSCN on top of PEDOT:PSS; KSCN was

used as interlayer material. Table 5.4 and Figure 5.30(a) show the detailed PCE performance and the variation of the PCE and PCE parameters with KSCN concentration. From Figure 5.30(a) it is clear that the PCE upsurges with a rise in KSCN concentration up to 5 mg mL⁻¹, and then the PCE shrinks with upsurge in concentration of KSCN. The increase in PCE is associated with an increase in the PCE parameters, especially increase in V_{OC} and FF .

Table 5.4 Optimization of KSCN concentration in DMF

Concentration (mg mL ⁻¹)	V_{OC} [V]	J_{SC} [mA cm ⁻²]	FF [%]	PCE [%]
0	0.63	19.94	65.6	8.28
2	0.65	20.17	68.18	8.98
5	0.69	21.22	68.85	10.06
10	0.66	22.00	68.45	9.92
15	0.64	22.92	66.05	9.73

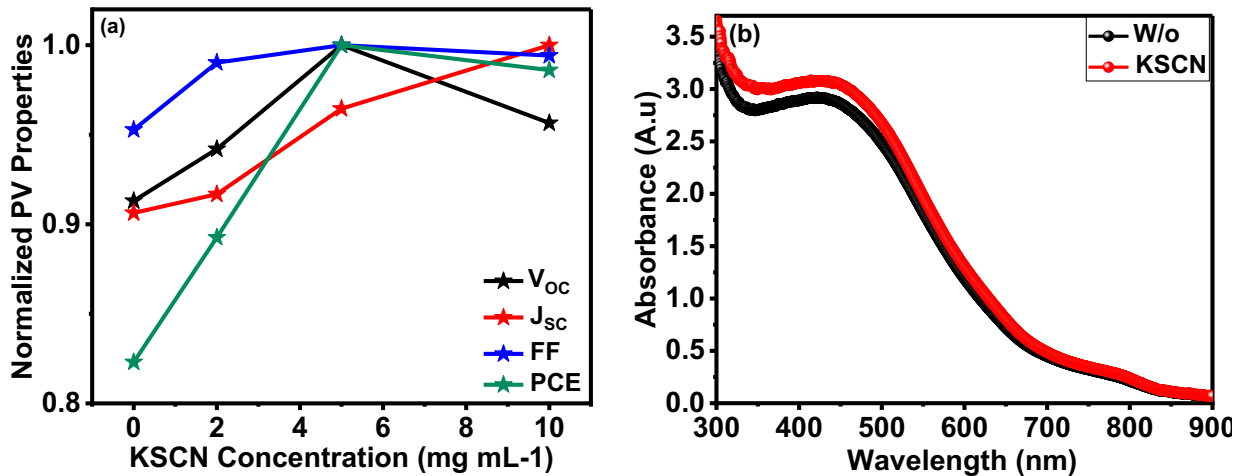


Figure 5.29. (a) The variation of the photovoltaic properties of the devices with KSCN concentration. (b) The optical absorption spectra of perovskite films deposited on plain glass and on glass coated with KSCN.

The increase in V_{OC} could be a result of defect reduction between the perovskite and PEDOT:PSS layers. High defect concentration has been shown to highly contribute to the low V_{OC} observed in Sn-PSCs (Y. Jiang *et al.*, 2022; Zheng *et al.*, 2023). Another possible reason for the increase of V_{OC} to the optimal amount of KSCN could be due to the matching of energy levels between the perovskite and PEDOT:PSS; matching energy levels facilitates direct charge transport within the PSCs and inhibits charge accumulation and recombination responsible for the reduction of V_{OC} (X. Jiang *et al.*, 2020). The J_{SC} was observed to increase linearly with an increase in KSCN, which could be due to an increase in compactness of the perovskite, but the high J_{SC} after the KSCN optimal value is useless since it cannot compensate for the V_{OC} loss of the devices to result in higher performance. The rise in J_{SC} was investigated using Uv-ViS absorbance data as shown in Figure 5.30(b), the graph shows that KSCN can increase the light absorbance of the film in the visible region resulting in the enhanced J_{SC} . No further characterization was done on the absorber material, as it was not the primary idea in this section of the study.

Other research works have shown that the thickness of the buffer layer is critical to the enhancement of the photovoltaic properties of PSCs (C. Chen *et al.*, 2017). PDINN was optimized by varying its concentration in ethanol as shown in Table 5.5. It is notable from Table 5.5 and Figure 5.31 that the PCE of the device increased with an increase in PDINN concentration up to 1.0 mg mL^{-1} . The increase in performance is related to the proper ohmic contact created by the optimal PDINN thickness; this enables efficient charge movement between the ETL and the counter electrode. Further increase of PDINN was detrimental to the performance as thick PDINN could have created a larger distance for electrons to travel before reaching the contact, charges in Sn-PSCs have reduced diffusion lengths (T. Wu *et al.*, 2021) and thus very thick layers are not appropriate for high performing devices.

Table 5.5. Optimization of PDINN concentration

concentration	V_{OC} [V]	J_{SC} [mA cm^{-2}]	FF [%]	PCE [%]
w/o	0.61	18.78	57.11	6.52
0.3 mg mL^{-1}	0.65	19.89	59.52	7.68
0.5 mg mL^{-1}	0.65	20.77	66.58	9.02
1.0 mg mL^{-1}	0.69	21.22	68.85	10.06
1.5 mg mL^{-1}	0.67	20.16	68.34	9.19

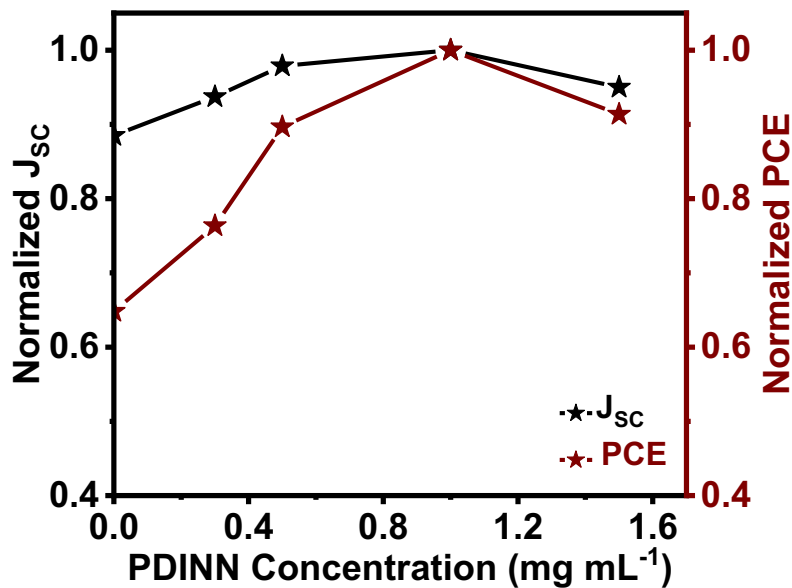


Figure 5.30. The variation of the photovoltaic properties of the devices with PDINN concentration.

5.3.3 Structural Defects within the Perovskite Absorber Layer

The difference in absorbance of the perovskite films deposited on treated and untreated PEDOT:PSS (Figure 30(b)) led to a conclusion that pristine PEDOT:PSS could be inducing structural defects to the absorber layer. The structural defects lead to poor-quality perovskite films,

which have reduced light absorption ability. The structural defect of the deposited perovskite in each case was evaluated by calculating their Urbach energy (E_u) using $\alpha = \alpha_0 \exp\left(\frac{h\nu - E_g}{E_u}\right)$ and the UV-Vis absorbance data as displayed in Figure 30(b).

E_u was obtained from the reciprocal of the slope of the curve of logarithmic absorbance against the absorbed photon energy as shown in Figure 5.32. The values of E_u are 95 and 83 meV for perovskite films deposited on control and KSCN-treated PEDOT:PSS. The increased E_u for the pristine PEDOT:PSS shows increased defect density in the perovskite film (S. Wang *et al.*, 2023). This implies that the pristine PEDOT:PSS contributes to the excessive defect density that is always observed in Sn-PSCs. The defects contribute to charge nonradiative recombination centers, which are exhibited in the reduced efficiency of control devices under PCE measurements. Therefore, it is necessary to eliminate the HTL defects using a suitable surface passivator before depositing the perovskite film.

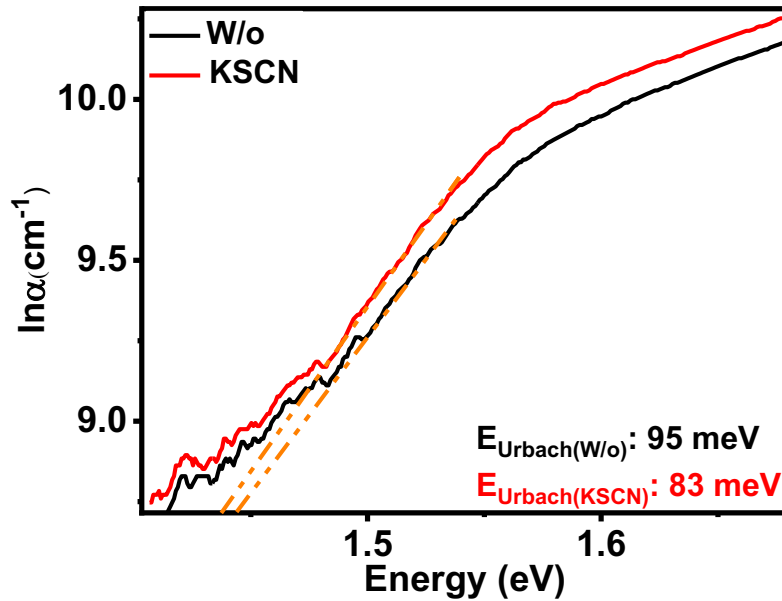


Figure 5.31. The Urbach energy of the perovskite film is based on the UV-Vis absorbance data.

5.3.4 Charge recombination within the Sn-perovskite solar cells

The charge recombination study was done using the electrochemical impedance spectroscopy technique and other characterization methods. Figure 33(a) displays the Nyquist plots of pristine, BCP, and PDINN based solar cells. The EIS measurement was done in the dark at a bias voltage, of 0.6 V for all the devices. The EIS data were fitted using ABC EIS analyzer (Bondarenko & Ragoisha, 2005) using the inset (in Figure 5.33(a)) equivalent circuit. Where R1, R2, and C1 are the series resistance, shunt (recombination) resistance, and capacitance of the solar cells. The values of R1, R2, and C1 were extracted from the fitting and tabulated as shown in Table 5.6; the percentage error during the fitting process was limited to below 10%. The series resistance of the devices with buffer layer was low with PDINN solar cells showing the lowest R1; the reduced series resistance of PDINN devices is attributed to its ability to form hydrogen bonding with PCBM and thus increase the ohmic contact between the ETL and the counter electrode. The reduced series resistance in the PDINN device is also evident in the $J - V$ characterization, where PDINN showed the highest J_{SC} . The recombination resistance, which is represented, by the major observable semicircular part of Figure 33(a) reveals that PDINN devices showed the highest value, which shows the reduced charge accumulation and recombination at the ETL/Cu interface (H. Jiang *et al.*, 2018). The reduced charge recombination can help in elevating the V_{OC} of the devices as shown under J-V measurement, and also as revealed by other researchers (G. Liu *et al.*, 2020). The time of surface recombination (τ_{rec}) of the devices was calculated using, $\tau_{rec} = R1C1$ and the result tabulated in Table 5.6. The PDINN device showed lowed τ_{rec} which confirms its ability to reduce the charge accumulation and recombination better than the commonly used BCP.

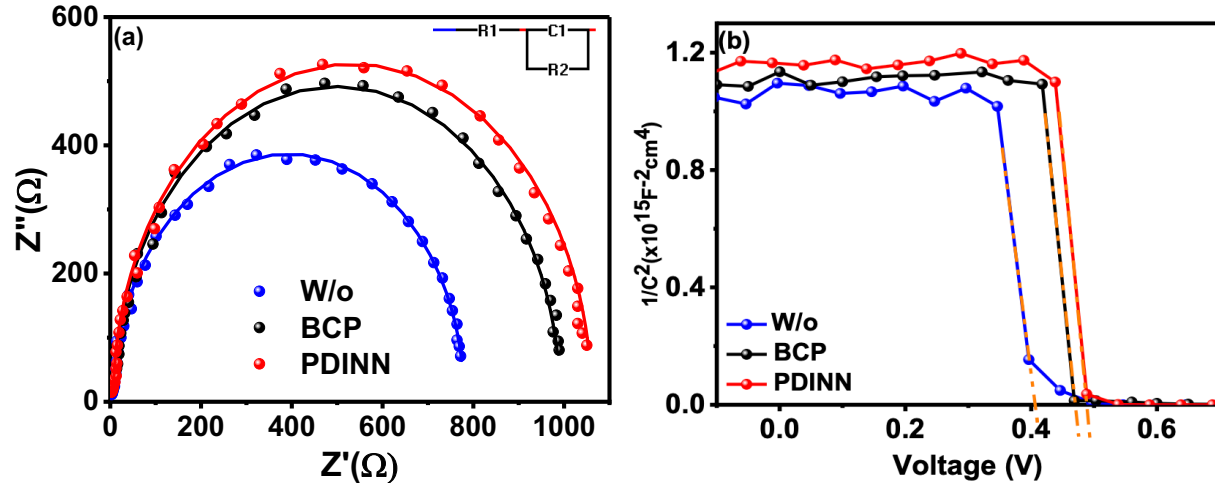


Figure 5.32. (a) The Nyquist plot from the EIS measurement for control, BCP, and PDINN devices. (b) Mott-Schottky plots of the devices measured at 100 kHz in the dark.

Table 5.6. Electrical impedance spectra parameters obtained after the Nyquist plot fitting.

	W/o	BCP	PDINN
Series Resistance (R_1) (Ω)	7.83	7.21	6.47
Recombination Resistance (R_2) (Ω)	669.43	983.61	1054.10
Capacitance (C_1) (F)	4.16×10^{-8}	2.43×10^{-8}	2.41×10^{-8}
τ_{rec} (μ s)	0.33	0.17	0.16

The Mott-Schottky plot in Figure 5.33(b) was used to further explain the enhancement in the performance of PDINN solar cells as compared to the BCP or control devices. The built-in potential (V_{bi}) was determined by extrapolating the 'almost vertical' linear part of the Mott-Schottky curve to the X-axis, and the value read at the intersection of the two lines. The built-in potentials are 0.41 V, 0.47 V, and 0.49 V for the control, BCP, and PDINN devices. The improved V_{bi} of PDINN devices is a result of reduced charge accumulation in the device due to the increased driving force of the photogenerated carriers, which leads to improved V_{OC} of PSCs (C. Wang et al., 2020).

The M-S plot in Figure 5.33(b) was used to determine the effects of using the two buffer layers on the defect concentration in the device. The slope of the linear part of the M-S plot and the equation

$\frac{A^2}{C^2} = \frac{2}{q\epsilon_r\epsilon_0 N_D} (V_{bi} - V)$, which was simplified to, $slope = \frac{2}{\epsilon\epsilon_0 A^2 e N_D}$, was used. The calculated defect concentrations of the three devices are 2.27×10^{16} , 1.86×10^{16} , and $1.84 \times 10^{16} \text{ cm}^{-3}$ for the control, BCP, and PDINN-based devices; these values are acceptable according to previously obtained values (Almora *et al.*, 2016; S. J. Lee *et al.*, 2018). In this study, it is assumed that the defect concentration should be similar since the perovskite and other layers, except the buffer layer, were made under the same conditions. With this assumption, it can be concluded that some defects within PSCs originated from the ETL/cathode junction, and thus, can be passivated by using the buffer layer. PDINN exhibited the lowest defect concentration, which can be due to its better conductivity, which allows for efficient charge transfer to the cathode.

Light dependent V_{OC} and J_{SC} were measured and plotted as shown in Figure 5.34(a and b), to promote the understanding of recombination mechanisms in the solar cells. The measurement was done on the champion devices with the optimized conditions. The graphs and $V_{OC} = \frac{nkT}{q} \ln\left(\frac{J_{SC}}{J_0} + 1\right)$ were used to determine the recombination mechanism as explained under theoretical background. The slope deviation of Figure 5.34(a) from kT/q is interrelated with trap-assisted recombination in the solar cells. The pristine device, BCP, and PDINN devices showed a slope of $1.14 kT/q$, $1.20 kT/q$, and $1.50 kT/q$, respectively. The smallest slope of PDINN devices shows reduced energy loss due to trap-assisted recombination, compared to BCP and control devices (Ji *et al.*, 2022; B. Yu *et al.*, 2021). These results show the ability of PDINN to suppress trap-recombination centers in Sn-PSCs and can help in explaining the improvement of PCE in PDINN devices.

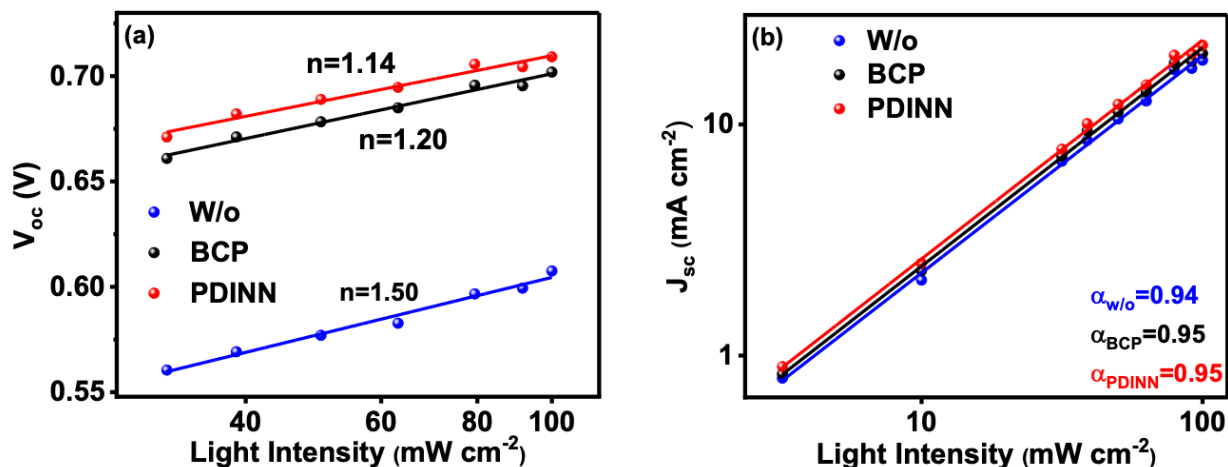


Figure 5.33. (a) The linear relationship of V_{oc} against logarithmic light intensity. (b) Double logarithmic of J_{sc} against light intensity.

The bimolecular recombination in the devices was investigated using Figure 5.34(b), where the slopes of the curves were considered. The slopes of the curves were 0.94, 0.95, and 0.95 for control, BCP, and PDINN devices, respectively. Values of the slope of Figure 34(b) close or equivalent to 1 show no/reduced bimolecular recombination in the device (Su *et al.*, 2022). Bimolecular recombination is sometimes referred to as radiative recombination, and it originates from the interfaces within the solar cell (M. Kim *et al.*, 2019). One of the interfaces is at the ETL/electrode boundary, and since all the other layers of the PSCs are similar, it can be assumed that the bimolecular recombination difference originated from the ETL/with or without buffer layer/Cu interface. The reduced radiative recombination in PDINN devices shows that PDINN can help in providing a directed pathway of electrons from the ETL to the Cu electrode, and hence the increased performance.

Dark current measurement was done to determine the leakage current in each case and to further understand why PDINN is better than the commonly used BCP. The dark current values of the devices were read from a bias voltage of -0.5 V as shown in Figure 5.35(a). The values of the dark currents are 3.55×10^{-4} , 5.60×10^{-5} , and 4.24×10^{-5} mA cm^{-2} for pristine, BCP, and PDINN devices, correspondingly. The high current leakage observed in the control device is associated with charge accumulation at the ETL/Cu interlayer, while the low leakage of the PDINN device is because of reduced charge accumulation at the ETL/Cu due to the PDINN buffer layer. The PDINN

can form a better ohmic contact between the ETL and Cu, also, PDINN has high electron conductivity making it easy for electron flow. BCP has a reduced dark current, which is higher than PDINN solar cells because it does not have some of the vital amine group responsible for the formation of strong interaction with PCBM and the cathode, also, its energy level does not perfectly match that of PCBM making it difficult for the flow of electrons.

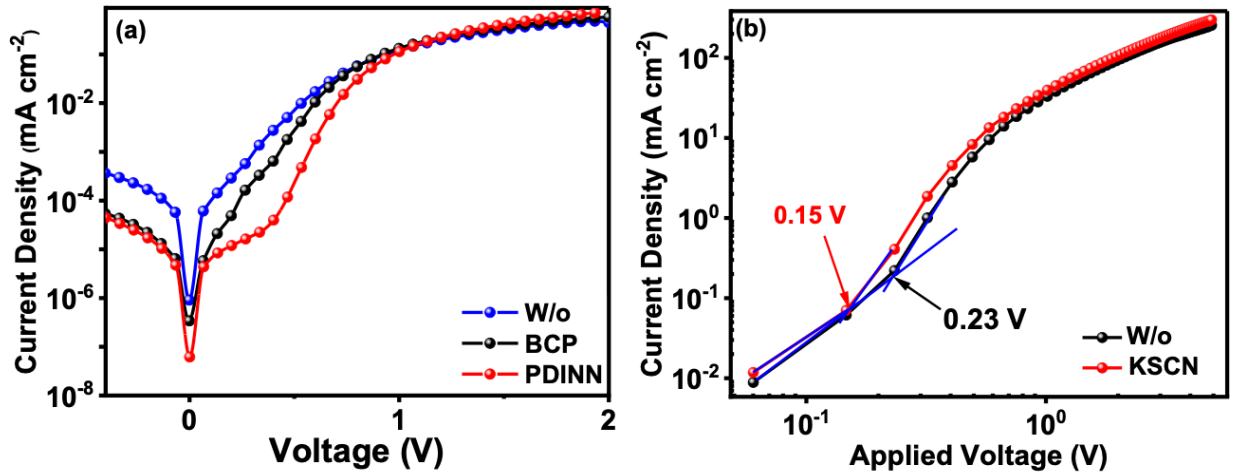


Figure 5.34. (a) Dark current graphs of the devices measured under dark condition (b) SCLC plots of hole-only devices with ITO/PEDOT:PSS/with or without KSCN/perovskite/MoO₃/Cu.

It is already clear that the performance of our devices improved remarkably when KSCN was used as an interlayer at PEDOT:PSS/perovskite interlayer. Therefore, hole-only devices with architecture ITO/PEDOT:PSS/with or without KSCN/perovskite/MoO₃/Cu were constructed to comprehend the impacts of KSCN on the defects within the Sn-PSCs. The space charge limited current plots of the hole-only device dark current measurement is shown in Figure 5.35(b). The trap concentration in the two devices was evaluated using $N_t = 2V_{TFL} \frac{\epsilon_r \epsilon_0}{qL^2}$, where all parameters are as defined before, under theoretical background. The V_{TFL} of the pristine solar cells is 0.23 V and that of KSCN based device is 0.15 V. The defect densities of the devices were calculated and the values are 7.63×10^{15} and $4.98 \times 10^{15} \text{ cm}^{-3}$ for the control and KSCN devices. The increased defect density in devices without KSCN can help explain the low efficiency of devices made by depositing perovskite directly on the PEDOT:PSS; it shows that PEDOT:PSS can directly contribute to defects within the PSCs and thus lead to charge recombination losses and low device

performance. The hole mobility of the perovskite layer was calculated from the SCLC region using the Mott-Gurney equation, $\mu_h = \frac{8JL^3}{9V^2 \epsilon_r \epsilon_0}$. The hole mobility of the perovskite deposited on pure PEDOT:PSS was $1.29 \times 10^{-2} \text{ cm}^2 \text{ V}^{-1} \text{ s}^{-1}$ and of that of perovskite deposited on KSCN treated PEDOT:PSS was $1.30 \times 10^{-2} \text{ cm}^2 \text{ V}^{-1} \text{ s}^{-1}$. The observed high hole mobility could be as a result of deposition of almost defect free perovskite films (J. J. Cao *et al.*, 2022).

5.3.5 The photogenerated charge transport in the BCP and PDINN based Sn-PSCs

From the photovoltaic performance of the devices exhibited in Figure 5.26(b) it was shown that, the hysteresis of PDINN based solar cell was the lowest as compared to other devices. Hysteresis in PSCs results from charge accumulation at the perovskite/contact interface induced by iodine/ion migration (Q. Jiang *et al.*, 2016). Therefore, a cathode interfacial layer with faster charge extraction is essential to decrease charge accumulation and hysteresis losses in Sn-perovskite solar cells.

Transient photocurrent and photovoltage decay measurements were done to evaluate the charge extraction abilities of PDINN and BCP as shown in Figure 5.36. In Figure 5.36(a), the photovoltage decay also known as charge recombination time was increased to 65.61 μs from 18.73 μs when the commonly used BCP cathode layer was replaced with PDINN. The photocurrent decay which, can also be referred to as charge transport time, significantly reduced to 1.23 μs from 1.55 μs when BCP was replaced by PDINN. The increase and decrease in photovoltage and photocurrent, respectively, decay in PDINN-based solar cells shows that PDINN is a better electron extractor and thus charge accumulation and recombination at the ETL/cathode will significantly be reduced (Q. Jiang *et al.*, 2016; Majhi *et al.*, 2023). The reduced charge accumulation best explains the reduced hysteresis in PDNN devices.

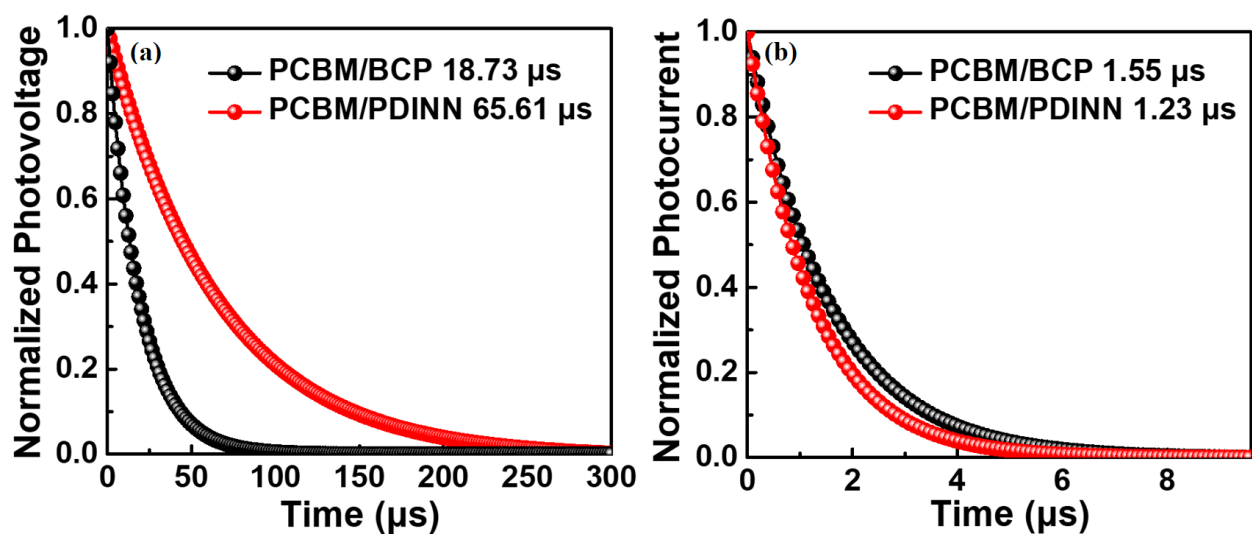


Figure 5.35. (a) Transient photovoltage curves (b) Transient photocurrent curves of Sn-perovskite solar cells based on BCP and PDINN cathode interfacial layer.

5.3.6 Investigation of moisture and oxygen stability of Sn-perovskite solar cells.

Perovskite materials, especially Sn-perovskites are known for their poor stability in different conditions. Some of the conditions include, ambient atmosphere, UV-light, and elevated temperatures beyond room temperature (Chowdhury *et al.*, 2023). In Sn-perovskite moisture and oxygen ingress is a major cause of extrinsic source of Sn-perovskite materials and solar cells degradation. The moisture and oxygen can attack the perovskite both at fabrication point and during operation of the full device. Therefore, it is necessary to fabricate a moisture and oxygen resistant Sn-perovskite solar cells if their stability is to be improved.

Figure 5.37 shows the photographs of Sn-perovskite solar cells based on PDINN and BCP after exposure to air, the photographs were taken at intervals of 2 hours to determine their ambient stability. As time progressed the perovskite devices, solution-processed layers, turned from dark brown to yellow brown, with the BCP based devices changing their colour at a faster rate. In addition, the colour of the copper cathode transformed from red-orange to reddish-brown, the colour change in BCP case was faster as compared to the PDINN case. The colour change in the Sn-perovskite devices is related to the decomposition of the Sn-perovskite film due to exposure to ambient atmosphere.

Upon exposure to air, ASnX_3 interacts with O_2 and H_2O to produce by-products. Some of the by-products include SnO_2 , A_2SnI_6 and I_2 (Lanzetta *et al.*, 2021). I_2 formation results from the oxidation of I^- , and the I_2 is responsible for further and severe device degradation (Y. Xing *et al.*, 2023). The oxidation of I^- produces increased p-doping in the perovskite layer and finally leads to perovskite solar cell short-circuiting or failure. The colour change of the cathode is due to the volatile I^- which easily diffuses from the perovskite layer and corrodes the electrode leading to creation of CuI_2 (Wijesekara *et al.*, 2021; Y. Xing *et al.*, 2023; W. S. Yang *et al.*, 2017). The ability of PDINN to resist corrosion of both the perovskite and electrode layers for a longer time is beneficial to the long term stability of Sn-PSCs.

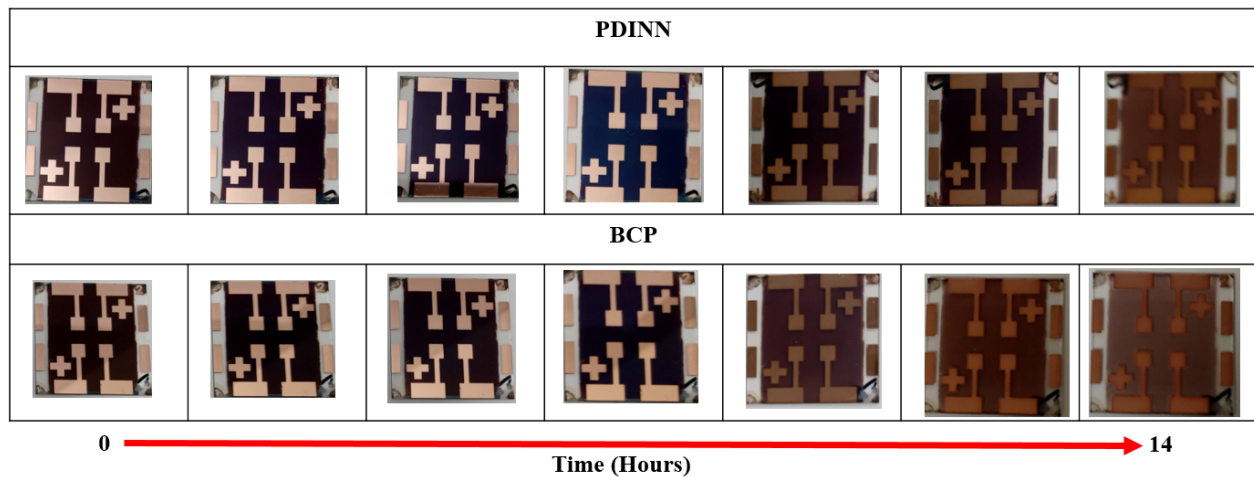


Figure 5.36. Photo-stability of Sn-PSCs with PDINN and BCP interlayer taken at intervals of 2 hours after exposure to ambient air for 14 hours. (The relative humidity was $\sim 38.8 - 44.3\%$, and temperature $\sim 18.3 - 20^\circ\text{C}$).

From chapter 2 of this work, under the degradation mechanism of Sn-perovskite, it was established that moisture accelerates the degradation of Sn-perovskite. Therefore, the difference in the rate of degradation witnessed in Figure 5.37 was examined by determining the water contact angle of PCBM, PCBM/BCP and PCBM/PDINN as shown in Figure 5.38. From Figure 5.38(b) it is clear that BCP turns the surface of PCBM to hygroscopic status making it easily attacked by the atmospheric water; this only aids in moisture infiltration into the perovskite layer. However, in Figure 5.38(c), PDINN makes the PCBM more hydrophobic as it can be seen that it amplified the water contact angle from 82.5° to 85.4° . The hydrophobic nature of PDINN can help in repelling

moisture from attacking the perovskite device, thus increasing the device stability. This result can help in explaining the observed enhanced stability of PDINN-based solar cells in Figure 5.28(b).

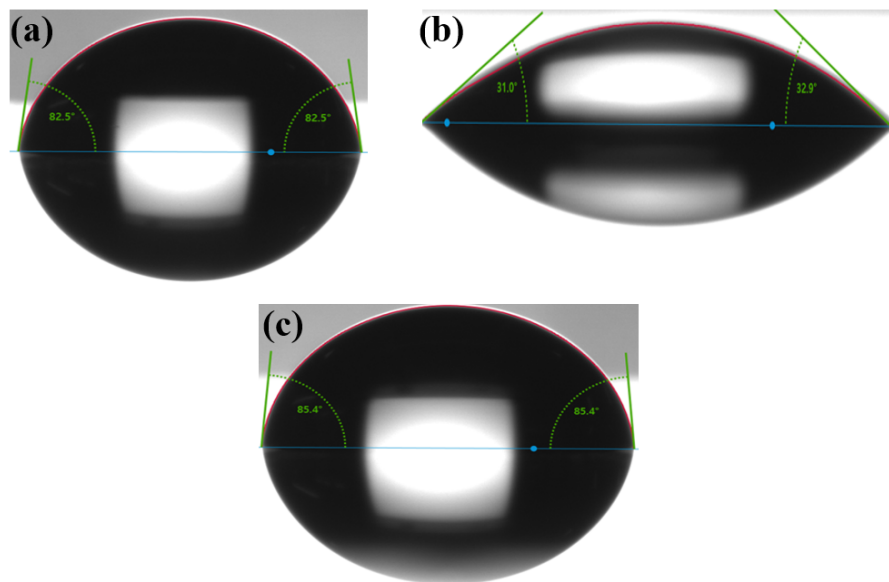


Figure 5.37. Water contact angle of (a) PCBM, (b) PCBM/BCP and (c) PCBM/PDINN.

CHAPTER SIX

CONCLUSIONS AND RECOMMENDATIONS

6.1 Conclusions

In most research work on Sn-PSCs, SnF₂ has always been used as an antioxidant to impede the oxidation of Sn²⁺. In this work, SnF₂ was employed as our main antioxidant; however, it resulted in the creation of aggregate phases on the resulting perovskite film. The aggregates are harmful to the qualities of the film such as charge transport and thus not suitable for solar cell fabrication. Anilinium hypophosphite (AHP) was used as a supplement additive to annihilate the unwanted phases created by using SnF₂. When the mixture of SnF₂ and AHP was used in FA_{0.50}MA_{0.45}PEA_{0.05}SnI_{3.00} and FASnI₃ films, the structural properties and crystallinity as verified by XRD measurement were improved. The morphology according to SEM data was enhanced; the morphology of the film with only SnF₂ was rough with pinholes and aggregates, however upon the addition of AHP, the film became compact, with no pinholes and no phase aggregation. The charge dynamics of the films improved when both AHP additives were combined, according to PL and TRPL measurements. The PL intensity increased when AHP was incorporated into the precursor solution symbolizing the reduction of charge non-radiative recombination in the perovskite films. Thus, the use of an optimized AHP additive quantity was shown to improve the quality of Sn-perovskite films.

The FA_{0.50}MA_{0.45}PEA_{0.05}SnI_{3.00} and FASnI₃ films based on optimized conditions were used to fabricate Sn-PSCs. The reference solar cell was based on SnF₂ and their PCE was compared to solar cells based on AHP additive. The PCE of FA_{0.50}MA_{0.45}PEA_{0.05}SnI_{3.00}-based solar cells improved to 6.87% higher than the control, which was only 4.74%. The PCE of FASnI₃-based solar cells improved to 5.48% from 4.04% when AHP additive was used. The rise in PCEs of the devices was due to improved Sn-perovskite absorber quality due to the use of AHP. Therefore, improving the quality of the Sn-perovskite layer is essential in improving the PCEs of Sn-PSCs.

PDINN is not thickness sensitive as compared to BCP, which is normally used as the cathode interfacial layer in Sn-PSCs. This allows room for PDINN thickness variation on PCBM without affecting the J_{sc} and PCE of the devices. PDINN and BCP are mostly solutions processed, and due to errors arising from uncontrollable solvent evaporation, it may not be easy to fix their thickness

to the optimal value required for high-performing devices. Therefore, it is much easier to use PDINN in fabricating devices because small thickness variation resulting from changes in the precursor solution does not affect the performance of devices. The performance of PDINN-based devices was 10.99%, which was higher than 10.79% for BCP devices. The high performance of PDINN devices was due to their good charge transport properties as revealed from the TPC and TPV results; which led to ease of flow of electrons from PCBM to Cu. The other characterization such as EIS measurement showed that PDINN devices had reduced series resistance, which led to increased charge collection at the cathode.

The stability of the FASnI_3 and $\text{FA}_{0.50}\text{MA}_{0.45}\text{PEA}_{0.05}\text{SnI}_3$ -based devices was investigated and it was found that the AHP-based devices were more stable than the SnF_2 -only devices. According to FTIR, SEM, and SEM-EDS data it was revealed that SnF_2 and AHP interaction resulted in a complex compound salt, $\text{Sn}(\text{H}_2\text{PO}_2)_2 \cdot \text{SnF}_2$ which positions itself at the grain boundaries and on the surface of the perovskite films. Due to the hydrophobic nature of AHP, it can thwart moisture from penetrating the perovskite hence making the perovskite stable and by extension making the solar cells more stable than the control ones. The stability of the devices based on BCP and PDINN buffer layer was investigated; PDINN showed better storage stability after 30 days. PDINN devices only lost 20% of their optimal performance and BCP devices lost up to 46% of their optimal performance. The good PDINN-based devices stability was due to its hydrophobic nature witnessed from the water contact measurement.

6.2 Recommendations for Further Works

Low V_{OC} is still a hurdle in achieving high-performing Sn-PSCs. In this study, the best V_{OC} is 0.71 V which shows that the V_{OC} loss according to $V_{OCloss} = \frac{E_g}{q} - V_{OC}$ is still 50%. The high V_{OC} loss is contributed primarily by the high defect concentration of Sn-perovskites. Therefore, further research needs to be carried out to establish the right antioxidant to “fully” eradicate the defects contributing to V_{OC} loss. Eliminating the defects “completely” will also help in boosting the fill factor of the devices. The J_{SC} of Sn-PSCs can still be improved further. Looking at the EQE spectra in this study, all of the curves experienced a drop in light absorption between 730 – 1000 nm wavelengths; this trend is similar to results obtained by other research groups. More research can be conducted to boost the absorbance of Sn-perovskite in this region to boost the J_{SC} for better PCEs.

REFERENCES

- Açikel, S. M., Celik, C., Gürbüz, D., & Cinarli, A. (2018). Flame retardant effect of tri butyl phosphate (TBP) in vegetable tanned leathers. *Tekstil ve Konfeksiyon*, **28**(2), 135–140.
- Ahmed, M. T., Islam, S., & Ahmed, F. (2022). Comparative Study on the Crystallite Size and Bandgap of Perovskite by Diverse Methods. *Advances in Condensed Matter Physics*, **2022**, 9535932
- Alharbi, E. A., Alyamani, A. Y., Kubicki, D. J., Uhl, A. R., Walder, B. J., Alanazi, A. Q., Luo, J., Burgos-Caminal, A., Albadri, A., Albrithen, H., Alotaibi, M. H., Moser, J. E., Zakeeruddin, S. M., Giordano, F., Emsley, L., & Grätzel, M. (2019). Atomic-level passivation mechanism of ammonium salts enabling highly efficient perovskite solar cells. *Nature Communications*, **10**(1), 3008.
- Alidaei, M., Izadifard, M., Ghazi, M. E., Roghabadi, F. A., & Ahmadi, V. (2019). Interfacial defect passivation in $\text{CH}_3\text{NH}_3\text{PbI}_3$ perovskite solar cells using modifying of hole transport layer. *Journal of Materials Science: Materials in Electronics*, **30**(7), 6936–6946.
- Almora, O., Aranda, C., Mas-Marzá, E., & Garcia-Belmonte, G. (2016). On Mott-Schottky analysis interpretation of capacitance measurements in organometal perovskite solar cells. *Applied Physics Letters*, **109**, 173903.
- Asgary, S., Moghaddam, H. M., Bahari, A., & Mohammadpour, R. (2021). Role of BCP layer on nonlinear properties of perovskite solar cell. *Solar Energy*, **213**(2021), 383–391.
- Babayigit, A., Duy Thanh, D., Ethirajan, A., Manca, J., Muller, M., Boyen, H. G., & Conings, B. (2016). Assessing the toxicity of Pb- and Sn-based perovskite solar cells in model organism *Danio rerio*. *Scientific Reports*, **6**, 18721.
- Bandara, R. M. I., Jayawardena, K. D. G. I., Adeyemo, S. O., Hinder, S. J., Smith, J. A., Thirimanne, H. M., Wong, N. C., Amin, F. M., Freestone, B. G., Parnell, A. J., Lidzey, D. G., Joyce, H. J., Sporea, R. A., & Silva, S. R. P. (2019). Tin (iv) dopant removal through anti-solvent engineering enabling tin based perovskite solar cells with high charge carrier mobilities. *Journal of Materials Chemistry C*, **7**(27), 8389–8397.
- Bi, D., Yi, C., Luo, J., Décoppet, J. D., Zhang, F., Zakeeruddin, S. M., Li, X., Hagfeldt, A., & Grätzel, M. (2016). Polymer-templated nucleation and crystal growth of perovskite films for solar cells with efficiency greater than 21%. *Nature Energy*, **1**(10), 16142.
- Boyd, M. T., Klein, S. A., Reindl, D. T., & Dougherty, B. P. (2011). Evaluation and validation of equivalent circuit photovoltaic solar cell performance models. *Journal of Solar Energy Engineering, Transactions of the ASME*, **133**(2), 021005.
- Burschka, J., Pellet, N., Moon, S. J., Humphry-Baker, R., Gao, P., Nazeeruddin, M. K., & Grätzel, M. (2013). Sequential deposition as a route to high-performance perovskite-sensitized solar cells. *Nature*, **499**(7458), 316–319.

- Cao, D. H., Stoumpos, C. C., Yokoyama, T., Logsdon, J. L., Song, T. Bin, Farha, O. K., Wasielewski, M. R., Hupp, J. T., & Kanatzidis, M. G. (2017). Thin Films and Solar Cells Based on Semiconducting Two-Dimensional Ruddlesden-Popper $(\text{CH}_3(\text{CH}_2)_3\text{NH}_3)_2(\text{CH}_3\text{NH}_3)_{n-1}\text{Sn}_n\text{I}_{3n+1}$ Perovskites. *ACS Energy Letters*, **2**(5), 982–990.
- Cao, J. J., Lou, Y. H., Yang, W. F., Wang, K. L., Su, Z. H., Chen, J., Chen, C. H., Dong, C., Gao, X. Y., & Wang, Z. K. (2022). Multifunctional potassium thiocyanate interlayer for eco-friendly tin perovskite indoor and outdoor photovoltaics. *Chemical Engineering Journal*, **433**, 133832.
- Cao, J., & Yan, F. (2021). Recent progress in tin-based perovskite solar cells. *Energy and Environmental Science*, **14**(3), 1286–1325.
- Cao, J., Tai, Q., You, P., Tang, G., Wang, T., Wang, N., & Yan, F. (2019). Enhanced performance of tin-based perovskite solar cells induced by an ammonium hypophosphite additive. *Journal of Materials Chemistry A*, **7**(46), 26580–26585.
- Chen, B., Yang, M., Priya, S., & Zhu, K. (2016). Origin of J-V Hysteresis in Perovskite Solar Cells. *Journal of Physical Chemistry Letters*, **7**(5), 905–917.
- Chen, C., Zhang, S., Wu, S., Zhang, W., Zhu, H., Xiong, Z., Zhang, Y., & Chen, W. (2017). Effect of BCP buffer layer on eliminating charge accumulation for high performance of inverted perovskite solar cells. *RSC Advances*, **7**(57), 35819–35826.
- Chen, J., Zhao, X., Kim, S. G., & Park, N. G. (2019). Multifunctional Chemical Linker Imidazoleacetic Acid Hydrochloride for 21% Efficient and Stable Planar Perovskite Solar Cells. *Advanced Materials*, **31**, 1902902.
- Chen, Y. F., Luo, Z. M., Chiang, C. H., & Wu, C. G. (2022). Multifunctional Ionic Fullerene Additive for Synergistic Boundary and Defect Healing of Tin Perovskite to Achieve High-Efficiency Solar Cells. *ACS Applied Materials and Interfaces*, **14**(41), 46603–46614.
- Chen, Y., Wang, K., Qi, H., Zhang, Y., Wang, T., Tong, Y., & Wang, H. (2022). Mitigating VocLoss in Tin Perovskite Solar Cells via Simultaneous Suppression of Bulk and Interface Nonradiative Recombination. *ACS Applied Materials and Interfaces*, **14**, 41086–41094.
- Chowdhury, T. A., Bin Zafar, M. A., Sajjad-Ul Islam, M., Shahinuzzaman, M., Islam, M. A., & Khandaker, M. U. (2023). Stability of perovskite solar cells: issues and prospects. *RSC Advances* **13**(3), 1787–1810.
- Cui, D., Liu, X., Wu, T., Lin, X., Luo, X., Wu, Y., Segawa, H., Yang, X., Zhang, Y., Wang, Y., & Han, L. (2021). Making Room for Growing Oriented FASnI_3 with Large Grains via Cold Precursor Solution. *Advanced Functional Materials*, **31**(25), 2100931.
- Duan, C., Li, J., Liu, Z., Wen, Q., Tang, H., & Yan, K. (2021). Highly electroluminescent and stable inorganic CsPbI_2Br perovskite solar cell enabled by balanced charge transfer. *Chemical Engineering Journal*, **417**(2021), 128053.

- Efaz1, E. T., Rhaman, M. M., Al Imam, S., Bashar, K. L., Kabir, F., Mourtaza, M. E., Sakib, S. N., & Mozahid, F. A. (2021). A review of primary technologies of thin-film solar cells. *Engineering Research Express*, **3**(3), 032001.
- Fan, Q., Biesold-McGee, G. V., Ma, J., Xu, Q., Pan, S., Peng, J., & Lin, Z. (2020). Lead-Free Halide Perovskite Nanocrystals: Crystal Structures, Synthesis, Stabilities, and Optical Properties. *Angewandte Chemie - International Edition*, **59**(3), 1030–1046.
- Faridi, A. W., Imran, M., Tariq, G. H., Ullah, S., Noor, S. F., Ansar, S., & Sher, F. (2022). Synthesis and Characterization of High-Efficiency Halide Perovskite Nanomaterials for Light-Absorbing Applications. *Industrial and Engineering Chemistry Research*, **62**(11), 4494–4502.
- Fu, Q., Tang, X., Huang, B., Hu, T., Tan, L., Chen, L., & Chen, Y. (2018). Recent Progress on the Long-Term Stability of Perovskite Solar Cells. *Advanced Science*, **5**(5), 1700387.
- Gao, F., Li, C., Qin, L., Zhu, L., Huang, X., Liu, H., Liang, L., Hou, Y., Lou, Z., Hu, Y., & Teng, F. (2018). Enhanced performance of tin halide perovskite solar cell by addition of lead thiocyanate. *RSC Advances*, **8**(25), 14025–14030.
- Giordano, F., Abate, A., Correa Baena, J. P., Saliba, M., Matsui, T., Im, S. H., Zakeeruddin, S. M., Nazeeruddin, M. K., Hagfeldt, A., & Graetzel, M. (2016). Enhanced electronic properties in mesoporous TiO₂ via lithium doping for high-efficiency perovskite solar cells. *Nature Communications*, **7**(10379).
- Girolamo, D. Di, Pascual, J., Aldamasy, M. H., Iqbal, Z., Li, G., Radicchi, E., Li, M., Nasti, G., Dallmann, A., Angelis, F. De, & Abate, A. (2021). Solvents for Processing Stable Tin Halide. *ACS Energy Letters* **6**(3), 959–968.
- Guo, Z., Jena, A. K., Kim, G. M., & Miyasaka, T. (2022). The high open-circuit voltage of perovskite solar cells. *Energy and Environmental Science*, **15**(8), 3171–3222.
- Hao, F., Stoumpos, C. C., Cao, D. H., Chang, R. P. H., & Kanatzidis, M. G. (2014). Lead-free solid-state organic-inorganic halide perovskite solar cells. *Nature Photonics*, **8**(6), 489–494.
- Hao, F., Stoumpos, C. C., Guo, P., Zhou, N., Marks, T. J., Chang, R. P. H., & Kanatzidis, M. G. (2015). Solvent-Mediated Crystallization of CH₃NH₃SnI₃ Films for Heterojunction Depleted Perovskite Solar Cells. *Journal of the American Chemical Society*, **137**(35), 11445–11452.
- Hassaniien, A. S., & Akl, A. A. (2016). Effect of Se addition on optical and electrical properties of chalcogenide CdSSe thin films. *Superlattices and Microstructures*, **89**, 153–169.
- He, X., Wu, T., Liu, X., Wang, Y., Meng, X., Wu, J., Noda, T., Yang, X., Moritomo, Y., Segawa, H., & Han, L. (2020). Highly efficient tin perovskite solar cells achieved in a wide oxygen concentration range. *Journal of Materials Chemistry A*, **8**(5), 2760–2768.
- Hoefler, S. F., Trimmel, G., & Rath, T. (2017). Progress on lead-free metal halide perovskites for photovoltaic applications: a review. *Monatshefte Fur Chemie*, **148**(5), 795–826.

- Igbari, F., Wang, Z. K., & Liao, L. S. (2019). Progress of Lead-Free Halide Double Perovskites. In *Advanced Energy Materials*, **9**(12), 1803150.
- Im, J. H., Jang, I. H., Pellet, N., Grätzel, M., & Park, N. G. (2014). Growth of $\text{CH}_3\text{NH}_3\text{PbI}_3$ cuboids with controlled size for high-efficiency perovskite solar cells. *Nature Nanotechnology*, **9**(11), 927–932.
- Im, J. H., Lee, C. R., Lee, J. W., Park, S. W., & Park, N. G. (2011). 6.5% Efficient Perovskite Quantum-Dot-Sensitized Solar Cell. *Nanoscale*, **3**(10), 4088–4093.
- International Energy Agency. (2021). *World Energy Outlook 2021 Technical note on the emissions and temperature implications of COP26 pledges*. www.iea.org/t&c/
- Jahandar, M., Khan, N., Jahankhan, M., Song, C. E., Lee, H. K., Lee, S. K., Shin, W. S., Lee, J. C., Im, S. H., & Moon, S. J. (2019). High-performance $\text{CH}_3\text{NH}_3\text{PbI}_3$ inverted planar perovskite solar cells via ammonium halide additives. *Journal of Industrial and Engineering Chemistry*, **80**, 265–272.
- Jain, A., Kumar, P., Jain, S. C., Kumar, V., Kaur, R., & Mehra, R. M. (2007). Trap filled limit voltage (VTFL) and V2 law in space charge limited currents. *Journal of Applied Physics*, **102**, 094505.
- Jeon, N. J., Noh, J. H., Kim, Y. C., Yang, W. S., Ryu, S., & Seok, S. Il. (2014). Solvent engineering for high-performance inorganic-organic hybrid perovskite solar cells. *Nature Materials*, **13**(9), 897–903.
- Ji, L., Zhang, T., Wang, Y., Liu, D., Chen, H., Zheng, H., Peng, X., Yuan, S., Chen, Z. D., & Li, S. (2022). Regulating crystallization dynamics and crystal orientation of methylammonium tin iodide enables high-efficiency lead-free perovskite solar cells. *Nanoscale*, **14**(4), 1219–1225.
- Jiang, H., Yan, Z., Zhao, H., Yuan, S., Yang, Z., Li, J., Liu, B., Niu, T., Feng, J., Wang, Q., Wang, D., Yang, H., Liu, Z., & Liu, S. F. (2018). Bifunctional Hydroxylamine Hydrochloride Incorporated Perovskite Films for Efficient and Stable Planar Perovskite Solar Cells. *ACS Applied Energy Materials*, **2018**(1), 900–909.
- Jiang, Q., Zhang, L., Wang, H., Yang, X., Meng, J., Liu, H., Yin, Z., Wu, J., Zhang, X., & You, J. (2016). Enhanced electron extraction using SnO_2 for high-efficiency planar-structure $\text{HC}(\text{NH}_2)_2\text{PbI}_3$ -based perovskite solar cells. *Nature Energy*, **2**, 16177.
- Jiang, Q., Zhao, Y., Zhang, X., Yang, X., Chen, Y., Chu, Z., Ye, Q., Li, X., Yin, Z., & You, J. (2019). Surface passivation of perovskite film for efficient solar cells. *Nature Photonics*, **13**(7), 460–466.
- Jiang, X., Li, H., Zhou, Q., Wei, Q., Wei, M., Jiang, L., Wang, Z., Peng, Z., Wang, F., Zang, Z., Xu, K., Hou, Y., Teale, S., Zhou, W., Si, R., Gao, X., Sargent, E. H., & Ning, Z. (2021). One-Step Synthesis of $\text{SnI}_2 \cdot (\text{DMSO})_x$ Adducts for High-Performance Tin Perovskite Solar Cells. *Journal of the American Chemical Society*, **143**(29), 10970–10976.
- Jiang, X., Wang, F., Wei, Q., Li, H., Shang, Y., Zhou, W., Wang, C., Cheng, P., Chen, Q., Chen, L., & Ning, Z. (2020). Ultra-high open-circuit voltage of tin perovskite solar cells via an electron transporting layer design. *Nature Communications*, **11**(1), 1245.

- Jiang, Y., Lu, Z., Zou, S., Lai, H., Zhang, Z., Luo, J., Huang, Y., He, R., Jin, J., Yi, Z., Luo, Y., Wang, W., Wang, C., Hao, X., Chen, C., Wang, X., Wang, Y., Ren, S., Shi, T., ... Zhao, D. (2022). Dual-site passivation of tin-related defects enabling efficient lead-free tin perovskite solar cells. *Nano Energy*, **103**, 107818.
- Jokar, E., Cheng, P. Y., Lin, C. Y., Narra, S., Shahbazi, S., & Diau, E. W. G. (2021). Enhanced performance and stability of 3D/2D tin perovskite solar cells fabricated with a sequential solution deposition. *ACS Energy Letters*, **6**, 485–492.
- Jokar, E., Chien, C. H., Fathi, A., Rameez, M., Chang, Y. H., & Diau, E. W. G. (2018). Slow surface passivation and crystal relaxation with additives to improve device performance and durability for tin-based perovskite solar cells. *Energy and Environmental Science*, **11**(9), 2353–2362.
- Jokar, E., Chien, C. H., Tsai, C. M., Fathi, A., & Diau, E. W. G. (2019). Robust Tin-Based Perovskite Solar Cells with Hybrid Organic Cations to Attain Efficiency Approaching 10%. *Advanced Materials*, **31**(2), 1804835.
- Jung, E. H., Jeon, N. J., Park, E. Y., Moon, C. S., Shin, T. J., Yang, T. Y., Noh, J. H., & Seo, J. (2019). Efficient, stable and scalable perovskite solar cells using poly(3-hexylthiophene). *Nature*, **567**(7749), 511–515.
- Jung, M., Ji, S. G., Kim, G., & Seok, S. Il. (2019). Perovskite precursor solution chemistry: From fundamentals to photovoltaic applications. *Chemical Society Reviews*, **48**(7), 2011–2038.
- Kaiser, C., Sandberg, O. J., Zarrabi, N., Li, W., Meredith, P., & Armin, A. (2021). A universal Urbach rule for disordered organic semiconductors. *Nature Communications*, **12**(1), 3988.
- Kamarudin, M. A., Hirotsu, D., Wang, Z., Hamada, K., Nishimura, K., Shen, Q., Toyoda, T., Iikubo, S., Minemoto, T., Yoshino, K., & Hayase, S. (2019). Suppression of charge carrier recombination in lead-free tin halide perovskite via lewis base post-treatment. *Journal of Physical Chemistry Letters*, **10**(17), 5277–5283.
- Kayesh, M. E., Chowdhury, T. H., Matsuishi, K., Kaneko, R., Kazaoui, S., Lee, J. J., Noda, T., & Islam, A. (2018). Enhanced Photovoltaic Performance of FASnI₃-Based Perovskite Solar Cells with Hydrazinium Chloride Coadditive. *ACS Energy Letters*, **3**(7), 1584–1589.
- Ke, W., & Kanatzidis, M. G. (2019). Prospects for low-toxicity lead-free perovskite solar cells. *Nature Communications*, **10**(1), 965.
- Ke, W., Stoumpos, C. C., & Kanatzidis, M. G. (2019). “Unleaded” Perovskites: Status Quo and Future Prospects of Tin-Based Perovskite Solar Cells. *Advanced Materials*, **31**(47), 1803230.
- Khan, N., Ryu, D. H., Park, J. G., Lee, H. K., Lee, S. K., Shin, W. S., Lee, J. C., Hong, K. H., Im, S. H., & Song, C. E. (2022). Bromide Incorporation Enhances Vertical Orientation of Triple Organic Cation Tin-Halide Perovskites for High-Performance Lead-Free Solar Cells. *Solar RRL*, **6**(11), 2200631.
- Kim, D., Lee, D. K., Kim, S. M., Park, W., & Sim, U. (2020). Photoelectrochemical water splitting reaction system based on metal-organic halide perovskites. *Materials*, **13**(210) .

- Kim, H. S., Lee, C. R., Im, J. H., Lee, K. B., Moehl, T., Marchioro, A., Moon, S. J., Humphry-Baker, R., Yum, J. H., Moser, J. E., Grätzel, M., & Park, N. G. (2012). Lead iodide perovskite sensitized all-solid-state submicron thin film mesoscopic solar cell with efficiency exceeding 9%. *Scientific Reports*, **2**, 591.
- Kim, M., Kim, G. H., Lee, T. K., Choi, I. W., Choi, H. W., Jo, Y., Yoon, Y. J., Kim, J. W., Lee, J., Huh, D., Lee, H., Kwak, S. K., Kim, J. Y., & Kim, D. S. (2019). Methylammonium Chloride Induces Intermediate Phase Stabilization for Efficient Perovskite Solar Cells. *Joule*, **3**(9), 2179–2192.
- Kojima, A., Teshima, K., Miyasaka, T., & Shirai, Y. (2006). Novel Photoelectrochemical Cell with Mesoscopic Electrodes Sensitized by Lead-halide Compounds, 210th ECS Meeting, Abstract#397.
- Kojima, A., Teshima, K., Shirai, Y., & Miyasaka, T. (2009). Organometal halide perovskites as visible-light sensitizers for photovoltaic cells. *Journal of the American Chemical Society*, **131**(17), 6050–6051.
- Kokubu, R., & Yang, Y. (2012). Vertical phase separation of conjugated polymer and fullerene bulk heterojunction films induced by high pressure carbon dioxide treatment at ambient temperature. *Physical Chemistry Chemical Physics*, **14**(23), 8313–8318.
- Konstantakou, M., & Stergiopoulos, T. (2017). A critical review on tin halide perovskite solar cells. *Journal of Materials Chemistry A*, **5**(23), 11518–11549.
- Konstantakou, M., Perganti, D., Falaras, P., & Stergiopoulos, T. (2017). Anti-solvent crystallization strategies for highly efficient perovskite solar cells. *Crystals*, **7**(10), 291.
- Krishnan, U. (2019). Factors affecting the stability of perovskite solar cells: a comprehensive review. *Journal of Photonics for Energy*, **9**(02), 021001.
- Kumar, M. H., Dharani, S., Leong, W. L., Boix, P. P., Prabhakar, R., Baikie, T., Shi, C., Ding, H., Ramesh, R., Asta, M., Graetzel, M., Mhaisalkar, S. G., & Mathews, N. (2014). Lead-Free Halide Perovskite Solar Cells with High Photocurrents Realized Through Vacancy Modulation. *Advanced Materials*, **26**(41), 7122–7127.
- Lanzetta, L., Aristidou, N., & Haque, S. A. (2020). Stability of Lead and Tin Halide Perovskites: The Link between Defects and Degradation. *Journal of Physical Chemistry Letters*, **11**(2), 574–585.
- Lanzetta, L., Webb, T., Zibouche, N., Liang, X., Ding, D., Min, G., Westbrook, R. J. E., Gaggio, B., Macdonald, T. J., Islam, M. S., & Haque, S. A. (2021). Degradation mechanism of hybrid tin-based perovskite solar cells and the critical role of tin (IV) iodide. *Nature Communications*, **12**(1), 2853.
- Le Corre, V. M., Duijnste, E. A., El Tambouli, O., Ball, J. M., Snaith, H. J., Lim, J., & Koster, L. J. A. (2021). Revealing Charge Carrier Mobility and Defect Densities in Metal Halide Perovskites via Space-Charge-Limited Current Measurements. *ACS Energy Letters*, **6**(3), 1087–1094.
- Lee, H. B., Jeon, M. K., Kumar, N., Tyagi, B., & Kang, J. W. (2019). Boosting the Efficiency of SnO₂-Triple Cation Perovskite System Beyond 20% Using Nonhalogenated Antisolvent. *Advanced Functional Materials*, **29**(32), 1903213.

- Lee, M. M., Teuscher, J., Miyasaka, T., Murakami, T. N., Snaith, H. J., & Zeilinger, A. (2012). Efficient Hybrid Solar Cells Based on Meso Superstructured Organometal Halide Perovskites. *Science*, **338**(6107), 643–647.
- Lee, S. J., Shin, S. S., Im, J., Ahn, T. K., Noh, J. H., Jeon, N. J., Seok, S. Il, & Seo, J. (2018). Reducing Carrier Density in Formamidinium Tin Perovskites and Its Beneficial Effects on Stability and Efficiency of Perovskite Solar Cells. *ACS Energy Letters*, **3**(1), 46–53.
- Lee, S. J., Shin, S. S., Kim, Y. C., Kim, D., Ahn, T. K., Noh, J. H., Seo, J., & Seok, S. Il. (2016). Fabrication of Efficient Formamidinium Tin Iodide Perovskite Solar Cells through SnF₂-Pyrazine Complex. *Journal of the American Chemical Society*, **138**(12), 3974–3977.
- Lee, T. D., & Ebong, A. U. (2017). A review of thin film solar cell technologies and challenges. In *Renewable and Sustainable Energy Reviews*, **70**, 1286–1297.
- Lee, T., Song, C. E., Lee, S. K., Shin, W. S., & Lim, E. (2021). Alkyl-Side-Chain Engineering of Nonfused Nonfullerene Acceptors with Simultaneously Improved Material Solubility and Device Performance for Organic Solar Cells. *ACS Omega*, **6**(7), 4562–4573.
- Li, B., Di, H., Chang, B., Yin, R., Fu, L., Zhang, Y. N., & Yin, L. (2021). Efficient Passivation Strategy on Sn Related Defects for High Performance All-Inorganic CsSnI₃ Perovskite Solar Cells. *Advanced Functional Materials*, **31**(11), 2007447.
- Li, B., Li, Z., Gao, D., Wu, X., Li, X., Zhang, C., Li, S., Gong, J., Zhang, D., Xie, X., Xiao, S., Lu, H., Li, M., & Zhu, Z. (2023). Underlayer engineering of grain strain toward efficient and stable tin perovskite solar cells. *Materials Chemistry Frontiers*, **7**, 3406-3413
- Li, D., Wu, P., & Zhang, F. (2023). Alkylammonium chloride promotes the record efficiency of perovskite solar cells. *Joule*, **7**(4), 628–630.
- Li, F., Hou, X., Wang, Z., Cui, X., Xie, G., Yan, F., Zhao, X. Z., & Tai, Q. (2021). FA/MA Cation Exchange for Efficient and Reproducible Tin-Based Perovskite Solar Cells. *ACS Applied Materials and Interfaces*, **13**(34), 40656–40663.
- Li, F., Xie, Y., Hu, Y., Long, M., Zhang, Y., Xu, J., Qin, M., Lu, X., & Liu, M. (2020). Effects of Alkyl Chain Length on Crystal Growth and Oxidation Process of Two-Dimensional Tin Halide Perovskites. *ACS Energy Letters*, **5**, 1422–1429.
- Li, F., Zhang, C., Huang, J., Fan, H., Wang, H., Wang, P., Zhan, C., Liu, C., Li, X., Yang, L., Song, Y., & Jiang, K. (2019). A Cation-Exchange Approach for the Fabrication of Efficient Methylammonium Tin Iodide Perovskite Solar Cells. *Angewandte Chemie*, **131**(20), 6760–6764.
- Li, N., Cheng, C., Wei, H., Liu, H., Li, X., Li, W., & Wang, L. (2017). Enhanced efficiency and stability of inverted perovskite solar cells by interfacial engineering with alkyl bisphosphonic molecules. *RSC Advances*, **7**(67), 42105–42112.
- Li, P., Liu, X., Zhang, Y., Liang, C., Chen, G., Li, F., Su, M., Xing, G., Tao, X., & Song, Y. (2020). Low-Dimensional Dion–Jacobson-Phase Lead-Free Perovskites for High-Performance

- Photovoltaics with Improved Stability. *Angewandte Chemie - International Edition*, **59**(17), 6909–6914.
- Li, S., Yang, F., Chen, M., Yang, J., Jiang, L., Sun, Y., Nirmala Graced, A., Jain, S. M., & Liu, H. (2022). Additive engineering for improving the stability of tin-based perovskite (FASnI₃) solar cells. *Solar Energy*, **243**, 134–141.
- Li, Y., Xie, H., Lim, E. L., Hagfeldt, A., & Bi, D. (2022). Recent Progress of Critical Interface Engineering for Highly Efficient and Stable Perovskite Solar Cells. *Advanced Energy Materials*, **12**(5), 2102730.
- Li, Y., Zhang, Y., Zhu, P., Li, J., Wu, J., Zhang, J., Zhou, X., Jiang, Z., Wang, X., & Xu, B. (2023). Achieving 17.46% Efficiency CsPbI₂Br Perovskite Solar Cells via Multifunction Lead Chloride-Modified ZnO Electron Transporting Layer. *Advanced Functional Materials*, 2309010.
- Liang, L., & Gao, P. (2018). Lead-Free Hybrid Perovskite Absorbers for Viable Application: Can We Eat the Cake and Have It too? *Advanced Science*, **5**(2), 1700331.
- Liao, J. F., Wu, W. Q., Zhong, J. X., Jiang, Y., Wang, L., & Kuang, D. bin. (2019). Enhanced efficacy of defect passivation and charge extraction for efficient perovskite photovoltaics with a small open circuit voltage loss. *Journal of Materials Chemistry A*, **7**(15), 9025–9033.
- Liao, W., Zhao, D., Yu, Y., Grice, C. R., Wang, C., Cimaroli, A. J., Schulz, P., Meng, W., Zhu, K., Xiong, R. G., & Yan, Y. (2016). Lead-Free Inverted Planar Formamidinium Tin Triiodide Perovskite Solar Cells Achieving Power Conversion Efficiencies up to 6.22%. *Advanced Materials*, **28**(42), 9333–9340.
- Liao, Y., Liu, H., Zhou, W., Yang, D., Shang, Y., Shi, Z., Li, B., Jiang, X., Zhang, L., Quan, L. N., Quintero-Bermudez, R., Sutherland, B. R., Mi, Q., Sargent, E. H., & Ning, Z. (2017). Highly Oriented Low-Dimensional Tin Halide Perovskites with Enhanced Stability and Photovoltaic Performance. *Journal of the American Chemical Society*, **139**(19), 6693–6699.
- Lin, L., Jones, T. W., Wang, J. T. W., Cook, A., Pham, N. D., Duffy, N. W., Mihaylov, B., Grigore, M., Anderson, K. F., Duck, B. C., Wang, H., Pu, J., Li, J., Chi, B., & Wilson, G. J. (2020). Strategically Constructed Bilayer Tin (IV) Oxide as Electron Transport Layer Boosts Performance and Reduces Hysteresis in Perovskite Solar Cells. *Small*, **16**(12), 1901466.
- Lin, Z., Liu, C., Liu, G., Yang, J., Duan, X., Tan, L., & Chen, Y. (2020). Preparation of efficient inverted tin-based perovskite solar cells via the bidentate coordination effect of 8-hydroxyquinoline. *Chemical Communications*, **56**(28), 4007–4010.
- Lin, Z., Su, Y., Dai, R., Liu, G., Yang, J., Sheng, W., Zhong, Y., Tan, L., & Chen, Y. (2021). Ionic Liquid-Induced Ostwald Ripening Effect for Efficient and Stable Tin-Based Perovskite Solar Cells. *ACS Applied Materials and Interfaces*, **13**(13), 15420–15428.
- Liu, G., Liu, C., Lin, Z., Yang, J., Huang, Z., Tan, L., & Chen, Y. (2020). Regulated Crystallization of Efficient and Stable Tin-Based Perovskite Solar Cells via a Self-Sealing Polymer. *ACS Applied Materials & Interfaces*, **12**(12), 14049–14056.

- Liu, J., Yao, H., Wang, S., Wu, C., Ding, L., & Hao, F. (2023). Origins and Suppression of Sn(ii)/Sn(iv) Oxidation in Tin Halide Perovskite Solar Cells. *Advanced Energy Materials*, **13**(23), 2300696.
- Liu, W., Li, H., Qiao, B., Zhao, S., Xu, Z., & Song, D. (2022). Highly efficient CIGS solar cells based on a new CIGS bandgap gradient design characterized by numerical simulation. *Solar Energy*, **233**, 337–344.
- Liu, X., Yan, K., Tan, D., Liang, X., Zhang, H., & Huang, W. (2018). Solvent engineering improves efficiency of lead-free tin-based hybrid perovskite solar cells beyond 9%. *ACS Energy Letters*, **3**(11), 2701–2707.
- Liu, Y., Duan, J., Zhang, J., Huang, S., Ou-Yang, W., Bao, Q., Sun, Z., & Chen, X. (2020). High Efficiency and Stability of Inverted Perovskite Solar Cells Using Phenethyl Ammonium Iodide-Modified Interface of NiOx and Perovskite Layers. *ACS Applied Materials and Interfaces*, **12**(1), 771–779.
- Lopes, C. de C. A., Limirio, P. H. J. O., Novais, V. R., & Dechichi, P. (2018). Fourier transform infrared spectroscopy (FTIR) application chemical characterization of enamel, dentin and bone. *Applied Spectroscopy Reviews*, **53**(9), 747–769.
- Ma, Y., Pendlebury, S. R., Reynal, A., Le Formal, F., & Durrant, J. R. (2014). Dynamics of photogenerated holes in undoped BiVO₄ photoanodes for solar water oxidation. *Chemical Science*, **5**(8), 2964–2973.
- Mahalingam, V. (2018). Synthesis, Growth and Characterization of Piperazinium P-Aminobenzoate and Piperazinium P-Chlorobenzoate Nonlinear Optical Single Crystals. *Alagappa University, Karaikudi, India*, 38-41.
- Majhi T., Sridevi M., Jain S., Srivastava A., Kumar M., Srivastava S. & Singh R. (2023). Insight into Controlled Surface Passivation of PEDOT:PSS for Defect Density Modulation and Efficient Charge Transport for Perovskite Solar Cells. *ACS Applied Energy Materials*, **6**(17), 8695-8706
- Milot, R. L., Klug, M. T., Davies, C. L., Wang, Z., Kraus, H., Snaith, H. J., Johnston, M. B., & Herz, L. M. (2018). The Effects of Doping Density and Temperature on the Optoelectronic Properties of Formamidinium Tin Triiodide Thin Films. *Advanced Materials*, **30**(44), 1804506.
- Min, H., Hu, J., Xu, Z., Liu, T., Khan, S., Roh, K., Loo, Y., & Rand, B. P. (2022). Hot-Casting-Assisted Liquid Additive Engineering for Efficient and Stable Perovskite Solar Cells. *Advanced Materials*, **34**(36), 2205309 (9 pages).
- Moghe, D., Wang, L., Traverse, C. J., Redoute, A., Sponseller, M., Brown, P. R., Bulović, V., & Lunt, R. R. (2016). All vapor-deposited lead-free doped CsSnBr₃ planar solar cells. *Nano Energy*, **28**, 469–474.
- Nasti, G., & Abate, A. (2020). Tin Halide Perovskite (ASnX₃) Solar Cells: A Comprehensive Guide toward the Highest Power Conversion Efficiency. *Advanced Energy Materials*, **10**(13), 1902467.

- Nishimura, K., Kamarudin, M. A., Hirotsu, D., Hamada, K., Shen, Q., Iikubo, S., Minemoto, T., Yoshino, K., & Hayase, S. (2020). Lead-free tin-halide perovskite solar cells with 13% efficiency. *Nano Energy*, **74**, 104858.
- Noel, N. K., Stranks, S. D., Abate, A., Wehrenfennig, C., Guarnera, S., Haghighirad, A. A., Sadhanala, A., Eperon, G. E., Pathak, S. K., Johnston, M. B., Petrozza, A., Herz, L. M., & Snaith, H. J. (2014). Lead-free organic-inorganic tin halide perovskites for photovoltaic applications. *Energy and Environmental Science*, **7**(9), 3061–3068.
- Ono, L. K., Raga, S. R., Remeika, M., Winchester, A. J., Gabe, A., & Qi, Y. (2015). Pinhole-free hole transport layers significantly improve the stability of MAPbI₃-based perovskite solar cells under operating conditions. *Journal of Materials Chemistry A*, **3**(30), 15451–15456.
- Park, J., Kim, J., Yun, H.-S., Paik, M. J., Noh, E., Mun, H. J., Kim, M. G., Shin, T. J., & Seok, S. I. (2023). Controlled growth of perovskite layers with volatile alkylammonium chlorides. *Nature*, **616**, 724–730.
- Pascual, J., Flatken, M., Félix, R., Li, G., Turren-Cruz, S. H., Aldamasy, M. H., Hartmann, C., Li, M., di Girolamo, D., Nasti, G., Hüsam, E., Wilks, R. G., Dallmann, A., Bär, M., Hoell, A., & Abate, A. (2021). Fluoride Chemistry in Tin Halide Perovskites. *Angewandte Chemie - International Edition*, **60**(39), 21583–21591.
- Perkowitz, Sidney. (1993). *Optical characterization of semiconductors: infrared, Raman, and photoluminescence spectroscopy*. Department of Theoretical Chemistry, University of Oxford, Oxford, England.
- Quan, L. N., Yuan, M., Comin, R., Voznyy, O., Beauregard, E. M., Hoogland, S., Buin, A., Kirmani, A. R., Zhao, K., Amassian, A., Kim, D. H., & Sargent, E. H. (2016). Ligand-Stabilized Reduced-Dimensionality Perovskites. *Journal of the American Chemical Society*, **138**(8), 2649–2655.
- Rath, T., Handl, J., Weber, S., Friesenbichler, B., Fürk, P., Troi, L., Dimopoulos, T., Kunert, B., Resel, R., & Trimmel, G. (2019). Photovoltaic properties of a triple cation methylammonium/formamidinium/phenylethylammonium tin iodide perovskite. *Journal of Materials Chemistry A*, **7**(16), 9523–9529.
- Ricciarelli, D., Meggiolaro, D., Ambrosio, F., & De Angelis, F. (2020). Instability of tin iodide perovskites: Bulk p-doping versus surface tin oxidation. *ACS Energy Letters*, **5**(9), 2787–2795.
- Ryu, D. H., Khan, N., Park, J., Paik, D., Kang, B. J., Jeon, N. J., Lee, S., Lee, H. K., Lee, S. K., Shin, W. S., Lee, J., Kim, H., Hong, K., Im, S. H., & Song, C. E. (2023). Morphology and Performance Enhancement through the Strong Passivation Effect of Amphoteric Ions in Tin-based Perovskite Solar Cells. *Small*, **2023**, 2302418.
- Saliba, M., Correa-Baena, J. P., Wolff, C. M., Stolterfoht, M., Phung, N., Albrecht, S., Neher, D., & Abate, A. (2018). How to Make over 20% Efficient Perovskite Solar Cells in Regular (n-i-p) and Inverted (p-i-n) Architectures. *Chemistry of Materials*, **30**(13), 4193–4201.

- Sanchez-Diaz, J., Sánchez, R. S., Masi, S., Krečmarová, M., Alvarez, A. O., Barea, E. M., Rodriguez-Romero, J., Chirvony, V. S., Sánchez-Royo, J. F., Martinez-Pastor, J. P., & Mora-Seró, I. (2022). Tin perovskite solar cells with >1,300 h of operational stability in N₂ through a synergistic chemical engineering approach. *Joule*, **6**(4), 861–883.
- Sani, F., Shafie, S., Lim, H. N., & Musa, A. O. (2018). Advancement on lead-free organic-inorganic halide perovskite solar cells: *Materials*, **11**(6), 1008.
- Savill, K. J., Ulatowski, A. M., & Herz, L. M. (2021). Optoelectronic Properties of Tin-Lead Halide Perovskites. *ACS Energy Letters*, **6**(7), 2413–2426.
- Seroka, N. S., Taziwa, R., & Khotseng, L. (2022). Solar Energy Materials-Evolution and Niche Applications. *Materials*, **15**(15), 5338.
- Shao, S., Dong, J., Duim, H., ten Brink, G. H., Blake, G. R., Portale, G., & Loi, M. A. (2019). Enhancing the crystallinity and perfecting the orientation of formamidinium tin iodide for highly efficient Sn-based perovskite solar cells. *Nano Energy*, **60**, 810–816.
- Shao, S., Liu, J., Portale, G., Fang, H. H., Blake, G. R., ten Brink, G. H., Koster, L. J. A., & Loi, M. A. (2018). Highly Reproducible Sn-Based Hybrid Perovskite Solar Cells with 9% Efficiency. *Advanced Energy Materials*, **8**(4), 1702019.
- Shi, Z., & Jayatissa, A. H. (2018). Perovskites-based solar cells: A review of recent progress, materials and processing methods. *Materials*, **11**(5), 729.
- Singh, R., & Parashar, M. (2021). *Origin of Hysteresis in Perovskite Solar Cells*. In Ren, J. and Kan, Z. (eds), soft-matter Thin Film Solar cells: Physical Processes and Device Simulation, Melville, New York: AIP Publishing, 1-1-1-42.
- Sivula, K. (2021). Mott-schottky analysis of photoelectrodes: Sanity checks are needed. *ACS Energy Letters*, **6**(7), 2549–2551.
- Su, Y., Yang, J., Liu, G., Sheng, W., Zhang, J., Zhong, Y., Tan, L., & Chen, Y. (2022). Acetic Acid-Assisted Synergistic Modulation of Crystallization Kinetics and Inhibition of Sn²⁺ Oxidation in Tin-Based Perovskite Solar Cells. *Advanced Functional Materials*, **32**(12), 2109631 (1-9).
- Sun, N., Gao, W., Dong, H., Liu, Y., Liu, X., Wu, Z., Song, L., Ran, C., & Chen, Y. (2021). Architecture of p-i-n Sn-based perovskite solar cells: Characteristics, advances, and perspectives. *ACS Energy Letters* **6**, 2863–2875.
- Suzuki, A., Okada, H., & Oku, T. (2016). Fabrication and characterization of CH₃NH₃PbI_{3-x-y}Br_xCl_y perovskite solar cells. *Energies*, **9**, 376.
- Taylor, N. K., Yukta, Ranjan, R., Ranjan, S., Sharma, T., Singh, A., Garg, A., Nalwa, K. S., Gupta, R. K., & Satapathi, S. (2021). The effect of dimensionality on the charge carrier mobility of halide perovskites. *Journal of Materials Chemistry A*, **9**(38), 21551–21575

- Teymourinia, H., Gonzales, C., Gallardo, J. J., Salavati-Niasari, M., Bisquert, J., Navas, J., & Guerrero, A. (2021). Interfacial Passivation of Perovskite Solar Cells by Reactive Ion Scavengers. *ACS Applied Energy Materials*, **4**(2), 1078–1084.
- Tumen-Ulzii, G., Matsushima, T., & Adachi, C. (2021). Mini-Review on Efficiency and Stability of Perovskite Solar Cells with Spiro-OMeTAD Hole Transport Layer: Recent Progress and Perspectives. *Energy and Fuels*, **35**(23), 18915–18927.
- Undavalli, V. K., Ling, C., & Khandelwal, B. (2021). Impact of alternative fuels and properties on elastomer compatibility. *Aviation Fuels*, **2021**, 113–132.
- Valero, S., Cabrera-Espinoza, A., Collavini, S., Pascual, J., Marinova, N., Kosta, I., & Delgado, J. L. (2020). Naphthalene Diimide-Based Molecules for Efficient and Stable Perovskite Solar Cells. *European Journal of Organic Chemistry*, **2020**(33), 5329–5339.
- Vivo, P., Salunke, J. K., & Priimagi, A. (2017). Hole-transporting materials for printable perovskite solar cells. *Materials*, **10**(9), 1087.
- Wang, C., Gu, F., Zhao, Z., Rao, H., Qiu, Y., Cai, Z., Zhan, G., Li, X., Sun, B., Yu, X., Zhao, B., Liu, Z., Bian, Z., & Huang, C. (2020). Self-Repairing Tin-Based Perovskite Solar Cells with a Breakthrough Efficiency Over 11%. *Advanced Materials*, **32**(31), 1907623.
- Wang, C., Song, Z., Li, C., Zhao, D., & Yan, Y. (2019). Low-Bandgap Mixed Tin-Lead Perovskites and Their Applications in All-Perovskite Tandem Solar Cells. *Advanced Functional Materials*, **29**(47), 1808801.
- Wang, C., Zhang, Y., Gu, F., Zhao, Z., Li, H., Jiang, H., Bian, Z., & Liu, Z. (2021). Illumination Durability and High-Efficiency Sn-Based Perovskite Solar Cell under Coordinated Control of Phenylhydrazine and Halogen Ions. *Matter*, **4**(2), 709–721.
- Wang, F., Jiang, X., Chen, H., Shang, Y., Liu, H., Wei, J., Zhou, W., He, H., Liu, W., & Ning, Z. (2018). 2D-Quasi-2D-3D Hierarchy Structure for Tin Perovskite Solar Cells with Enhanced Efficiency and Stability. *Joule*, **2**(12), 2732–2743.
- Wang, F., Jiang, X., He, H., Wang, F., Jiang, X., Chen, H. H., Shang, Y., Liu, H. H., Wei, J., Trinh, X., Kim, H., Yang, J., Chen, S., Xu, J., Zhang, Q., Liu, H. H., Liu, Z., Zhong, Y., Hufnagel, M., ... Hayase, S. (2020). Lead-free tin-halide perovskite solar cells with 13% efficiency. *Nano Energy*, **74**, 104858.
- Wang, M., Wang, W., Ma, B., Shen, W., Liu, L., Cao, K., Chen, S., & Huang, W. (2021). Lead-Free Perovskite Materials for Solar Cells. *Nano-Micro Letters*, **13**(62).
- Wang, S., Yan, L., Zhu, W., Cao, Z., Zhou, L., Ding, L., & Hao, F. (2022). Suppressing the formation of tin vacancy yields efficient lead-free perovskite solar cells. *Nano Energy*, **99**, 107416.
- Wang, S., Yao, H., Zhu, W., Wu, C., Tang, Z., Liu, J., Ding, L., & Hao, F. (2023). Stabilization of Perovskite Lattice and Suppression of Sn²⁺/Sn⁴⁺ Oxidation via Formamidinium Acetate for High Efficiency Tin Perovskite Solar Cells. *Advanced Functional Materials*, **33**(17), 2215041.

- Wang, T., Loi, H. L., Cao, J., Qin, Z., Guan, Z., Xu, Y., Cheng, H., Li, M. G., Lee, C. S., Lu, X., & Yan, F. (2022). High Open Circuit Voltage Over 1 V Achieved in Tin-Based Perovskite Solar Cells with a 2D/3D Vertical Heterojunction. *Advanced Science*, **9**(18), 2200242.
- Wang, Z., Gan, J., Liu, X., Shi, H., Wei, Q., Zeng, Q., Qiao, L., & Zheng, Y. (2020). Over 1 μm electron-hole diffusion lengths in CsPbI₂Br for high efficient solar cells. *Journal of Power Sources*, **454**, 227913.
- Wang, Z., Lin, Q., Chmiel, F. P., Sakai, N., Herz, L. M., & Snaith, H. J. (2017). Efficient ambient-air-stable solar cells with 2D-3D heterostructured butylammonium-caesium-formamidinium lead halide perovskites. *Nature Energy*, **2**(9), 17135.
- Weber, D. (1978). CH₃NH₃PbX₃, ein Pb(II)-System mit kubischer Perowskitstruktur CH₃NH₃PbX₃, a Pb(II)-System with Cubic Perovskite Structure. *Z. Naturforsch: J. Chem. Sci*, **33**, 1443-1445.
- Weber, D., Heimbürger, R., Schondelmaier, G., Junghans, T., Zetzl, A., Zahn, D. R. T., & Schondelmaier, D. (2023). Cost-effective equipment for surface pre-treatment for cleaning and excitation of substrates in semiconductor technology. *SN Applied Sciences*, **5**(21).
- Wijesekara, A., Walker, M., Han, Y., Walker, D., Huband, S., & Hatton, R. A. (2021). Enhanced Stability of Tin Halide Perovskite Photovoltaics Using a Bathocuproine—Copper Top Electrode. *Advanced Energy Materials*, **11**, 2102766.
- Wu, D., Jia, P., Bi, W., Tang, Y., Zhang, J., Song, B., Qin, L., Lou, Z., Hu, Y., Teng, F., & Hou, Y. (2020). Enhanced performance of tin halide perovskite solar cells by addition of hydrazine monohydrobromide. *Organic Electronics*, **82**, 105728.
- Wu, T., Liu, X., Luo, X., Lin, X., Cui, D., Wang, Y., Segawa, H., Zhang, Y., & Han, L. (2021). Lead-free tin perovskite solar cells. *Joule*, **5**(4), 863–886.
- Xiao, M., Gu, S., Zhu, P., Tang, M., Zhu, W., Lin, R., Chen, C., Xu, W., Yu, T., & Zhu, J. (2018). Tin-Based Perovskite with Improved Coverage and Crystallinity through Tin-Fluoride-Assisted Heterogeneous Nucleation. *Advanced Optical Materials*, **6**(1), 1700615.
- Xiao, Z., Song, Z., & Yan, Y. (2019). From Lead Halide Perovskites to Lead-Free Metal Halide Perovskites and Perovskite Derivatives. *Advanced Materials*, **31**(47), 1803792.
- Xie, W., Peng, L., & Li, N. (2021). An Insight into the Effects of SnF₂ Assisting the Performance of Lead-Free Perovskite of FASnI₃: A First-Principles Calculations. *ACS Omega*, **6**(23), 14938–14951.
- Xing, Y., Deng, Z., Guo, T., Zhang, Z., Tai, Q., Zhao, R., Xiong, J., Wang, Q., Huang, L., Liu, X., Hu, Z., Zhu, Y., & Zhang, J. (2023). Managing iodine and tin based defects for efficient and stable mixed Sn-Pb perovskite solar cells. *Chemical Engineering Journal*, **462**, 142122.
- Xing, Z., Zang, Z., Li, H., Ning, Z., Wong, K. S., & Chow, P. C. Y. (2023). Improved Structural Order and Exciton Delocalization in High-Member Quasi-Two-Dimensional Tin Halide Perovskite Revealed by Electroabsorption Spectroscopy. *The Journal of Physical Chemistry Letters*, **14**(18), 4349–4356.

- Xiong, L., Guo, Y., Wen, J., Liu, H., Yang, G., Qin, P., & Fang, G. (2018). Review on the Application of SnO₂ in Perovskite Solar Cells. *Advanced Functional Materials*, **28**, 1802757.
- Xu, F., Liu, J., Subbiah, A. S., Liu, W., Kang, J., Harrison, G. T., Yang, X., Isikgor, F. H., Aydin, E., De Bastiani, M., & De Wolf, S. (2021). Potassium Thiocyanate-Assisted Enhancement of Slot-Die-Coated Perovskite Films for High-Performance Solar Cells. *Small Science*, **1**(5), 2000044.
- Xu, H., Jiang, Y., He, T., Li, S., Wang, H., Chen, Y., Yuan, M., & Chen, J. (2019). Orientation Regulation of Tin-Based Reduced-Dimensional Perovskites for Highly Efficient and Stable Photovoltaics. *Advanced Functional Materials*, **29**(47), 1807696.
- Xu, L., Feng, X., Jia, W., Lv, W., Mei, A., Zhou, Y., Zhang, Q., Chen, R.-F., & Huang, W. (2021). Recent advances and challenges of inverted lead-free tin-based perovskite solar cells. *Energy & Environmental Science*, **14**, 4292-4317.
- Xu, X., Chueh, C. C., Yang, Z., Rajagopal, A., Xu, J., Jo, S. B., & Jen, A. K. Y. (2017). Ascorbic acid as an effective antioxidant additive to enhance the efficiency and stability of Pb/Sn-based binary perovskite solar cells. *Nano Energy*, **34**, 392–398.
- Xu, Z., Li, N., Niu, X., Liu, H., Liu, G., Chen, Q., & Zhou, H. (2022). Balancing Energy-Level Difference for Efficient n-i-p Perovskite Solar Cells with Cu Electrode. *Energy Material Advances*, **2022**, 9781073.
- Yang, D., Yang, R., Wang, K., Wu, C., Zhu, X., Feng, J., Ren, X., Fang, G., Priya, S., & Liu, S. (Frank). (2018). High efficiency planar-type perovskite solar cells with negligible hysteresis using EDTA-complexed SnO₂. *Nature Communications*, **9**(1), 3239.
- Yang, S. J., Choi, J., Song, S., Park, C., & Cho, K. (2021). Enhancing air-stability and reproducibility of lead-free formamidinium-based tin perovskite solar cell by chlorine doping. *Solar Energy Materials and Solar Cells*, **227**, 111072.
- Yang, W. F., Igbari, F., Lou, Y. H., Wang, Z. K., & Liao, L. S. (2020). Tin Halide Perovskites: Progress and Challenges. *Advanced Energy Materials*, **10**(13), 1902584.
- Yang, W. S., Park, B.-W., Jung, E. H., Jeon, N. J., Kim, Y. C., Lee, D. U., Shin, S. S., Seo, J., Kim, E. K., Noh, J. H., & Seok, S. Il. (2017). Iodide management in formamidinium-lead-halide-based perovskite layers for efficient solar cells. *Science*, **356**, 1376–1379.
- Yang, Z., Yu, Z., Wei, H., Xiao, X., Ni, Z., Chen, B., Deng, Y., Habisreutinger, S. N., Chen, X., Wang, K., Zhao, J., Rudd, P. N., Berry, J. J., Beard, M. C., & Huang, J. (2019). Enhancing electron diffusion length in narrow-bandgap perovskites for efficient monolithic perovskite tandem solar cells. *Nature Communications*, **10**(1), 4498.
- Yao, J., Qiu, B., Zhang, Z. G., Xue, L., Wang, R., Zhang, C., Chen, S., Zhou, Q., Sun, C., Yang, C., Xiao, M., Meng, L., & Li, Y. (2020). Cathode engineering with perylene-diimide interlayer enabling over 17% efficiency single-junction organic solar cells. *Nature Communications*, **11**(1), 2726.

- Yoshikawa, K., Kawasaki, H., Yoshida, W., Irie, T., Konishi, K., Nakano, K., Uto, T., Adachi, D., Kanematsu, M., Uzu, H., & Yamamoto, K. (2017). Silicon heterojunction solar cell with interdigitated back contacts for a photoconversion efficiency over 26%. *Nature Energy*, **2**(5), 17032.
- Yu, B. B., Chen, Z., Zhu, Y., Wang, Y., Han, B., Chen, G., Zhang, X., Du, Z., & He, Z. (2021). Heterogeneous 2D/3D Tin-Halides Perovskite Solar Cells with Certified Conversion Efficiency Breaking 14%. *Advanced Materials*, **33**(36), 2102055.
- Yu, B. B., Liao, M., Zhu, Y., Zhang, X., Du, Z., Jin, Z., Liu, D., Wang, Y., Gatti, T., Ageev, O., & He, Z. (2020). Oriented Crystallization of Mixed-Cation Tin Halides for Highly Efficient and Stable Lead-Free Perovskite Solar Cells. *Advanced Functional Materials*, **30**(24), 2002230.
- Yu, W., Sun, X., Xiao, M., Hou, T., Liu, X., Zheng, B., Yu, H., Zhang, M., Huang, Y., & Hao, X. (2022). Recent advances on interface engineering of perovskite solar cells. *Nano Research*, **15**(1), 85–103.
- Yuan, J., Jiang, Y., He, T., Shi, G., Fan, Z., & Yuan, M. (2019). Two-dimensional perovskite capping layer for stable and efficient tin-lead perovskite solar cells. *Science China Chemistry*, **62**(5), 629–636.
- Yukta, Chavan, R. D., Prochowicz, D., Yadav, P., Tavakoli, M. M., & Satapathi, S. (2022). Thiocyanate-Passivated Diaminonaphthalene-Incorporated Dion–Jacobson Perovskite for Highly Efficient and Stable Solar Cells. *ACS Applied Materials & Interfaces*, **14**(1), 850–860.
- Zhang, L., Ju, M. G., & Liang, W. (2016). The effect of moisture on the structures and properties of lead halide perovskites: A first-principles theoretical investigation. *Physical Chemistry Chemical Physics*, **18**(33), 23174–23183.
- Zhang, R., Li, M., Huan, Y., Xi, J., Zhang, S., Cheng, X., Wu, H., Peng, W., Bai, Z., & Yan, X. (2019). A potassium thiocyanate additive for hysteresis elimination in highly efficient perovskite solar cells. *Inorganic Chemistry Frontiers*, **6**(2), 434–442.
- Zhang, X., Wang, S., Zhu, W., Cao, Z., Wang, A., & Hao, F. (2022). The Voltage Loss in Tin Halide Perovskite Solar Cells: Origins and Perspectives. *Advanced Functional Materials*, **32**(8), 2108832.
- Zhang, Y., Kirs, A., Ambroz, F., Lin, C. T., Bati, A. S. R., Parkin, I. P., Shapter, J. G., Batmunkh, M., & Macdonald, T. J. (2021). Ambient Fabrication of Organic–Inorganic Hybrid Perovskite Solar Cells. *Small Methods*, **5**(1), 2000744.
- Zhang, Z., Kamarudin, M. A., Baranwal, A. K., Wang, L., Kapil, G., Sahamir, S. R., Sanehira, Y., Chen, M., Shen, Q., & Hayase, S. (2022). Indent-Free Vapor-Assisted Surface Passivation Strategy toward Tin Halide Perovskite Solar Cells. *ACS Applied Materials and Interfaces*, **14**(31), 36200–36208.
- Zhao, Z., Gu, F., Li, Y., Sun, W., Ye, S., Rao, H., Liu, Z., Bian, Z., & Huang, C. (2017). Mixed-Organic-Cation Tin Iodide for Lead-Free Perovskite Solar Cells with an Efficiency of 8.12%. *Advanced Science*, **4**, 1700204 9.

- Zhao, Z., Gu, F., Wang, C., Zhan, G., Zheng, N., Bian, Z., & Liu, Z. (2020). Orientation Regulation of Photoactive Layer in Tin-Based Perovskite Solar Cells with Allylammonium Cations. *Solar RRL*, **4**(10), 2000315.
- Zheng, C., Qiu, P., Zhong, S., Luo, X., Wu, S., Wang, Q., Gao, J., Lu, X., Gao, X., Shui, L., Wu, S., & Liu, J. M. (2023). Dual Effects of Slow Recrystallization and Defects Passivation Achieve Efficient Tin-Based Perovskite Solar Cells with Good Stability Up to One Year. *Advanced Functional Materials*, **33**(12), 2212106.
- Zhou, R., Liu, X., Li, H., Peng, X., Gong, X., Ouyang, Y., Luo, H., Fu, Y., & Peng, Y. (2022). Multifunctional Passivation Strategy of Cationic and Anionic Defects for Efficient and Stable Perovskite Solar Cells. *ACS Applied Energy Materials*, **5**(5), 5928–5936.
- Zhu, H., Liu, Y., Eickemeyer, F. T., Pan, L., Ren, D., Ruiz, M., Hagfeldt, A., Dar, M. I., Li, X., & Grätzel, M. (n.d.). Tailored Amphiphilic Molecular Passivator for Stable Perovskite Solar Cells with 23.5% efficiency. *Advanced Materials*, **32**(12), 1907757.
- Zhu, Z., & Mi, Q. (2022). Substituted thiourea as versatile ligands for crystallization control and surface passivation of tin-based perovskite. *Cell Reports Physical Science*, **3**(1), 100690.
- Zhu, Z., Chueh, C. C., Li, N., Mao, C., & Jen, A. K. Y. (2018). Realizing Efficient Lead-Free Formamidinium Tin Triiodide Perovskite Solar Cells via a Sequential Deposition Route. *Advanced Materials*, **30**(6), 1703800.
- Zhu, Z., Jiang, X., Yu, D., Yu, N., Ning, Z., & Mi, Q. (2022). Smooth and Compact FASnI₃ Films for Lead-Free Perovskite Solar Cells with over 14% Efficiency. *ACS Energy Letters*, **7**(6), 2079–2083.
- Best-research-cell-efficiencies Chart. *NREL* (2022). <https://www.nrel.gov/pv/cell-efficiency.html> (Accessed May 2022).
- Bondarenko, A. S., & Ragoisha, G. A. (2005). in Progress in Chemometrics Research. In *Pomerantsev A. L., Ed., Nova Science Publishers: New York*. <http://www.abc.chemistry.bsu.by/vi/analyser/> (Accessed February 2023).
- Bp Statistical Review of World Energy. (2022). *Statistical Review of World Energy 2022*. <https://www.bp.com/content/dam/bp/business-sites/en/global/corporate/pdfs/energy-economics/statistical-review/bp-stats-review-2022-full-report.pdf> (accessed June 2022)
- Deutsche Bank. (2014). *Deutsche Bank Markets Research*. https://investor-relations.db.com/files/documents/annual-reports/Annual_Financial_Statements_and_Management_Report_Deutsche_Bank_AG_2014.pdf?language_id=1 (accessed February 2022).
- Imamzai, M., Aghaei, M., Hanum, Y., Thayoob, M., & Forouzanfar, M. (2012). *A Review on Comparison between Traditional Silicon Solar Cells and Thin-Film CdTe Solar Cells*. <https://www.researchgate.net/publication/253327599> (accessed March 2023)

- National Renewable Energy Laboratory. (2020). *NREL_efficiencies_chart.pdf*.
<https://www.nrel.gov/pv/cell-efficiency.html>
- National Renewable Energy Laboratory. Best Research-Cell Efficiency Chart | Photovoltaic Research | NREL. <https://www.nrel.gov/pv/cell-efficiency.html> (Accessed November 2022)
- NREL Best Research-Cell Efficiency Chart*. (2022). <https://www.nrel.gov/pv/cell-efficiency.html>
- Wang, S. (2014). *How to UV Ozone Cleaning*.
https://chem.uiowa.edu/sites/chem.uiowa.edu/files/people/shaw/Scarlett-How%20to%20UV-OZONE%20Sep_15th.pdf (accessed November 2023)
- World Energy Outlook 2022*. (2022). www.iea.org/t&c/ (accessed December 2022)
- Xiang, J. (2018). *Foutier Transform Infrared Spectroscopy Instrumentation and Integration with Thermogravimetry*. Masters Theses & Specialist Projects. Paper2572
<https://digitalcommons.wku.edu/theses/2572/> (accessed March 2023).